

1

²A SEARCH FOR LONG-LIVED, CHARGED, SUPERSYMMETRIC PARTICLES
³USING IONIZATION WITH THE ATLAS DETECTOR

4

BRADLEY AXEN

5

September 2016 – Version 0.47

6



⁸ Bradley Axen: *A Search for Long-Lived, Charged, Supersymmetric Particles using
9 Ionization with the ATLAS Detector*, Subtitle, © September 2016

10

Usually a quotation.

11

Dedicated to.

₁₂ ABSTRACT

₁₃ How to write a good abstract:

₁₄ <https://plg.uwaterloo.ca/~migod/research/beck00PSLA.html>

₁₅ PUBLICATIONS

₁₆ Some ideas and figures have appeared previously in the following publications:

₁₇

₁₈ Put your publications from the thesis here. The packages `multibib` or `bibtopic`
₁₉ etc. can be used to handle multiple different bibliographies in your document.

²¹ ACKNOWLEDGEMENTS

²² Put your acknowledgements here.

²³

²⁴ And potentially a second round.

²⁵

26 CONTENTS

27	I	INTRODUCTION	1
28	1	INTRODUCTION	3
29	II	THEORETICAL CONTEXT	5
30	2	STANDARD MODEL	7
31	2.1	Particles	7
32	2.2	Interactions	8
33	2.3	Limitations	8
34	3	SUPERSYMMETRY	9
35	3.1	Motivation	9
36	3.2	Structure	9
37	3.3	Phenomenology	9
38	4	LONG-LIVED PARTICLES	11
39	4.1	Mechanisms	11
40	4.1.1	Examples in Supersymmetry	11
41	4.2	Phenomenology	11
42	4.2.1	Disimilarities to Prompt Decays	11
43	4.2.2	Characteristic Signatures	11
44	III	EXPERIMENTAL STRUCTURE AND RECONSTRUCTION	13
45	5	THE LARGE HADRON COLLIDER	15
46	5.1	Injection Chain	16
47	5.2	Design	17
48	5.2.1	Layout	17
49	5.2.2	Magnets	18
50	5.2.3	RF Cavities	19
51	5.2.4	Beam	21
52	5.3	Luminosity Parameters	21
53	5.4	Delivered Luminosity	23
54	6	THE ATLAS DETECTOR	25
55	6.1	Coordinate System	27
56	6.2	Magnetic Field	28
57	6.3	Inner Detector	30
58	6.3.1	Pixel Detector	33
59	6.3.2	Semiconductor Tracker	35
60	6.3.3	Transition Radiation Tracker	37
61	6.4	Calorimetry	38
62	6.4.1	Electromagnetic Calorimeter	40
63	6.4.2	Hadronic Calorimeters	41
64	6.5	Muon Spectrometer	43
65	6.5.1	Monitored Drift Tube	45

66	6.5.2	Resistive Plate Chamber	46
67	6.5.3	Cathode Strip Chamber	46
68	6.5.4	Thin Gap Chamber	46
69	6.6	Trigger	48
70	7	EVENT RECONSTRUCTION	51
71	7.1	Tracks and Vertices	51
72	7.1.1	Pixel Neural Network	53
73	7.1.2	Pixel dE/dx	54
74	7.1.3	Vertex Reconstruction	54
75	7.2	Electrons and Photons	55
76	7.2.1	Photon Identification	56
77	7.2.2	Electron Identification	56
78	7.3	Muons	56
79	7.3.1	Muon Identification	57
80	7.4	Jets	57
81	7.4.1	Topological Clustering	58
82	7.4.2	Jet Algorithms	59
83	7.4.3	Jet Energy Scale	60
84	7.5	Missing Transverse Energy	60
85	IV	CALORIMETER RESPONSE	63
86	8	RESPONSE MEASUREMENT WITH SINGLE HADRONS	65
87	8.1	Dataset and Simulation	66
88	8.1.1	Data Samples	66
89	8.1.2	Simulated Samples	66
90	8.1.3	Event Selection	66
91	8.2	Inclusive Hadron Response	67
92	8.2.1	E/p Distribution	67
93	8.2.2	Zero Fraction	68
94	8.2.3	Neutral Background Subtraction	69
95	8.2.4	Corrected Response	71
96	8.2.5	Additional Studies	73
97	8.3	Identified Particle Response	76
98	8.3.1	Decay Reconstruction	76
99	8.3.2	Identified Response	77
100	8.3.3	Additional Species in Simulation	79
101	8.4	Summary	80
102	9	JET ENERGY RESPONSE AND UNCERTAINTY	83
103	9.1	Motivation	83
104	9.2	Uncertainty Estimate	83
105	9.3	Summary	86
106	V	SEARCH FOR LONG-LIVED PARTICLES	89
107	10	LONG-LIVED PARTICLES IN ATLAS	91
108	10.1	Event Topology	91
109	10.1.1	Detector Interactions	92
110	10.1.2	Lifetime Dependence	93

111	10.2 Simulation	96
112	11 EVENT SELECTION	99
113	11.1 Trigger	100
114	11.2 Kinematics and Isolation	101
115	11.3 Particle Species Rejection	105
116	11.4 Ionization	108
117	11.4.1 Mass Estimation	109
118	11.5 Efficiency	110
119	12 BACKGROUND ESTIMATION	113
120	12.1 Background Sources	113
121	12.2 Prediction Method	114
122	12.3 Validation	115
123	12.3.1 Closure in Simulation	115
124	12.3.2 Validation Region in Data	116
125	13 SYSTEMATIC UNCERTAINTIES AND RESULTS	119
126	13.1 Systematic Uncertainties	119
127	13.1.1 Background Estimate	119
128	13.1.2 Signal Yield	120
129	13.2 Final Yields	126
130	13.3 Cross Sectional Limits	127
131	13.4 Mass Limits	129
132	13.5 Context for Long-Lived Searches	131
133	VI CONCLUSIONS	135
134	14 SUMMARY AND OUTLOOK	137
135	14.1 Summary	137
136	14.2 Outlook	137
137	VII APPENDIX	139
138	A INELASTIC CROSS SECTION	141
139	B EXPANDED R-HADRON YIELDS AND LIMITS	143
140	BIBLIOGRAPHY	149

141 LIST OF FIGURES

142	Figure 1	The particle content of the Standard Model (SM).	8
143	Figure 2	The four collision points and corresponding experiments of the Large Hadron Collider (LHC). The image includes the location of the nearby city of Geneva as well as the border of France and Switzerland.	16
144			
145			
146			
147	Figure 3	The cumulative luminosity over time delivered to the A Toroidal LHC ApparatuS (ATLAS) experiment from high energy proton-proton collisions since 2011. The energies of the collisions are listed for each of the data-taking periods.	17
148			
149			
150			
151			
152	Figure 4	The accelerator complex that builds up to the full design energies at the LHC . The protons are passed in order to Linac 2, the PSB , the PS , the SPS and then the LHC	18
153			
154			
155			
156	Figure 5	A schematic of the layout of the LHC , not to scale. The arched and straight sections are illustrated at the bottom of the schematic, and all four crossing sites are indicated with their respective experiments.	19
157			
158			
159			
160	Figure 6	A cross section of the the cryodipole magnets which bend the flight path of protons around the circumference of the LHC . The diagram includes both the superconducting coils which produce the magnetic field and the structural elements which keep the magnets precisely aligned.	20
161			
162			
163			
164			
165			
166	Figure 7	The arrangement of four radiofrequency (RF) cavities within a cryomodule.	20
167			
168	Figure 8	The cumulative luminosity versus time delivered to ATLAS (green), recorded by ATLAS (yellow), and certified to be good quality data (blue) during stable beams for pp collisions at 13 TeV in 2015.	23
169			
170			
171			
172	Figure 9	The luminosity-weighted distribution of the mean number of interactions per crossing for the 2015 pp collision data at 13 TeV.	24
173			
174			
175	Figure 10	A cut-away schematic of the layout of the ATLAS detector. Each of the major subsystems is indicated.	26
176			
177	Figure 11	A cross-sectional slice of the ATLAS experiment which illustrates how the various SM particles interact with the detector systems.	26
178			
179			
180	Figure 12	The layout of the four superconducting magnets in the ATLAS detector.	29
181			

182	Figure 13	The arrangement of the subdetectors of the ATLAS inner detector. Each of the subdetectors is labeled in the cut-away view of the system.	31
183			
184			
185	Figure 14	A quarter section of the ATLAS inner detector which shows the layout of each of the subdetectors in detail. The lower panel shows an enlarged view of the pixel detector. Example trajectories for a particle with $\eta = 1.0, 1.5, 2.0, 2.5$ are shown. The Insertible B-Layer (IBL), which was added after the original detector commissioning, is not shown.	31
186			
187			
188			
189			
190			
191			
192	Figure 15	A computer generated three-dimensional view of the inner detector along the line of the beam axis. The subdetectors and their positions are labeled.	32
193			
194			
195	Figure 16	An alternative computer generated three-dimensional view of the inner detector transverse to the beam axis. The subdetectors and their positions are labeled.	32
196			
197			
198	Figure 17	The integrated radiation lengths traversed by a straight track at the exit of the ID envelope, including the services and thermal enclosures. The distribution is shown as a function of $ \eta $ and averaged over ϕ . The breakdown indicates the contributions of individual subdetectors, including services in their active volume.	33
199			
200			
201			
202			
203			
204	Figure 18	36
205	Figure 19	An image of the insertion of the IBL into the current pixel detector.	36
206			
207	Figure 20	A three-dimensional computer-generated image of the geometry of the IBL with a view (a) mostly transverse to the beam pipe (b) mostly parallel to the beam pipe.	37
208			
209			
210	Figure 21	An exploded view of the geometry of the silicon microstrip (SCT) double layers in the barrel region.	38
211			
212	Figure 22	39
213	Figure 23	The depth of (a) the electromagnetic barrel calorimeter in radiation lengths and (b) all calorimeters in interaction lengths as a function of pseudorapidity.	40
214			
215			
216	Figure 24	A schematic of the Liquid Argon (LAr) calorimeter in the barrel region, highlighting the accordion structure.	40
217			
218	Figure 25	A schematic of a hadronic tile module which shows the alternating layers of steel and plastic scintillator.	42
219			
220	Figure 26	The segmentation in depth and η of the tile-calorimeter modules in the central (left) and extended (right) barrels.	42
221			
222	Figure 27	A cut-away diagram of the muon systems on ATLAS	43
223	Figure 28	A quarter view of the muon spectrometer which highlights the layout of each of the detecting elements. The BOL, BML, BIL, EOL, EML, and EIL are all Monitored Drift Tube (MDT) elements, where the acronyms encode their positions.	44
224			
225			
226			
227			

228	Figure 29	A schematic of the cross-section of the muon spectrometer in the barrel region.	44
229			
230	Figure 30	A schematic of a single MDT chamber, which shows the multilayers of drift tubes as well as the alignment system.	45
231			
232			
233	Figure 31	A schematic of the Cathode Strip Chamber (CSC) endcap, showing the overlapping arrangement of the eight large and eight small chambers.	47
234			
235			
236	Figure 32	A schematic of the Thin Gap Chamber (TGC) doublet and triplet layers.	47
237			
238	Figure 33	The L1 Trigger rate broken down into the types of triggers as a function of the luminosity block for the 2015 data collection period.	49
239			
240			
241	Figure 34	The HLT Trigger rate broken down into the types of triggers as a function of the luminosity block for the 2015 data collection period.	50
242			
243			
244	Figure 35	The x and y locations of the hits generated in a simulated $t\bar{t}$ event in the inner detector. The hits which belong to tracks formed using the inside-out algorithm are highlighted in red, while the hits which belong to tracks formed using the outside-in algorithm are circled in black.	52
245			
246			
247			
248			
249			
250	Figure 36	Examples of the clusters formed in a single layer of the pixel detector for (a) a single isolated particle, (b) two nearly-overlapping particles, and (c) a particle which emits a δ -ray [12].	53
251			
252			
253			
254	Figure 37	The total, fractional jet energy scale (JES) uncertainties estimated for 2015 data as a function of jet p_T	61
255			
256	Figure 38	An illustration (a) of the E/p variable used throughout this paper. The red energy deposits come from the charged particle targeted for measurement, while the blue energy deposits are from nearby neutral particles and must be subtracted. The same diagram (b) for the neutral-background selection, described in Section 8.2.3.	68
257			
258			
259			
260			
261			
262	Figure 39	The E/p distribution and ratio of simulation to data for isolated tracks with (a) $ \eta < 0.6$ and $1.2 < p/\text{GeV} < 1.8$ and (b) $ \eta < 0.6$ and $2.2 < p/\text{GeV} < 2.8$	68
263			
264			
265	Figure 40	The fraction of tracks as a function (a, b) of momentum, (c, d) of interaction lengths with $E \leq 0$ for tracks with positive (on the left) and negative (on the right) charge.	70
266			
267			
268			
269	Figure 41	$\langle E/p \rangle_{\text{BG}}$ as a function of the track momentum for tracks with (a) $ \eta < 0.6$, (b) $0.6 < \eta < 1.1$, and as a function of the track pseudorapidity for tracks with (c) $1.2 < p/\text{GeV} < 1.8$, (d) $1.8 < p/\text{GeV} < 2.2$	71
270			
271			
272			

273	Figure 42	$\langle E/p \rangle_{\text{COR}}$ as a function of track momentum, for tracks with (a) $ \eta < 0.6$, (b) $0.6 < \eta < 1.1$, (c) $1.8 < \eta < 1.9$, and (d) $1.9 < \eta < 2.3$	72
274			
275			
276	Figure 43	$\langle E/p \rangle_{\text{COR}}$ calculated using LCW-calibrated topological clusters as a function of track momentum for tracks with (a) zero or more associated topological clusters or (b) one or more associated topological clusters.	73
277			
278			
279			
280	Figure 44	Comparison of the $\langle E/p \rangle_{\text{COR}}$ for tracks with (a) less than and (b) greater than 20 hits in the TRT.	74
281			
282	Figure 45	Comparison of the $\langle E/p \rangle_{\text{COR}}$ for (a) positive and (b) negative tracks as a function of track momentum for tracks with $ \eta < 0.6$	74
283			
284			
285	Figure 46	Comparison of the E/p distributions for (a) positive and (b) negative tracks with $0.8 < p/\text{GeV} < 1.2$ and $ \eta < 0.6$, in simulation with the FTFP_BERT and QGSP_BERT physics lists.	75
286			
287			
288			
289	Figure 47	Comparison of the response of the hadronic calorimeter as a function of track momentum (a) at the EM-scale and (b) after the LCW calibration.	75
290			
291			
292	Figure 48	Comparison of the response of the EM calorimeter as a function of track momentum (a) at the EM-scale and (b) with the LCW calibration.	76
293			
294			
295	Figure 49	The reconstructed mass peaks of (a) K_S^0 , (b) Λ , and (c) $\bar{\Lambda}$ candidates.	77
296			
297	Figure 50	The E/p distribution for isolated (a) π^+ , (b) π^- , (c) proton, and (d) anti-proton tracks.	78
298			
299	Figure 51	The fraction of tracks with $E \leq 0$ for identified (a) π^+ and π^- , and (b) proton and anti-proton tracks	78
300			
301	Figure 52	The difference in $\langle E/p \rangle$ between (a) π^+ and π^- (b) p and π^+ , and (c) \bar{p} and π^-	79
302			
303	Figure 53	$\langle E/p \rangle_{\text{COR}}$ as a function of track momentum for (a) π^+ tracks and (b) π^- tracks.	80
304			
305	Figure 54	The ratio of the calorimeter response to single particles of various species to the calorimeter response to π^+ with the physics list FTFP_BERT.	80
306			
307			
308	Figure 55	The spectra of true particles inside anti- k_t , $R = 0.4$ jets with (a) $90 < p_T/\text{GeV} < 100$, (b) $400 < p_T/\text{GeV} < 500$, and (c) $1800 < p_T/\text{GeV} < 2300$	84
309			
310			
311	Figure 56	The JES uncertainty contributions, as well as the total JES uncertainty, as a function of jet p_T for (a) $ \eta < 0.6$ and (b) $0.6 < \eta < 1.1$	86
312			
313			
314	Figure 57	The JES correlations as a function of jet p_T and $ \eta $ for jets in the central region of the detector.	87
315			

316	Figure 58	A schematic diagram of an R-Hadron event with a life-time around 0.01 ns. The diagram includes one charged R-Hadron (solid blue), one neutral R-Hadron (dashed blue), Lightest Supersymmetric Particles (LSPs) (dashed green) and charged hadrons (solid orange). The pixel detector, calorimeters, and muon system are illustrated but not to scale.	93
317			
318			
319			
320			
321			
322			
323	Figure 59	A schematic diagram of an R-Hadron event with a life-time around 4 ns. The diagram includes one charged R-Hadron (solid blue), one neutral R-Hadron (dashed blue), LSPs (dashed green) and a charged hadron (solid orange). The pixel detector, calorimeters, and muon system are illustrated but not to scale.	94
324			
325			
326			
327			
328			
329	Figure 60	A schematic diagram of an R-Hadron event with a life-time around 5 ns. The diagram includes one charged R-Hadron (solid blue), one neutral R-Hadron (dashed blue), LSPs (dashed green) and charged hadrons (solid orange). The pixel detector, calorimeters, and muon system are illustrated but not to scale.	95
330			
331			
332			
333			
334			
335	Figure 61	A schematic diagram of an R-Hadron event with a life-time around 20 ns. The diagram includes one charged R-Hadron (solid blue), one neutral R-Hadron (dashed blue), LSPs (dashed green) and charged hadrons (solid orange). The pixel detector, calorimeters, and muon system are illustrated but not to scale.	95
336			
337			
338			
339			
340			
341	Figure 62	A schematic diagram of an R-Hadron event with a life-time around 20 ns. The diagram includes one charged R-Hadron (solid blue) and one neutral R-Hadron (dashed blue). The pixel detector, calorimeters, and muon system are illustrated but not to scale.	96
342			
343			
344			
345			
346	Figure 63	The distribution of (a) E_T^{miss} and (b) Calorimeter E_T^{miss} for simulated signal events before the trigger requirement.	100
347			
348			
349	Figure 64	The distribution of E_T^{miss} for data and simulated signal events, after the trigger requirement.	102
350			
351	Figure 65	The trigger efficiency for the HLT_xe70 trigger requirement as a function of (a) E_T^{miss} and (b) Calorimeter E_T^{miss} for simulated signal events.	103
352			
353			
354	Figure 66	The dependence of dE/dx on N_{split} in data after basic track hit requirements have been applied.	104
355			
356	Figure 67	The distribution of dE/dx with various selections applied in data and simulated signal events.	104
357			
358	Figure 68	The distribution of track momentum for data and simulated signal events, after previous selection requirements have been applied.	105
359			
360			

361	Figure 69	The distribution of M_T for data and simulated signal events, after previous selection requirements have been applied.	106
362			
363			
364	Figure 70	The distribution of summed tracked momentum within a cone of $\Delta R < 0.25$ around the candidate track for data and simulated signal events, after previous selection requirements have been applied.	107
365			
366			
367			
368	Figure 71	The normalized, two-dimensional distribution of E/p and f_{EM} for simulated (a) $Z \rightarrow ee$, (b) $Z \rightarrow \tau\tau$, (c) 1200 GeV Stable R-Hadron events, and (d) 1200 GeV, 10 ns R-Hadron events.	108
369			
370			
371			
372	Figure 72	Two-dimensional distribution of dE/dx versus charge signed momentum (qp) for minimum-bias tracks. The fitted distributions of the most probable values for pions, kaons and protons are superimposed.	109
373			
374			
375			
376	Figure 73	The distribution of mass estimated using dE/dx for simulated stable R-Hadrons with masses between 1000 and 1600 GeV.	110
377			
378			
379	Figure 74	The acceptance \times efficiency as a function of R-Hadron (a) mass and (b) lifetime. (a) shows all of the combinations of mass and lifetime considered in this search, and (b) highlights the lifetime dependence for 1000 GeV and 1600 GeV R-Hadrons.	112
380			
381			
382			
383			
384	Figure 75	The distribution of (a) dE/dx and (b) momentum for tracks in data and simulated signal after requiring the event level selection and the track selection on p_T , hits, and N_{split} . Each sub-figure shows the normalized distributions for tracks classified as hadrons, electrons, and muons in data and R-Hadrons in the simulated signal.	114
385			
386			
387			
388			
389			
390			
391	Figure 76	The distribution of $M_{dE/dx}$ (a) before and (b) after the ionization requirement for tracks in simulated W boson decays and for the randomly generated background estimate.	116
392			
393			
394			
395	Figure 77	The distribution of $M_{dE/dx}$ (a) before and (b) after the ionization requirement for tracks in the validation region and for the randomly generated background estimate.	117
396			
397			
398			
399	Figure 78	The trigger efficiency for the HLT_xe70 trigger requirement as a function of Calorimeter E_T^{miss} for simulated data events with a W boson selection. Simulated signal events and simulated W boson events are also included.	122
400			
401			
402			
403			
404	Figure 79	The efficiency of the muon veto for R-hadrons of two different masses, as a function of $\frac{1}{\beta}$ for simulated R-Hadron tracks.	124
405			
406			

407	Figure 80	The average reconstructed MDT β distribution for $Z \rightarrow \mu\mu$ events in which one of the muons is reconstructed as a slow muon, for both data and simulation. A gaussian fit is superimposed.	125
408			
409			
410			
411	Figure 81	The observed mass distribution of events in data and the generated background distribution in (a) the stable and (b) the metastable signal region. A few example simulated signal distributions are superimposed.	126
412			
413			
414			
415	Figure 82	The observed and expected cross section limits as a function of mass for the stable simulated signal. The predicted cross section values for the corresponding signals are included.	129
416			
417			
418			
419	Figure 83	The observed and expected cross section limits as a function of mass for each generated lifetime. The predicted cross section values for the corresponding signals are included.	130
420			
421			
422			
423	Figure 84	The excluded range of masses as a function of gluino lifetime. The expected lower limit (LL), with its experimental $\pm 1\sigma$ band, is given with respect to the nominal theoretical cross-section. The observed 95% LL obtained at $\sqrt{s} = 8$ TeV [68] is also shown for comparison.	132
424			
425			
426			
427			
428	Figure 85	The constraints on the gluino mass as a function of lifetime for a split-supersymmetry model with the gluino R-Hadrons decaying into a gluon or light quarks and a neutralino with mass of 100 GeV. The solid lines indicate the observed limits, while the dashed lines indicate the expected limits. The area below the curves is excluded. The dots represent results for which the particle is assumed to be prompt or stable.	133
429			
430			
431			
432			
433			
434			
435			

436 LIST OF TABLES

437 Table 1	The design parameters of the LHC beam that determines the energy of collisions and the luminosity, for both the injection of protons and at the nominal circulation.	22
438		
439		
440		
441 Table 2	The performance goals for each of the subsystems of the ATLAS detector. The $ \eta $ coverage specifies the range where the subsystem needs to be able to provide measurements with the specified resolution. The resolutions include a p_T or E dependence that is added in quadrature with a p_T/E independent piece.	27
442		
443		
444		
445		
446		
447 Table 3	A summary of the parameters of each of the three magnet systems on ATLAS.	29
448		
449 Table 4	A summary of the parameters of the inner detector and each of the subdetectors [3].	34
450		
451 Table 5	A summary of the expected performance of the combined inner detector [8]. Included are the reconstruction efficiencies for multiple particle types as well as the momentum and impact parameter (IP) resolution for various momenta.	35
452		
453		
454		
455		
456 Table 6	The trigger menu for the 2015 data collection with $L = 5 \times 10^{33} \text{ cm}^{-2} \text{ s}^{-1}$. Both the L1 and high level trigger (HLT) selection requirements and their trigger rates are shown measured at the specified luminosity are shown. The typical offline selections represent a typical set of offline requirements imposed after the trigger in an analysis.	49
457		
458		
459		
460		
461		
462		
463 Table 7	The dominant sources of corrections and systematic uncertainties in the JES estimation technique, including typical values for the correcting shift (Δ) and the associated uncertainty (σ).	85
464		
465		
466		
467 Table 8	The expected number of events at each level of the selection for metastable 1600 GeV, 10 ns R-Hadrons, along with the number of events observed in data, for 3.2 fb^{-1} . The simulated yields are shown with statistical uncertainties only. The total efficiency \times acceptance is also shown for the signal.	111
468		
469		
470		
471		
472		
473 Table 9	A summary of the sources of systematic uncertainty for the data-driven background in the signal region. If the uncertainty depends on the mass, the maximum values are reported.	119
474		
475		
476		

477	Table 10	A summary of the sources of systematic uncertainty for the simulated signal yield. The uncertainty depends on the mass and lifetime, and the maximum negative and positive values are reported in the table.	121
478			
479			
480			
481	Table 11	Example of the contributing systematic variations to the total systematic for the E_T^{miss} Scale, as measured in a 1200 GeV, Stable R-Hadron signal sample.	123
482			
483			
484	Table 12	The estimated number of background events and the number of observed events in data for the specified selection regions prior to the requirement on mass. The background estimates show statistical and systematic uncertainties.	126
485			
486			
487			
488			
489	Table 13	The left and right extremum of the mass window for each generated mass point with a 10 ns lifetime.	127
490			
491	Table 14	The left and right extremum of the mass window used for each generated stable mass point.	127
492			
493	Table 15	The expected number of signal events, the expected number of background events, and the observed number of events in data with their respective statistical errors within the respective mass window for each generated stable mass point.	128
494			
495			
496			
497			
498	Table 16	The expected number of signal events, the expected number of background events, and the observed number of events in data with their respective statistical errors within the respective mass window for each generated mass point with a lifetime of 10 ns.	128
499			
500			
501			
502			
503	Table 17	The observed and expected 95% CL lower limit on mass for gluino R-Hadrons for each considered lifetime.	131
504			
505	Table 18	The left and right extremum of the mass window for each generated mass point with a 50 ns lifetime.	143
506			
507	Table 19	The left and right extremum of the mass window for each generated mass point with a 30 ns lifetime.	143
508			
509	Table 20	The left and right extremum of the mass window for each generated mass point with a 10 ns lifetime.	144
510			
511	Table 21	The left and right extremum of the mass window used for each generated mass point with a lifetime of 3 ns.	144
512			
513	Table 22	The left and right extremum of the mass window used for each mass point with a lifetime of 1 ns.	144
514			
515	Table 23	The left and right extremum of the mass window for each generated mass point with a lifetime of 0.4 ns.	145
516			
517	Table 24	The left and right extremum of the mass window used for each generated stable mass point.	145
518			

519	Table 25	The expected number of signal events, the expected number of background events, and the observed number of events in data with their respective statistical errors within the respective mass window for each generated mass point with a lifetime of 50 ns.	145
520			
521			
522			
523			
524	Table 26	The expected number of signal events, the expected number of background events, and the observed number of events in data with their respective statistical errors within the respective mass window for each generated mass point with a lifetime of 30 ns.	146
525			
526			
527			
528			
529	Table 27	The expected number of signal events, the expected number of background events, and the observed number of events in data with their respective statistical errors within the respective mass window for each generated mass point with a lifetime of 10 ns.	146
530			
531			
532			
533			
534	Table 28	The expected number of signal events, the expected number of background events, and the observed number of events in data with their respective statistical errors within the respective mass window for each generated mass point with a lifetime of 3 ns.	147
535			
536			
537			
538			
539	Table 29	The expected number of signal events, the expected number of background events, and the observed number of events in data with their respective statistical errors within the respective mass window for each generated mass point with a lifetime of 1 ns.	147
540			
541			
542			
543			
544	Table 30	The expected number of signal events, the expected number of background events, and the observed number of events in data with their respective statistical errors within the respective mass window for each generated mass point with a lifetime of p4 ns.	148
545			
546			
547			
548			
549	Table 31	The expected number of signal events, the expected number of background events, and the observed number of events in data with their respective statistical errors within the respective mass window for each generated stable mass point	148
550			
551			
552			
553			

554 LISTINGS

555 ACRONYMS

- 556 SM Standard Model
557 CERN European Organization for Nuclear Research
558 SUSY Supersymmetry
559 LSP Lightest Supersymmetric Particle
560 LHC Large Hadron Collider
561 ATLAS A Toroidal LHC ApparatuS
562 CMS Compact Muon Solenoid
563 ALICE A Large Ion Collider Experiment
564 LHCb Large Hadron Collider beauty experiment
565 LEP the Large Electron Positron collider
566 PS Proton Synchrotron
567 PSB Proton Synchrotron Booster
568 SPS Super Proton Synchrotron
569 SCT silicon microstrip
570 TRT transition radiation tracker
571 LAr Liquid Argon
572 EM electromagnetic
573 RPC Resistive Plate Chamber
574 TGC Thin Gap Chamber
575 MDT Monitored Drift Tube
576 CSC Cathode Strip Chamber
577 ToT time over threshold
578 RoI Region of Interest
579 LCW local cluster weighted
580 MIP minimally ionizing particle
581 IP impact parameter

- 582 EPJC European Physical Journal C
583 JES jet energy scale
584 LLP Long-Lived Particle
585 CR Control Region
586 NLO next-to-leading order
587 NLL next-to-leading logarithmic
588 PDF parton distribution function
589 ISR initial state radiation
590 RMS root mean square
591 IBL Insertible B-Layer
592 CP Combined Performance
593 MDT Monitored Drift Tube
594 RF radiofrequency
595 HLT high level trigger

596

PART I

597

INTRODUCTION

598

You can put some informational part preamble text here.

1

599

600 INTRODUCTION

601

PART II

602

THEORETICAL CONTEXT

603

You can put some informational part preamble text here.

2

604

605 STANDARD MODEL

606 The SM of particle physics seeks to explain the symmetries and interactions of
607 all currently discovered fundamental particles. It has been tested by several genera-
608 tions of experiments and has been remarkably successful, no significant de-
609 viations have been found. The SM provides predictions in particle physics for
610 interactions up to the Planck scale (10^{15} - 10^{19} GeV).

611 The theory itself is a quantum field theory grown from an underlying $SU(3) \times$
612 $SU(2) \times U(1)$ that requires the particle content and quantum numbers consist-
613 ent with experimental observations (see Section 2.1). Each postulated symme-
614 try is accompanied by an interaction between particles through gauge invari-
615 ance. These interactions are referred to as the Strong, Weak, and Electromag-
616 netic forces, which are discussed in Section 2.2.

617 Although this model has been very predictive, the theory is incomplete; for
618 example, it is not able to describe gravity or astronomically observed dark matter.
619 These limitations are discussed in more detail in Section 2.3.

620 21 PARTICLES

621 The most familiar matter in the universe is made up of protons, neutrons, and
622 electrons. Protons and neutrons are composite particles, however, and are made
623 up in turn by particles called quarks. Quarks carry both electric charge and color
624 charge, and are bound in color-neutral combinations called baryons. The elec-
625 tron is an example of a lepton, and carries only electric charge. Another type
626 of particle, the neutrino, does not form atomic structures in the same way that
627 quarks and leptons do because it carries no color or electric charge. Collectively,
628 these types of particles are known as fermions, the group of particles with half-
629 integer spin.

630 There are three generations of fermions, although familiar matter is formed
631 predominantly by the first generation. The generations are identical except for
632 their masses, which increase in each generation by convention. In addition, each
633 of these particles is accompanied by an antiparticle, with opposite-sign quantum
634 numbers but the same mass.

635 The fermions comprise what is typically considered matter, but there are
636 additional particles that are mediators of interactions between those fermions.
637 These mediators are known as the gauge bosons, gauge in that their existence
638 is required by gauge invariance (discussed further in Section 2.2) and bosons in
639 that they have integer spin. The boson which mediates the electromagnetic force
640 is the photon, the first boson to be discovered; it has no electric charge, no mass,
641 and a spin of 1. There are three spin-1 mediators of the weak force, the two
642 W bosons and the Z boson. The W bosons have electric charge of ± 1 and a
643 mass of 80.385 ± 0.015 GeV, while the Z boson is neutral and has a mass of

644 91.1876 \pm 0.0021 GeV. The strong force is mediated by eight particles called
 645 gluons, which are massless and electrically neutral but do carry color charge.

646 The final particle present in the SM is the Higgs boson, which was recently
 647 observed for the first time by experiments at CERN in 2012. It is electrically
 648 neutral, has a mass of 125.7 \pm 0.4 GeV, and is the only spin-0 particle yet to be
 649 observed. The Higgs boson is the gauge boson associated with the mechanism
 650 that gives a mass to the W and Z bosons.

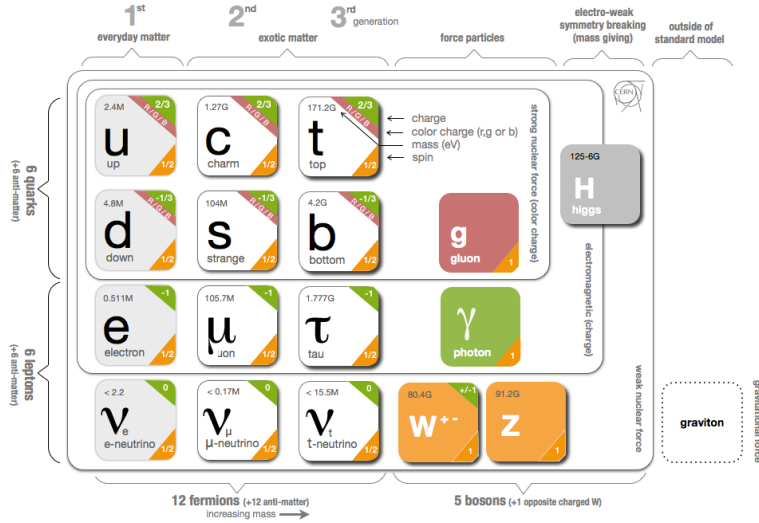


Figure 1: The particle content of the SM.

651 Together these particles form the entire content of the SM, and are summa-
 652 rized in Figure 1. These are the particles that constitute the observable universe
 653 and all the so-far-observed interactions within it.

654 2.2 INTERACTIONS

655 The interactions predicted and described by the SM are fundamentally tied to the
 656 particles within it, both in that they describe the way those particles can influence
 657 each other and also in that the existence of the interactions requires the existence
 658 of some particles (the gauge bosons).

659 2.3 LIMITATIONS

3

660

661 SUPERSYMMETRY

662 3.1 MOTIVATION

663 3.2 STRUCTURE

664 3.3 PHENOMENOLOGY

4

665

666 LONG-LIVED PARTICLES

667 4.1 MECHANISMS

668 4.1.1 EXAMPLES IN SUPERSYMMETRY

669 4.2 PHENOMENOLOGY

670 4.2.1 DISIMILARITIES TO PROMPT DECAYS

671 4.2.2 CHARACTERISTIC SIGNATURES

672

PART III

673

EXPERIMENTAL STRUCTURE AND RECONSTRUCTION

674

You can put some informational part preamble text here.

675

676 THE LARGE HADRON COLLIDER

677 The LHC, a two-ring superconducting hadron accelerator, provides high energy
678 proton-proton collisions for several large experiments at European Organization
679 for Nuclear Research (CERN) in Geneva, Switzerland [1, 2]. It is the largest,
680 highest-luminosity, and highest-energy proton collider ever built, and was con-
681 structed by a collaboration of more than 10,000 scientists from the more than
682 100 countries that contribute to CERN. The original design of the LHC focused on
683 providing collision energies of up to 14 TeV and generating enough collisions to
684 reveal physics beyond the SM which is predicted to exist at higher energy scales.

685 The LHC was installed in an existing 27 km tunnel at CERN which was origi-
686 nally designed to house the Large Electron Positron collider (LEP). This allows
687 the collider to use existing accelerators at the same complex to provide the initial
688 acceleration of protons up to 450 GeV before injecting into LHC. The injected
689 hadrons are accelerated up to as much as 14 TeV while being focused into two
690 beams traveling in opposite directions. During this process the protons circulate
691 around the tunnel millions of times, while the beams are intermittently crossed
692 at the four locations of the experiments to provide collisions. These collision
693 points correspond to the four major LHC experiments: ATLAS, Compact Muon
694 Solenoid (CMS), Large Hadron Collider beauty experiment (LHCb), and A Large
695 Ion Collider Experiment (ALICE), and Figure 2 shows the layout of the exper-
696 iments both on the surface and below. ATLAS and CMS are both general pur-
697 pose, high-luminosity detectors which search for a wide range of new types of
698 physics [3, 4]. LHCb studies the interactions of b-hadrons to explore the asymme-
699 try between matter and antimatter [5]. ALICE focuses on the collisions of lead
700 ions, which the LHC also provides, in order to study the properties of quark-
701 gluon plasma [6].

702 During the first five years of operation, after the LHC turned on in 2010, the
703 LHC has provided four major data collecting periods. In 2010 the LHC generated
704 collisions at several energies, starting at 900 GeV. It increased the energy from
705 900 GeV to 2.76 TeV and then subsequently to 7 TeV, with a peak luminos-
706 ity of $2 \times 10^{32} \text{ cm}^{-2}\text{s}^{-1}$, and a total delivered luminosity of 50 pb^{-1} . The next
707 run, during 2011, continued the operation at 7 TeV and provided an additional 5
708 fb^{-1} with a peak luminosity of $4 \times 10^{33} \text{ cm}^{-2}\text{s}^{-1}$. The energy was then increased
709 to 8 TeV for the data collection during 2012, which provided 23 fb^{-1} with a peak
710 luminosity of $7.7 \times 10^{33} \text{ cm}^{-2}\text{s}^{-1}$. After the first long shutdown for 2013 and
711 2014, the LHC resumed operation and increased the energy to 13 TeV in 2015,
712 where it delivered 4.2 fb^{-1} with a peak luminosity of $5.5 \times 10^{33} \text{ cm}^{-2}\text{s}^{-1}$. The
713 LHC is currently providing additional 13 TeV collisions in 2016 with higher lu-
714 minosities than during any previous data collection periods. These running peri-
715 ods are summarized in Figure 3, which shows the total delivered luminosity over

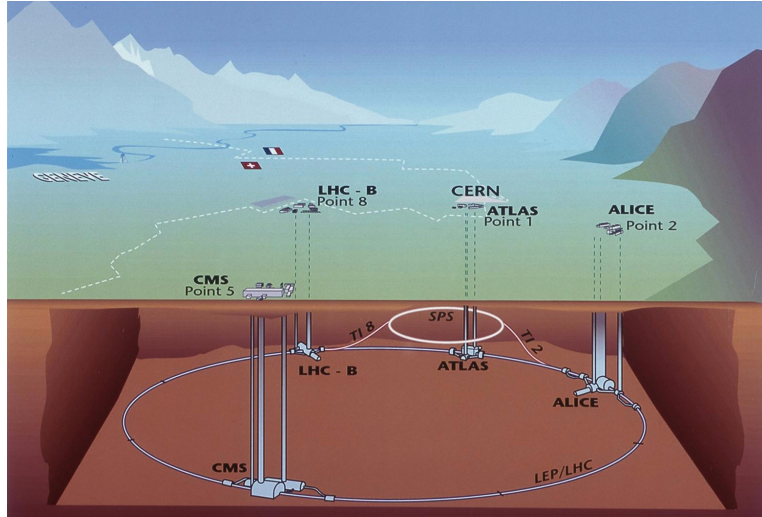


Figure 2: The four collision points and corresponding experiments of the [LHC](#). The image includes the location of the nearby city of Geneva as well as the border of France and Switzerland.

716 time for the [ATLAS](#) experiment during each of the four years of data collection
717 since 2011.

718 5.1 INJECTION CHAIN

719 The [LHC](#) takes advantage of the presence of previously built accelerators at [CERN](#)
720 to work up to the target energy in consecutive stages. The series of accelerators
721 that feed into the [LHC](#) are known collectively as the injection chain, and together
722 with the [LHC](#) form the accelerator complex. The full complex is illustrated in
723 Figure 4, which details the complex series required to reach collisions of 13 or
724 14 TeV.

725 Protons at the [LHC](#) begin as hydrogen atoms in the Linac 2, a linear accelerator
726 which replaced Linac 1 as the primary proton accelerator at CERN in 1978. In
727 Linac 2, the hydrogen atoms are stripped of their electrons by a strong magnetic
728 field, and the resulting protons are accelerated up to 50 MeV by cylindrical con-
729 ductors charged by radio frequency cavities. The protons are then transferred
730 to the Proton Synchrotron Booster ([PSB](#)), which uses a stack of four synchrotron
731 rings to accelerate the protons up to 1.4 GeV. Then the protons are injected
732 into the Proton Synchrotron ([PS](#)) which again uses synchrotron rings to bring
733 the energy up to 25 GeV. The intermediate step between Linac 2 and the [PS](#) is
734 not directly necessary, as the [PS](#) can accelerate protons starting from as low as
735 50 MeV. The inclusion of the [PSB](#) allows the [PS](#) to accept a higher intensity of
736 injection and so increases the deliverable luminosity in the [LHC](#). The penulti-
737 mate stage of acceleration is provided by the Super Proton Synchrotron ([SPS](#)), a
738 large synchrotron with a 7 km circumference that was commissioned at CERN
739 in 1976. During this step the protons increase in energy to 450 GeV, after which
740 they can be directly injected into the [LHC](#).

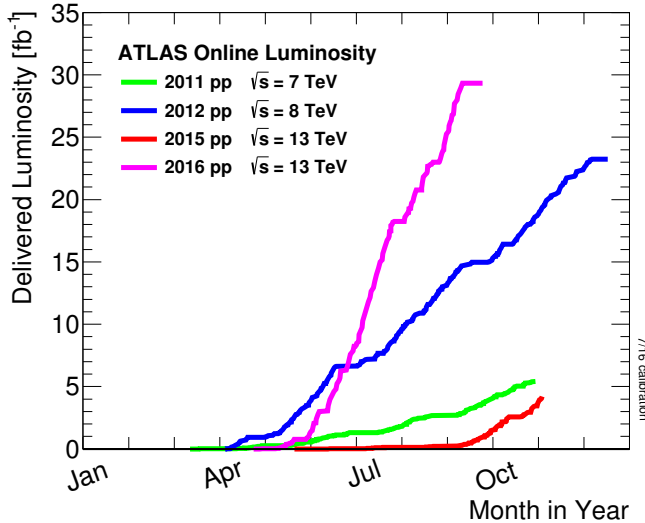


Figure 3: The cumulative luminosity over time delivered to the [ATLAS](#) experiment from high energy proton-proton collisions since 2011. The energies of the collisions are listed for each of the data-taking periods.

The final step is the [LHC](#) itself, which receives protons from the [SPS](#) into two separate beam pipes which circulate in opposite directions. The filling process at this steps takes approximately 4 minutes, and the subsequent acceleration to the final energy (6.5 TeV during 2015 and up to 7 TeV by design) takes approximately half an hour. At this point the protons circulate around the circumference tens of thousands of times a second and continue for up to two hours.

5.2 DESIGN

5.2.1 LAYOUT

Many of the aspects of the [LHC](#) design are driven by the use of the existing [LEP](#) tunnel. This tunnel slopes gradually, with a 1.4% decline, with 90% of its length built into molasse rock which is particularly well suited to the application. The circumference is composed of eight 2987 meter arcs and eight 528 meter straight sections which connect them; this configuration is illustrated in Figure 5. The tunnel diameter is 3.7 m throughout its length.

The design energy is directly limited by the size of this tunnel, with its radius of curvature of 2804 m. A significant magnetic field is required to curve the protons around that radius of curvature; the relationship is given by

$$p \simeq 0.3BR \quad (1)$$

where p is the momentum of the particle in GeV, B is the magnetic field in Tesla, and R is the radius of curvature in meters. From the target design energy of 14 TeV, or 7 TeV of momentum for protons in each beam, the required magnetic field is 8.33 Tesla. This is too large a field strength to be practical with

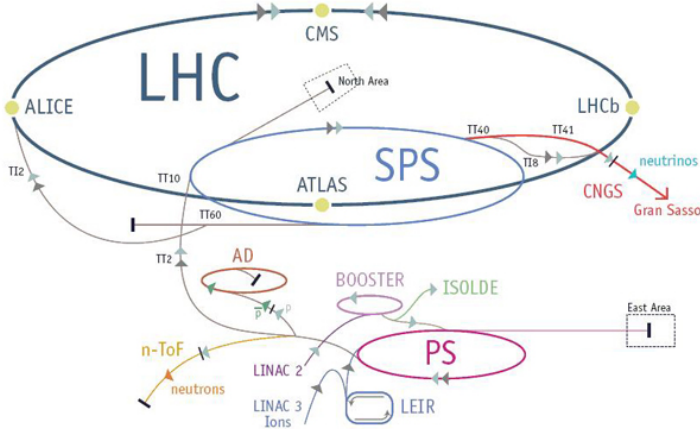


Figure 4: The accelerator complex that builds up to the full design energies at the [LHC](#). The protons are passed in order to Linac 2, the [PSB](#), the [PS](#), the [SPS](#) and then the [LHC](#).

iron electromagnets, because of the enormous power required and the resulting requirements for cooling. Because of these constraints, the [LHC](#) uses superconducting magnets which can maintain that field strength with significantly less power consumption.

5.2.2 MAGNETS

Specifically the magnets chosen were Niobium and Titanium (NbTi) which allow for field strengths as high as 10 Tesla when cooled down to 1.9 K. Reaching the target temperature of 1.9 K for all of the magnets requires superfluid helium and a large cryogenic system along the entire length of the tunnel. During normal operation, the [LHC](#) uses 120 tonnes of helium within the magnets, and the entire system is cooled by eight cryogenic helium refrigerators. The temperature increase that occurs during transit from the refrigerator along the beam necessitates that the refrigerators cool the helium down to 1.8 K. Any significant increase above this temperature range can remove the superconductive properties of the magnets, which in turn generates drastically larger heat losses from the current within the magnets and causes a rapid rise in temperature called a quench.

In all there are approximately 8000 superconducting magnets distributed around the [LHC](#). The 1232 bending magnets, which keep the protons curving along the length of the beam, are twin bore cryodipoles, which allow both proton beams to be accommodated by one magnet and all of the associated cooling structure. Figure 6 shows the cross section of the design for these dipoles. The magnets are very large, 16.5 m long with a diameter of 0.57 meters and a total weight of 28 tonnes. They are slightly curved, with an angle of 5.1 mrad, in order to carefully match the beam path. The twin bore accommodates both magnets inside the two 5 cm diameter holes which are surrounded by the superconducting coils. The coils require 12 kA of current in order to produce the required magnetic

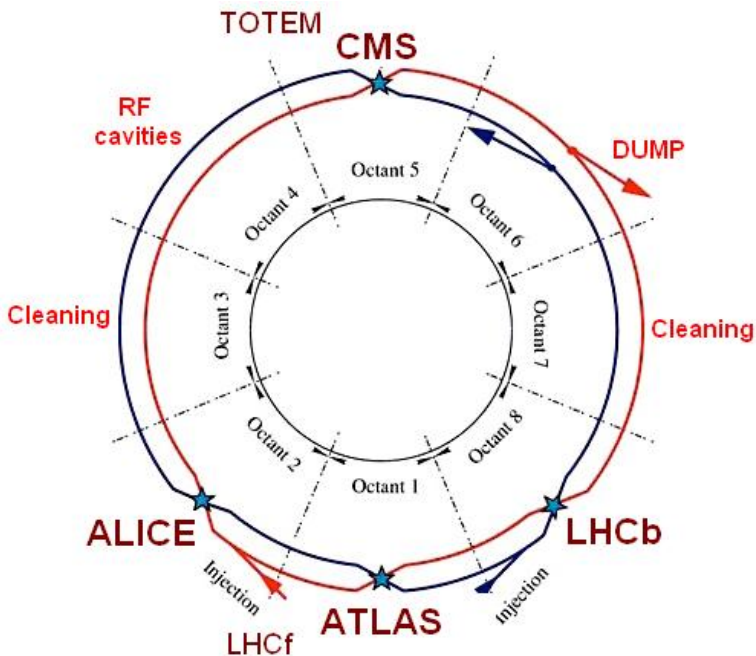


Figure 5: A schematic of the layout of the LHC, not to scale. The arched and straight sections are illustrated at the bottom of the schematic, and all four crossing sites are indicated with their respective experiments.

789 field. These coils are comprised of NbTi cable wound in two layers; the wire in
 790 the inner layer has a diameter of 1.065 mm while the wire in the outer layer has
 791 a diameter of 0.825 mm.

792 The large currents in the wires, along with the magnetic field produced, result
 793 in forces on the magnets which would tend to push them apart with over 10,000
 794 Newtons per meter. Constraining the magnets requires a significant amount of
 795 structure including non-magnetic stainless steel collars. Both the presence of
 796 these electromagnetic forces and the varying thermal contraction coefficient of
 797 the pieces of the magnet produce significant forces on the cold mass structure.
 798 The cold mass is carefully engineered to so that these stresses do not significantly
 799 alter the magnetic field shape, which must be maintained between magnets to a
 800 precision of approximately 10^{-4} for successful operation.

801 The remaining 6800 magnets are a variety of quadrupole, sextapole, octopole,
 802 and single bore dipole magnets. These are used to damp oscillations, correct
 803 beam trajectories, focus the beams during circulation, and to squeeze the beams
 804 before collisions.

805 5.2.3 RF CAVITIES

806 Sixteen RF cavities produce the actual acceleration of the proton beam up to the
 807 design energy. These RF cavities are tuned to operate at 400 MHz, and are pow-
 808 ered by high-powered electron beams modulated at the same frequency, called
 809 klystrons. The resonance within the cavity with the oscillating electric field
 810 establishes a voltage differential of 2 MV per cavity. The sixteen cavities are

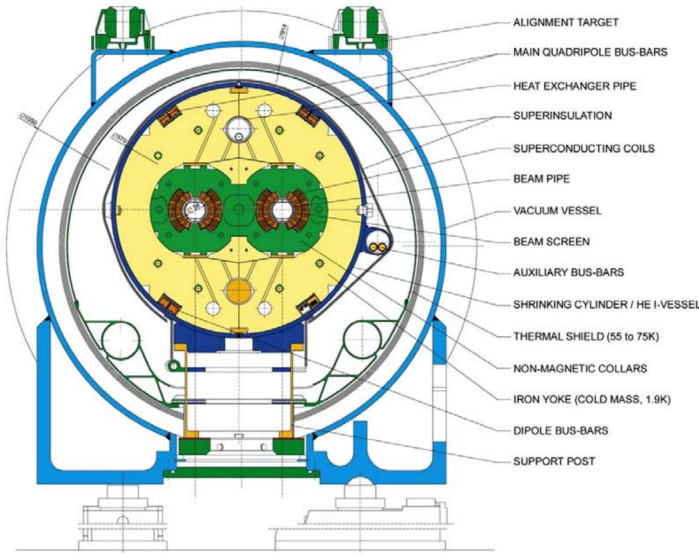


Figure 6: A cross section of the cryodipole magnets which bend the flight path of protons around the circumference of the LHC. The diagram includes both the superconducting coils which produce the magnetic field and the structural elements which keep the magnets precisely aligned.

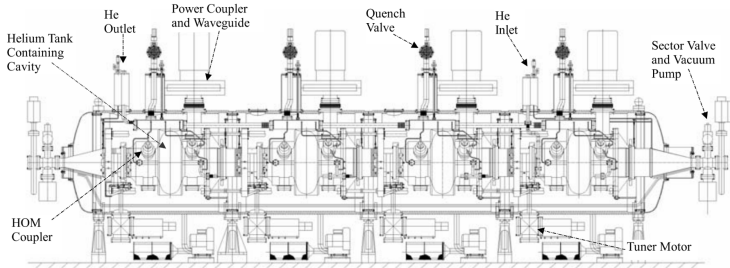


Figure 7: The arrangement of four RF cavities within a cryomodule.

split between the two beams, so combined the cavities provide 16 MV per beam, which accelerate the protons on each consecutive pass through the cavity. This acceleration is also necessary during circulation even after the target energy has been reached in order to compensate for losses from synchrotron radiation.

The cavities are arranged in cryomodules which contain four cavities, with two cryomodules per beam; this arrangement is illustrated in Figure 7. These cryomodules are necessary to maintain the superconducting state of the cavities, which are also constructed from niobium. The RF cavities use niobium along with copper to allow for low power losses in the superconductors. The copper provides a reduced susceptibility to quenching, as it rapidly conducts away heat generated by imperfections in the niobium, as well as natural shielding from the earth's magnetic field which can interfere with the RF system.

The nature of the radio frequency oscillations tends to group protons together into buckets. A proton traveling exactly in phase with the RF oscillations will not be displaced at all during a single circulation, and those slightly ahead or behind

826 of that phase will slightly decelerate or accelerate, respectively. This produces
 827 separate clusters of protons which arrive in phase to the cavities every 2.5 ns,
 828 corresponding to the 400 MHz frequency.

829 5.2.4 BEAM

830 The beams of protons circulate within 54 km of 5 cm diameter beam pipe. This
 831 entire structure is kept under vacuum at 1.9 K to prevent interactions between
 832 the beam pipe and the magnets as well as to prevent any interactions between the
 833 circulating protons and gas in the pipe. The vacuum within the pipe establishes
 834 a pressure as low as 10^{-9} mbar before the protons are introduced.

835 Because of the very high energies of the circulating protons, synchrotron ra-
 836 diation is not negligible in the bending regions. The protons are expected to
 837 radiate 3.9 kW per beam at 14 TeV, with 0.22 W/m, which is enough power to
 838 heat the liquid helium and cause a quench were it absorbed by the magnets. To
 839 prevent this, a copper screen is placed within the vacuum tube that absorb the
 840 emitted photons. This screen is kept between 5 and 20 K by the liquid helium
 841 cooling system.

842 5.3 LUMINOSITY PARAMETERS

843 In addition to the high energy of the collisions, the rate of collisions is extremely
 844 important to enabling the discovery of new physics. Many measurements and
 845 searches require a large number of events in order to be able to make statistically
 846 significant conclusions. The rate of collisions is measured using luminosity, the
 847 number of collisions per unit time and unit cross section for the proton-proton
 848 collisions. From the beam parameters, luminosity is given by

$$\mathcal{L} = \frac{N_b^2 n_b f_{rev} \gamma}{4\pi\epsilon_n \beta^*} F \quad (2)$$

849 where N_b is the number of protons per bunch, n_b is the number of bunches per
 850 beam, f_{rev} is the frequency of revolution, γ is the Lorentz factor for the protons
 851 at the circulating energy, ϵ_n is the emittance, β^* is the amplitude function at the
 852 collision point, and F is a geometric factor that accounts for the crossing angle of
 853 the beams at the collision point. The emittance measures the average spread of
 854 particles in both position and momentum space, while the amplitude function
 855 is a beam parameter which measures how much the beam has been squeezed.
 856 Together ϵ_n and β^* give the size of the beam in the transverse direction, $\sigma = \sqrt{\epsilon\beta^*}$. β
 857 changes over the length of the beam as the accessory magnets shape the
 858 distribution of protons, but only the value at the point of collisions, β^* , affects
 859 the luminosity.

860 The luminosity is maximized to the extent possible by tuning the parameters
 861 in Equation 2. A number of these are constrained by the design decisions. The
 862 revolution frequency is determined entirely by the length of the tunnel, as the

Parameter	Unit	Injection	Nominal
Beam Energy	TeV	0.450	7
Peak Instantaneous Luminosity	$\text{cm}^{-2}\text{s}^{-1}$	-	10^{34}
Bunch Spacing	ns	25	25
Number of Filled Bunches	-	2808	2808
Normalized Transverse Emittance	μm	3.75	3.75
Frequency	MHz	400.789	400.790
RF Voltage/Beam	MV	8	16
Stored Energy	MJ	-	362
Magnetic Field	T	0.54	8.33
Operating Temperature	K	1.9	1.9

Table 1: The design parameters of the [LHC](#) beam that determines the energy of collisions and the luminosity, for both the injection of protons and at the nominal circulation.

863 protons travel at very close to the speed of light. The geometric factor F is de-
 864 termined by the crossing angle of the beams at the collision points, again a com-
 865 ponent of the tunnel design; this angle is already very small at $285 \mu\text{rad}$, which
 866 helps to maximize the geometric factor.

867 The major pieces that can be adjusted are the number of protons per bunch,
 868 N_b , the number of bunches in the beam, n_b , and the amplitude function β . In-
 869 creasing either N_b or n_b increases the amount of energy stored in the beam,
 870 which presents a danger if control of the beam is lost. At design specifications,
 871 the beam stores 362 MJ, which is enough energy to damage the detectors or ac-
 872 celerator if the beam were to wander out of the beam pipe. So, the luminosity
 873 is primarily controlled at the [LHC](#) by adjusting β^* , where lowering β^* increases
 874 the luminosity. β^* is tuned to provide the various values of luminosity used at
 875 the [LHC](#) which can be raised to as much as 10^{34} .

876 The nominal bunch structure consists of 3654 bunches, each holding 10^{11} pro-
 877 tons, which cross a collision point in 25 ns. These are further subdivided into the
 878 buckets mentioned in Section 5.2.3 by the clustering properties of the RF cavities.
 879 The bunches are further grouped into trains of 72 bunches which are separated
 880 by a gap which would otherwise hold 12 bunches. At nominal operation 2808
 881 of the bunches will actually be filled with protons, while the remainder are left
 882 empty to form an abort gap that can be used in case the beam needs to be dumped.

883 The various beam parameters are summarized in Table 1 for the designed op-
 884 eration. In practice the beam has operated at lower energies and lower luminosi-
 885 ties than the design values, but the [LHC](#) is expected to operate at the full design
 886 values during Run 2.

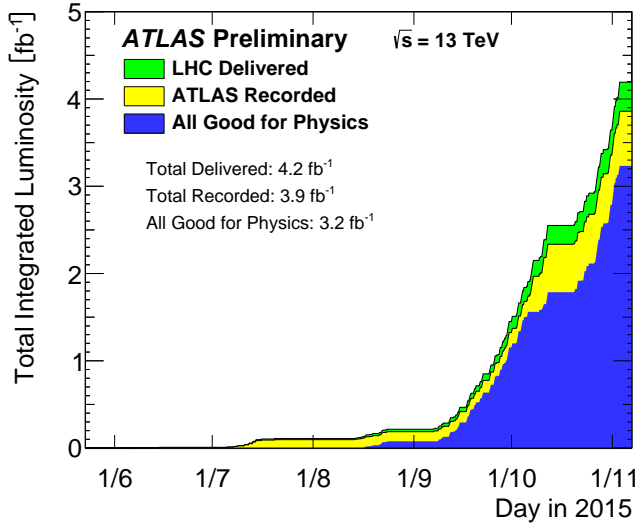


Figure 8: The cumulative luminosity versus time delivered to ATLAS (green), recorded by ATLAS (yellow), and certified to be good quality data (blue) during stable beams for pp collisions at 13 TeV in 2015.

5.4 DELIVERED LUMINOSITY

During the data collection of 2015, the [LHC](#) operated at luminosities as large as 5×10^{33} . It is convenient to refer to the integrated luminosity, the integral of the instantaneous luminosity, which corresponds directly to the number of delivered events for a given process.

$$N = \sigma \times \int \mathcal{L}(t) dt$$

where σ is the cross section for the process of interest. The integrated luminosity over time is shown in Figure 8. This includes the luminosity delivered by the [LHC](#) as well as the luminosity that was recorded by [ATLAS](#). Some of the delivered luminosity is not recorded because [ATLAS](#) is placed in standby until the [LHC](#) reports that the beam conditions are stable, and only then does [ATLAS](#) begin recording. The figure also includes the amount of luminosity marked as good for physics, which includes additional requirements on the operation of the detector during data collection that are necessary for precise measurements.

In addition to the instantaneous luminosity, the beam conditions also influence the number of collisions that occur within a single bunch crossing. The multiple interactions at each crossing are referred to as pileup, often denoted μ , and each of these interactions are present in a single measured event. Figure 9 shows the luminosity-weighted distribution of the mean number of interactions for events collected in 2015. The presence of as many as 20 events in a single collision provides a significant challenge in reconstructing events and isolating the targeted physical processes.

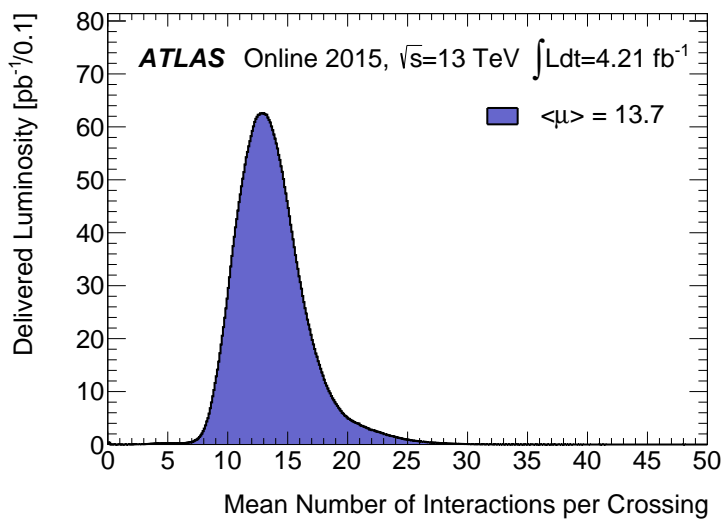


Figure 9: The luminosity-weighted distribution of the mean number of interactions per crossing for the 2015 pp collision data at 13 TeV.

904

905 THE ATLAS DETECTOR

906 The four major LHC experiments at CERN seek to use the never before matched
907 energies and luminosities of the new collider to explore the boundaries of par-
908 ticle physics and to gain insight into the fundamental forces of nature. Two of
909 these experiments, ATLAS and CMS, are general purpose detectors that seek to
910 measure a variety of processes in the up to 14 TeV proton-proton collisions that
911 occur as much as 40 million times per second at the LHC at the design luminosity
912 of $10^{34} \text{ cm}^{-2}\text{s}^{-1}$. ATLAS employs a hermetic detector design, one which encloses
913 the particle collisions as completely as possible with detecting elements, that al-
914 lows it to study a wide range of physics from SM and Higgs measurements to
915 searches for new physics in models like Supersymmetry [3].

916 Accommodating this wide variety of goals is a challenge for the design of
917 the detector. The wide range of energies involved requires high measurement
918 precision over several orders of magnitude and the ability to measure a vari-
919 ety of particle types. At the time of the construction of ATLAS, the Higgs bo-
920 son had yet to be discovered, but the diphoton decay mode was (correctly) ex-
921 pected to be important and necessitated a high resolution photon measurement.
922 The potential for decays of new heavy gauge bosons, W' and Z' , required a simi-
923 larly high momentum resolution for leptons with momentum up to several TeV.
924 Hadronic decay modes of several possible new high energy particles could re-
925 sult in very energetic jets, again up to several TeV, and reconstructing the decay
926 resonances would again require good energy resolution. Several models, such
927 as Supersymmetry (SUSY) or Extra Dimensions, predict the existence of particles
928 which would not interact with traditional detecting elements. However these
929 particles can still be observed in a hermetic detector by accurately measuring
930 the remaining event constituents to observe an imbalance in energy called miss-
931 ing energy or E_T^{miss} . Measuring E_T^{miss} implicitly requires a good resolution on all
932 SM particles that can be produced. And at the lower end of the energy spectrum,
933 precision SM measurements would require good resolution of a variety of parti-
934 cle types at energies as low as a few GeV, so the design needs to accommodate
935 roughly three orders of magnitude.

936 This broad spectrum of measurements requires a variety of detector systems
937 working together to form a cohesive picture of each collision. Two large magnet
938 systems provide magnetic fields that provide a curvature to the propagation of
939 charged particles and allows for precision momentum measurements by other
940 systems. The inner detector uses a combination of tracking technologies to re-
941 construct particle trajectories and vertices for charged particles. A variety of
942 calorimeters measure the energies of hadrons, electrons, and photons over a
943 large solid angle. A large muon spectrometer identifies muons and uses the sec-
944 ond magnet system to provide an independent measurement of their momentum

945 from the inner detector and improve the resolution. The layout of all of these
 946 systems is shown in Figure 10.

947 The performance goals needed to achieve the various targeted measurements
 948 and searches discussed above can be summarized as resolution and coverage re-
 949 quirements on each of these systems. Those requirements are listed in Table 2.

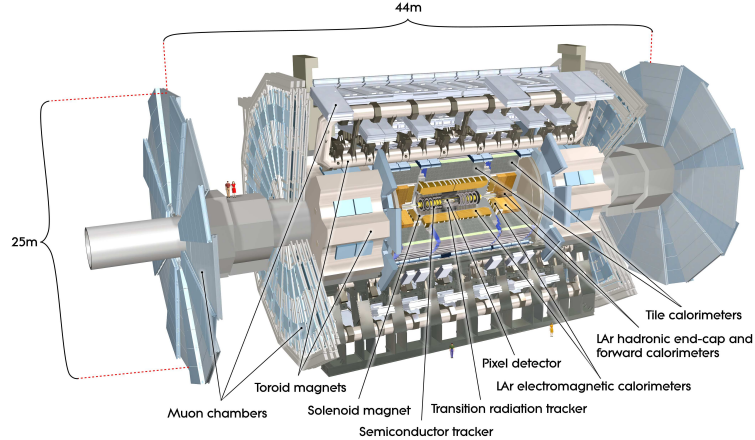


Figure 10: A cut-away schematic of the layout of the [ATLAS](#) detector. Each of the major subsystems is indicated.

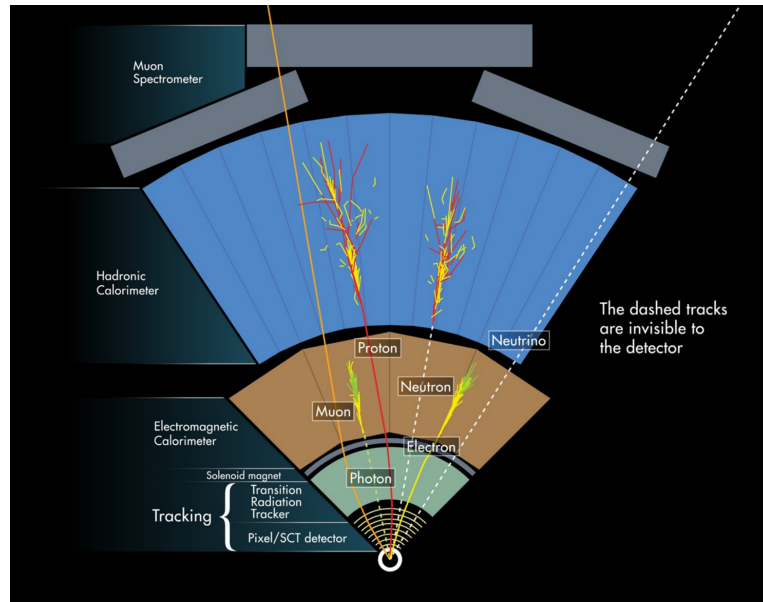


Figure 11: A cross-sectional slice of the [ATLAS](#) experiment which illustrates how the various SM particles interact with the detector systems.

950 Incorporating these various pieces into a single detector is a significant tech-
 951 nical challenge. The resulting detector has a diameter of 22 m, is 46 m long,
 952 and weighs 7,000 tons; it is the largest volume particle detector ever constructed.
 953 The various detector elements need to be constructed and assembled with pre-
 954 cision as low as micrometers. These systems all need to function well even after
 955 exposure to the significant radiation dose from the collisions. Designing, con-

Detector Component	Required Resolution	$ \eta $ Coverage	
		Measurement	Trigger
Tracking	$\sigma_{p_T}/p_T = 0.05\% p_T + 1\%$	2.5	-
EM Calorimetry	$\sigma_E/E = 10\%/\sqrt{E} + 0.7\%$	3.2	2.5
Hadronic Calorimetry			
Barrel and Endcap	$\sigma_E/E = 50\%/\sqrt{E} + 3\%$	3.2	3.2
Forward	$\sigma_E/E = 100\%/\sqrt{E} + 10\%$	3.1 – 4.9	3.1 – 4.9
Muon Spectrometer	$\sigma_{p_T}/p_T = 10\% \text{ at } p_T = 1 \text{ TeV}$	2.7	2.4

Table 2: The performance goals for each of the subsystems of the [ATLAS](#) detector. The $|\eta|$ coverage specifies the range where the subsystem needs to be able to provide measurements with the specified resolution. The resolutions include a p_T or E dependence that is added in quadrature with a p_T/E independent piece.

956 structing, and installing the detector took the combined effort of more than 3000
 957 scientists from 38 countries over almost two decades.

958 6.1 COORDINATE SYSTEM

959 The coordinate system defined for the [ATLAS](#) detector is used throughout all of
 960 the sections of this thesis. The choice of coordinate system reflects the cylind-
 961 drical symmetry of the [ATLAS](#) detector, and is oriented by the direction of the
 962 beamline which defines the z -direction. The positive z side of the detector is
 963 commonly referred to as the A -side, and the negative z side is referred to as
 964 the C -side. The $x - y$ plane is then the plane transverse to the beam direction,
 965 with the x direction defined as pointing from the interaction point to the center
 966 of the [LHC](#) ring and the y direction defined as pointing upwards. The nominal
 967 interaction point is the origin of this system.

968 It is more convenient in practice to use a cylindrical coordinate system. The
 969 angle from the z -axis is θ . The azimuthal angle uses the usual definition, with ϕ
 970 running around the z -axis and $\phi = 0$ corresponding to the x -axis. Many aspects
 971 of the detector are independent of the this coordinate to first order. The re-
 972 maining direction is typically specified using rapidity or pseudorapidity, where
 973 rapidity is defined as

$$y = \frac{1}{2} \ln \frac{E + p_z}{E - p_z} \quad (3)$$

974 Rapidity is particularly useful to indicate the component along the z direction
 975 because differences in rapidity are invariant to boosts along the z -direction. A
 976 similar quantity which depends only the θ is pseudorapidity,

$$\eta = -\ln \tan \frac{\theta}{2} \quad (4)$$

977 which is the same as rapidity when the particle is massless and in the limit where
 978 the energy is much larger than the particle's mass. It is often useful to refer to
 979 differences in solid angle using the pseudorapidity and the azimuthal angle:

$$\Delta R = \sqrt{\Delta\phi^2 + \Delta\eta^2} \quad (5)$$

980 The pseudorapidity is also invariant to boosts along the z -axis for high mo-
 981 mentum particles, and is preferable to rapidity because it does not depend on
 982 the specific choice of particle. Pseudorapidity is also preferable to θ because
 983 of the aforementioned boost-invariance and also because particle production is
 984 roughly uniform in equal-width intervals of η up to about $\eta = 5.0$. A particle
 985 traveling along the beampipe has $\eta = \text{inf}$ and a particle traveling perpendicular
 986 to the beampipe has $\eta = 0$. The extent of the tracker, $|\eta| < 2.5$, corresponds
 987 to approximately $0.05\pi < \theta[\text{rad}] < 0.95\pi$ and the extent of the calorimeters,
 988 $|\eta| < 4.9$ corresponds to approximately $0.005\pi < \theta[\text{rad}] < 0.995\pi$. Many de-
 989 tector components are broken into multiple subsystems to provide coverage at
 990 greater $|\eta|$. The lower $|\eta|$ region is referred to as the barrel, typically with $|\eta| \lesssim 2$,
 991 and the greater $|\eta|$ region is often referred to as the endcap.

992 The initial energy and momentum of a proton-proton collision along the z di-
 993 rection is unknown in hadron colliders because different energies and momenta
 994 can be carried by the partons. Along the transverse plane, however, the vector
 995 sum of momentum will be zero. For this reason, many physical quantities are
 996 quantified in terms of their projection onto the transverse plan, such as p_T or
 997 E_T . In addition, p_T alone determines the amount of curvature in the magnetic
 998 field, and can be measured independently by measuring the curvature of a parti-
 999 cle's propagation.

1000 6.2 MAGNETIC FIELD

1001 The magnet system used in [ATLAS](#) is designed to provide a substantial magnetic
 1002 field in the two regions where the trajectory of particles is measured, the inner
 1003 detector and the muon spectrometer. The magnetic field provides a curvature
 1004 to the trajectory of charged particles and allows the precision tracking measure-
 1005 ments to make high resolutions measurements of p_T . To provide a magnetic field
 1006 in these regions, [ATLAS](#) uses a hybrid system with four separate, superconduct-
 1007 ing magnets. A single solenoid provides a 2 T axial magnetic field for the inner
 1008 detector, while a barrel toroid and two endcap toroids produce a magnetic field
 1009 of 0.5 and 1 T, respectively, for the muon detectors. This geometry is illustrated
 1010 in Figure 12, and the parameters of the three magnet systems are summarized in
 1011 Table 3.

1012 The central solenoid uses a single-layer coil with a current of 7.730 kA to gen-
 1013 erate the 2 T axial field at the center of the magnet. The single-layer coil design
 1014 enables a minimal amount of material to be used in the solenoid's construction,
 1015 which is important because the solenoid is placed between the inner detector
 1016 and the calorimeters. At normal incidence the magnet has only 0.66 radiation
 1017 lengths worth of material, where one radiation length is the mean distance over

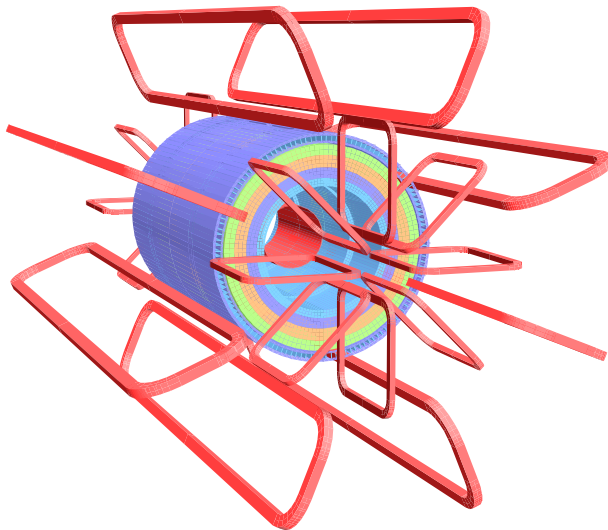


Figure 12: The layout of the four superconducting magnets in the [ATLAS](#) detector.

Parameter	Unit	Solenoid	Barrel Toroid	Endcap Toroids
Inner Diameter	m	2.4	9.4	1.7
Outer Diameter	m	2.6	20.1	10.7
Axial Length	m	5.3	25.3	5.0
Weight	tons	5.7	830	239
Conductor Size	mm ²	30×4.25	57×12	41×4.25
Peak Field	T	2.6	3.9	4.1
Heat Load	W	130	990	330
Current	kA	7.7	20.5	20.0
Stored Energy	MJ	38	1080	206

Table 3: A summary of the parameters of each of the three magnet systems on [ATLAS](#).

1018 which a high-energy electron loses all but $1/e$ of its energy through material in-
 1019 teractions [7]. The coil is made of a high-strength aluminum stabilized NbTi
 1020 superconductor which was optimized to achieve a high field with minimal thick-
 1021 ness. The axial magnetic field produced by the solenoid bends charged particles
 1022 in the ϕ direction.

1023 The barrel toroid consists of eight coils which generate a 0.5 T magnetic field
 1024 in the cylindrical region around the calorimeters with an approximately 20 kA
 1025 current. The coils are separated only by air to reduce the scattering of muons as
 1026 they propagate through the region. The coils are made of an aluminum stabilized
 1027 NbTiCu superconductor and each is separately housed in a vacuum and cold
 1028 chamber. This magnetic configuration produces a field in the ϕ and so curves
 1029 muons traversing the volume primarily in the η direction.

1030 The endcap toroids follow a similar design to the barrel toroid, with eight
 1031 separate NbTiCu coils, but in this case all eight are housed within a single cold
 1032 mass. This extra structure is necessary to withstand the Lorentz forces exerted
 1033 by the magnets. These magnets are rotated 22.5% relative to the barrel toroid to
 1034 provide a uniform field in the transition between the two systems. The endcap
 1035 toroids also produce a field in the ϕ direction and curve muons primarily in the
 1036 η direction.

1037 6.3 INNER DETECTOR

1038 The [ATLAS](#) inner detector provides excellent momentum resolution as well as
 1039 accurate primary and secondary vertex measurements through robust pattern
 1040 recognition that identifies tracks left by charged particles. These tracks fulfill
 1041 a number of important roles in the [ATLAS](#) measurement system: they measure
 1042 the momentum of charged particles including electrons and muons, they can
 1043 identify electrons or photon conversions, they assign various particles and jets
 1044 to different vertices, and they provide a correction to E_T^{miss} measurements from
 1045 low energy particles. The system has to be accurate enough to separate tracks
 1046 from dozens of vertices and to resolve each vertex individually, as well as accu-
 1047 rate enough to measure the p_T of very high momentum tracks which curve very
 1048 little even in the large magnetic field. This is accomplished by several indepen-
 1049 dent layers of tracking systems. Closest to the interaction point is the very high
 1050 granularity Pixel detector, which is followed by the [SCT](#) layers. These subdetec-
 1051 tors both use discrete space-points to reconstruct track patterns. The final layer,
 1052 the transition radiation tracker ([TRT](#)), uses many layers of straw tube elements
 1053 interleaved with transition radiation material to provide continuous tracking.
 1054 The arrangement of these subdetectors is shown in Figure 13. To provide the
 1055 desired hermetic coverage, the subdetectors are divided into barrel and endcap
 1056 geometries. Figure 14 shows the layout of the subdetectors in more detail, and
 1057 illustrates how tracks at various pseudorapidities can traverse the subdetectors;
 1058 tracks with $\eta > 1.1$ begin to traverse the endcap subdetectors rather than those
 1059 in the barrel, and tracks with $\eta > 1.7$ use primarily endcap elements. The [IBL](#)
 1060 was not present during the original commissioning of the inner detector and is
 1061 not shown in this figure.

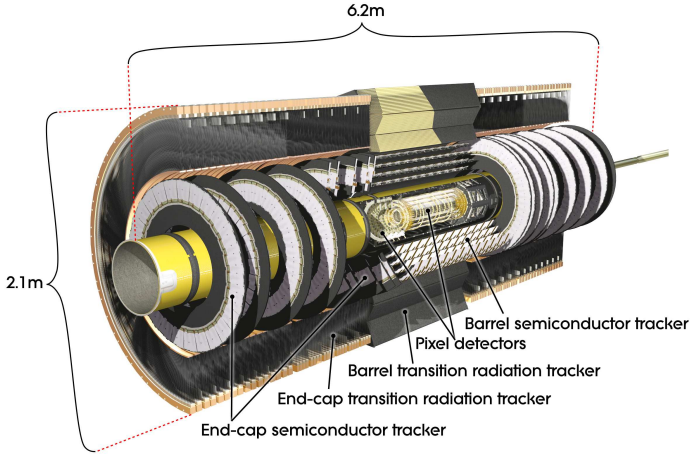


Figure 13: The arrangement of the subdetectors of the ATLAS inner detector. Each of the subdetectors is labeled in the cut-away view of the system.

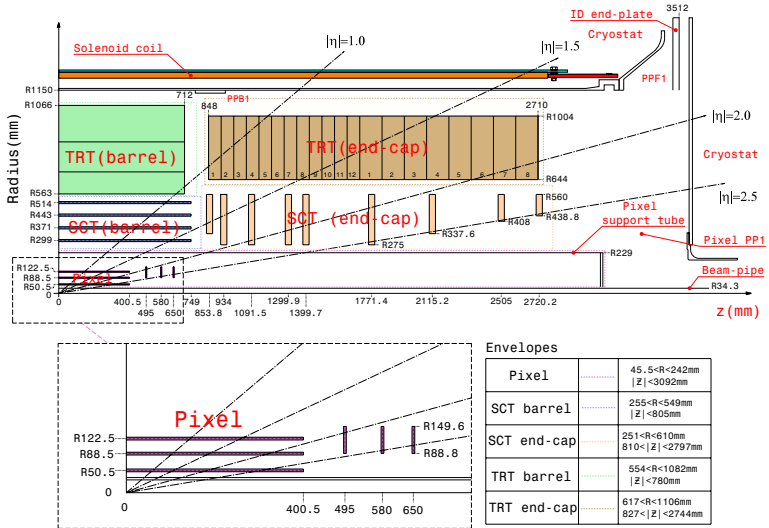


Figure 14: A quarter section of the ATLAS inner detector which shows the layout of each of the subdetectors in detail. The lower panel shows an enlarged view of the pixel detector. Example trajectories for a particle with $\eta = 1.0, 1.5, 2.0, 2.5$ are shown. The IBL, which was added after the original detector commissioning, is not shown.

1062 Figure 15 shows a computer generated three-dimensional view of the inner
 1063 detector along the beam axis, which emphasizes the straw tube structure of the
 1064 **TRT** as well as the overlapping geometry of the **SCT**. This figure also includes
 1065 the **IBL**, which was added during the long shutdown and provides an additional
 1066 measurement layer in the Pixel detector as of the beginning of Run 2. Figure 16
 1067 shows an alternative computer generated three-dimensional view transverse to
 1068 the beam axis which emphasizes the endcap structures of the **SCT** and **TRT**.

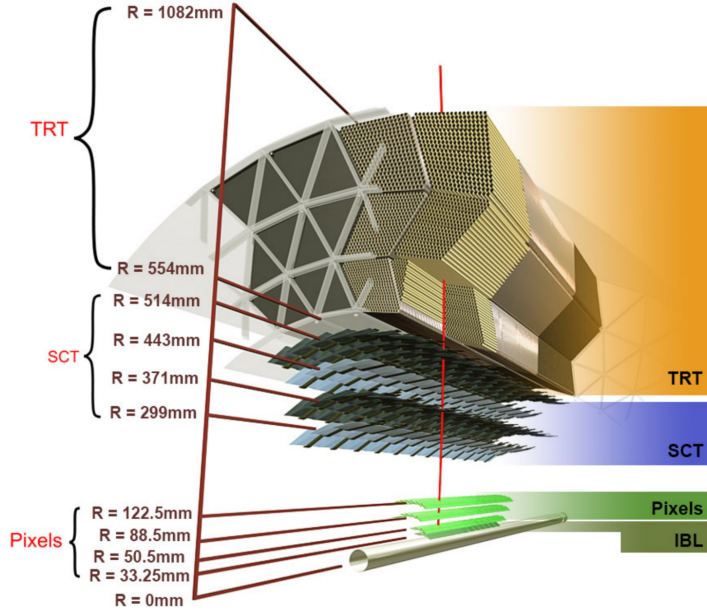


Figure 15: A computer generated three-dimensional view of the inner detector along the line of the beam axis. The subdetectors and their positions are labeled.

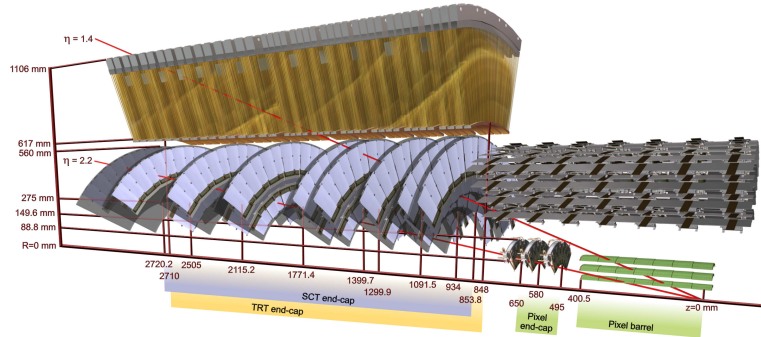


Figure 16: An alternative computer generated three-dimensional view of the inner detector transverse to the beam axis. The subdetectors and their positions are labeled.

1069 As the closest system to the interaction point, it is crucial for the inner de-
 1070 tector to use as little material as possible to avoid scattering of charged parti-
 1071 cles or photon conversions before they reach the remaining subdetectors. The
 1072 various components, including the readout electronics, cooling infrastructure,
 1073 gas volumes, and support structures, were designed to use as little material as

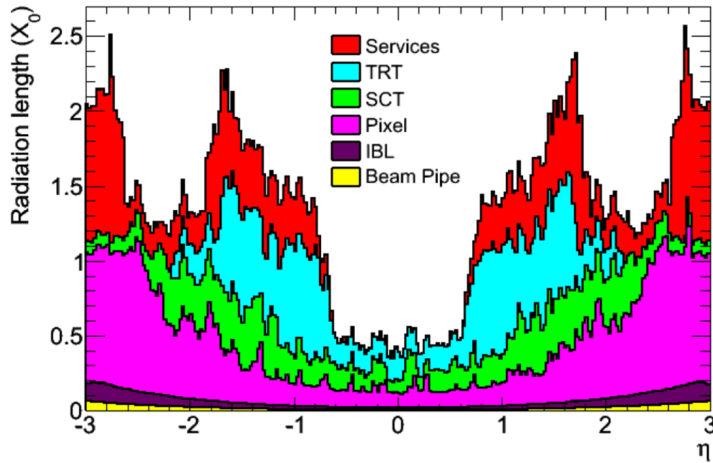


Figure 17: The integrated radiation lengths traversed by a straight track at the exit of the ID envelope, including the services and thermal enclosures. The distribution is shown as a function of $|\eta|$ and averaged over ϕ . The breakdown indicates the contributions of individual sub-detectors, including services in their active volume.

possible. Even with these optimizations, the combination of stringent performance requirements and the harsh radiation environment in the inner detector requires a significant amount of material. This material causes many electrons to lose most of their energy before reaching the electromagnetic calorimeter and approximately 40% of photons convert into an electron-positron pair while traversing the inner detector. Figure 17 shows the integrated radiation lengths traversed by a straight track in the inner detector as a function of η , grouped by subdetector. There is a large increase in the amount of material for support structures around $|\eta| = 1.7$, where the inner detector transitions from barrel to endcap.

The inner detector is designed to work as a cohesive unit to provide complete tracking information for charged particulars, and the subdetectors are complementary. Table 4 summarizes the parameters of each of the subdetectors as well as the parameters of the combined inner detector. Table 5 summarizes the expected performance that can be achieved by the inner detector as a whole.

6.3.1 PIXEL DETECTOR

The Pixel detector is the closest detector to the interaction point and therefore is designed to provide extremely high granularity while simultaneously handling a very large dose of radiation from collisions. It consists of four layers of silicon pixel modules, each of which provides a precision measurement on the trajectory of any charged particle. In the barrel region, the four layers are located at radial distances of 31 mm, 51 mm, 89 mm, and 123 mm. The three outer layers also include endcap elements, illustrated in Figure 14, which are located at 495 mm, 580 mm, and 650 mm away from the interaction point.

Parameter	Inner Detector	Pixel	SCT	TRT
Inner Radius	3.1 cm	3.1 cm	30 cm	56 cm
$ \eta $ Coverage	-	2.5	2.5	2.0
Cell Width	-	50 μm	80 μm	4 mm
Cell Length	-	400 μm	12 cm	70 cm
Material at $ \eta = 0.0$	$0.3 X/X_0$			
Material at $ \eta = 1.7$	$1.2 X/X_0$			
Material at $ \eta = 2.5$	$0.5 X/X_0$			
Number of Hits	48	4	8	36
Channels	99 M	92 M	6.3 M	350 k

Table 4: A summary of the parameters of the inner detector and each of the subdetectors [3].

1098 The pixel sensor technology uses a p-n junction of n-type bulk that contains
 1099 both p⁺ and n⁺ impurities. This combination is crucial in maintaining perfor-
 1100 mance after a significant radiation dose, as the n⁺ implants allow the sensor to
 1101 continue function after the n-type bulk has been converted to a p-type bulk by
 1102 the accumulation of radiation.

1103 The size of the pixels in the original three layers are 50 $\mu\text{m} \times$ 400 μm in the
 1104 $r - \phi$ and z directions, respectively. Those pixels are bump-bonded to front-end
 1105 readout chips, the FE-I3, which contains a total of 2880 pixels per chip. In the
 1106 three original pixel layers, the chips are grouped into modules composed of 16
 1107 chips each with 46,080 pixels per module and a total size of 20 mm x 60 mm
 1108 x 250 μm . The modules are further arranged into long rectangular structures
 1109 that run parallel to the beamline called staves. By tiling several staves with an
 1110 offset of 20°, the stave geometry provides full azimuthal coverage in the barrel
 1111 region while accommodating the readout and cable systems. The endcap regions
 1112 are instead arranged into petals and then into wheels. This arrangement can be
 1113 seen in Figure 18 which shows a computer-generated, cut-away image of the
 1114 outer three layers of the pixel detector. Together these three layers contain 1744
 1115 modules between the barrel and two endcap sections.

1116 The innermost layer, the IBL, was added during the long shutdown before Run
 1117 2, and provides the fourth track measurement. It was inserted directly into the
 1118 existing pixel detector by removing the existing beam pipe and replacing it with
 1119 a significantly smaller version. This insertion can be seen in action in Figure 19,
 1120 which emphasizes the extreme precision required to place the the 70 cm long
 1121 layer with only 2 mm of clearance. The IBL was commissioned to provide con-
 1122 tinued tracking robustness and high precision in the higher luminosity environ-
 1123 ment of Run 2 [9]. The proximity of this layer to the collisions necessitated an
 1124 even higher granularity and better radiation hardness than the other pixel lay-
 1125 ers. And the strict space requirements to add an active sensing layer so close to
 1126 the interaction point required a sensor chip with a much higher active area and
 1127 a larger overall area per chip. These requirements led to the development of a

Parameter	Particle	Value
Reconstruction Efficiency	Muon, $p_T = 1 \text{ GeV}$	96.8%
	Pion, $p_T = 1 \text{ GeV}$	84.0%
	Electron, $p_T = 5 \text{ GeV}$	90.0%
Momentum Resolution	$p_T = 1 \text{ GeV}, \eta \approx 0$	1.3%
	$p_T = 1 \text{ GeV}, \eta \approx 2.5$	2.0%
	$p_T = 100 \text{ GeV}, \eta \approx 0$	3.8%
	$p_T = 100 \text{ GeV}, \eta \approx 2.5$	11%
Transverse IP Resolution	$p_T = 1 \text{ GeV}, \eta \approx 0$	$75 \mu\text{m}\%$
	$p_T = 1 \text{ GeV}, \eta \approx 2.5$	$200 \mu\text{m}$
	$p_T = 1000 \text{ GeV}, \eta \approx 0$	$11 \mu\text{m}$
	$p_T = 1000 \text{ GeV}, \eta \approx 2.5$	$11 \mu\text{m}$
Longitudinal IP Resolution	$p_T = 1 \text{ GeV}, \eta \approx 0$	$150 \mu\text{m}\%$
	$p_T = 1 \text{ GeV}, \eta \approx 2.5$	$900 \mu\text{m}$
	$p_T = 1000 \text{ GeV}, \eta \approx 0$	$90 \mu\text{m}$
	$p_T = 1000 \text{ GeV}, \eta \approx 2.5$	$190 \mu\text{m}$

Table 5: A summary of the expected performance of the combined inner detector [8]. Included are the reconstruction efficiencies for multiple particle types as well as the momentum and IP resolution for various momenta.

new chip type, the FE-I4 (compared to the FE-I3 chips used in the original pixel detector) with improved radiation hardness and a larger active footprint of 90%. The IBL is comprised of 448 of these individual chips arranged in 14 staves, with 26,880 pixels per chip and a chip size of 18.5 mm x 41.3 mm x 200 μm . The staves, like in the other layers of the pixel detector, are offset by 14° to provide full azimuthal coverage. This arrangement can be seen in Figure 20, which shows two computer-generated images of the IBL geometry and includes the some of the remaining pixel layers.

6.3.2 SEMICONDUCTOR TRACKER

The SCT, the subdetector which immediately surrounds the Pixel detector, provides additional discrete measurements of the trajectory of a charged particle. Because the SCT is further away from the interaction point, the spatial resolution does not need to be as high as in the pixel detector, and so the SCT uses micro-strips instead of pixels. Although pixels provide a more accurate measurement, the number of pixels and readout channels required to cover the cylindrical area at the radius of the SCT layers would be prohibitively complicated and expensive.

Each individual silicon strip sensor contains 768 individual readout strips with a total area of 6.36 cm x 6.40 cm and a pitch of 80 μm . Pairs of these sensors are then bonded together to form a combined strip with a length of 12.8 cm. Two of these combined strips are then placed back to back with a relative tilt

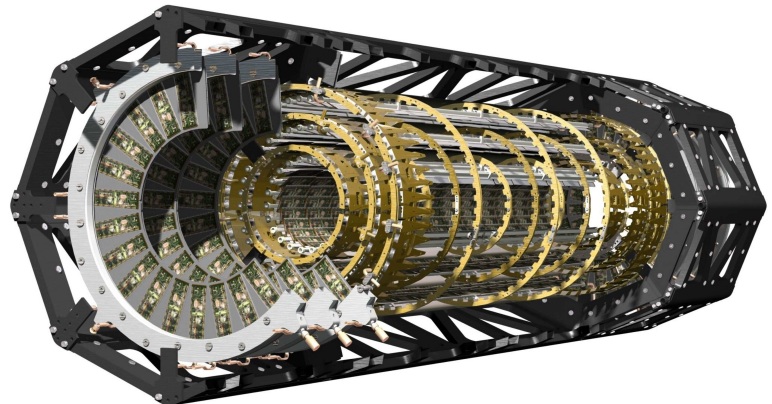


Figure 18

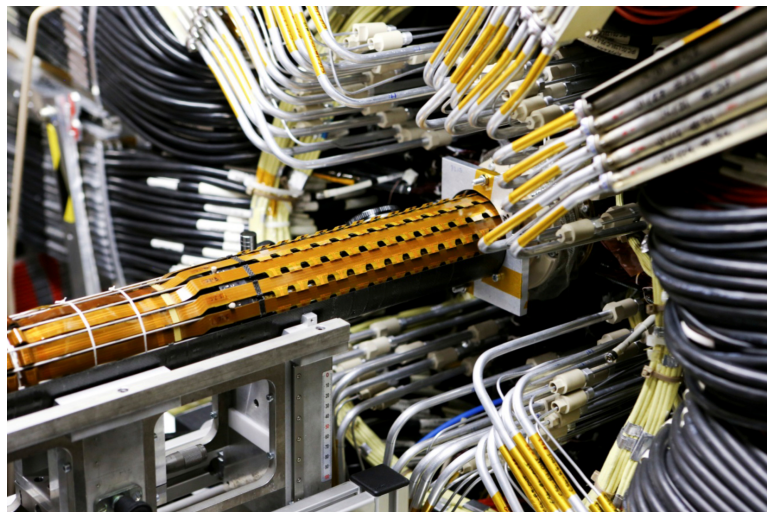


Figure 19: An image of the insertion of the [IBL](#) into the current pixel detector.

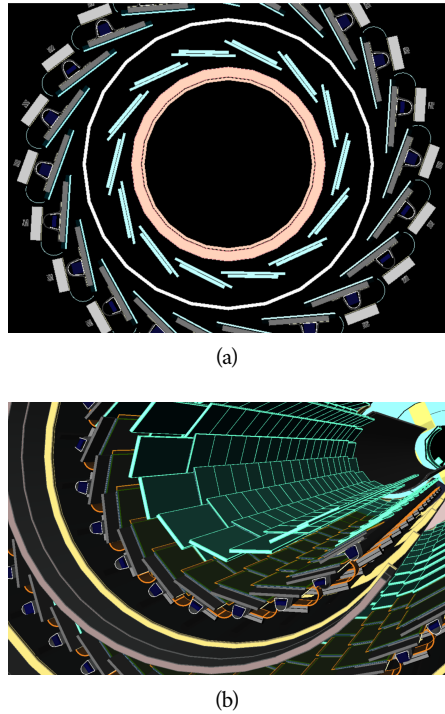


Figure 20: A three-dimensional computer-generated image of the geometry of the [IBL](#) with a view (a) mostly transverse to the beam pipe (b) mostly parallel to the beam pipe.

of 40 mrad. This geometry is illustrated in an exploded-out view in Figure 21. The purpose of angular offset of the consecutive layers is to allow the strip sensor areas to more accurately measure the position of a particle by comparing the overlap of the two strips which were traversed by a track.

Four of these double layers are placed in the barrel region, with radii of 284 mm, 355 mm, 427 mm, and 498 mm. Together these layers provide eight additional measurements for each track that traverses the central $|\eta|$ region. In the endcap region, the layers are arranged in wheels, with the double layers similarly offset to provide improved resolution. With these configurations, the [SCT](#) achieves a spatial resolution of $17 \mu\text{m}$ in the $r - \phi$ direction and $580 \mu\text{m}$ in the z direction.

6.3.3 TRANSITION RADIATION TRACKER

The final component of the inner detector, the [TRT](#), provides continuous tracking using straw drift tubes. The tubes are made of Kapton and aluminum with a diameter of 4 mm and are filled with a gas mixture of 70% Xe, 27% CO₂, and 3% O₂. At the center of each tube is a gold-plated anode tungsten wire $30 \mu\text{m}$ in diameter. When a charged particle passes through these tubes, it ionizes the gas within. The ions produced drift in the electric field established between the wire and the tube wall, and the large electric field near the wire produces avalanche multiplication and results in an electric current on the wire that is read out by the electronics and provides a track measurement. The time it takes the ioniza-

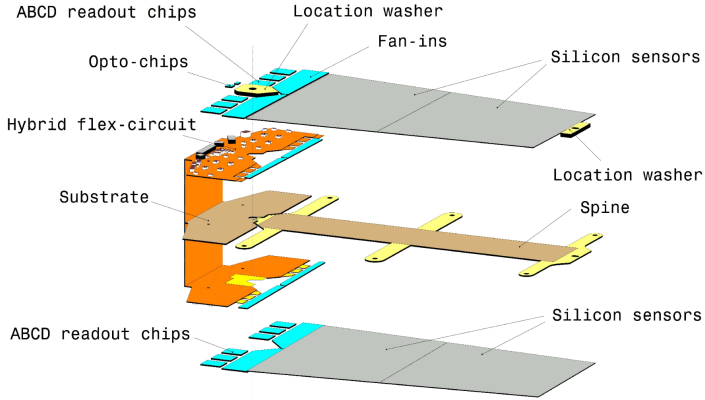


Figure 21: An exploded view of the geometry of the [SCT](#) double layers in the barrel region.

tion to drift to the wire can be used to estimate the distance from the wire that the particle passed through the tube; this gives a resolution on the distance of approximately $130\mu\text{m}$. Combining several such measurements between consecutive hits in the [TRT](#) tubes allows the trajectory of the particle to be reconstructed.

In addition to the continuous tracking, the detector can use transition radiation produced when a particle passes between the layers to distinguish between electrons and heavier charged particles. The space between the tubes is filled with CO_2 , and so has a different dielectric constant than the gas within the tubes which contains Xe. At the transition between those media, a relativistic particle emits radiation proportional to γ , so inversely proportional to mass at a fixed momentum. The photons produced in this transition then produces an ionization cascade which is significantly larger than the signal for the minimally-ionizing charged particles. To distinguish between these two cases, the [TRT](#) defines two signal thresholds, a low threshold for the typical signal produced by a minimally ionizing particle ([MIP](#)) and a high threshold for the the signal produced by transition radiation. A high momentum electron is expected to produce approximately 7 to 10 high threshold hits as it traverses the [TRT](#), and thus these hits provide a way to distinguish electrons from other charged particles.

The [TRT](#) contains 351,000 tubes in total, divided between the barrel and endcap regions. In the barrel region, the tubes are 144 cm long and arranged in 73 layers parallel to the beampipe. In the endcap region, the tubes are 37 cm long and arranged in 160 layers transverse to the beampipe. These configurations can be seen in Figure 15 and Figure 16. With this geometry the [TRT](#) achieves a resolution of $130\mu\text{m}$ in the $r - \phi$ direction.

6.4 CALORIMETRY

The combination of calorimeter systems used in [ATLAS](#) can measure the energy of electrons, photons, hadrons, and hadronic jets with complete coverage up to $|\eta| < 4.9$ and across ϕ . Unlike the inner detector, the calorimeters are capable of measuring neutral particles. To accomplish precision measurements of these

1198 particle types, the [ATLAS](#) calorimeter system uses four individual calorimeters,
 1199 a [LAr](#) electromagnetic calorimeter in the barrel region, a tile hadronic calorime-
 1200 ter in the barrel region, a [LAr](#) hadronic endcap calorimeter, and a [LAr](#) forward
 1201 calorimeter. Together these provide hermetic coverage for the [ATLAS](#) detector.
 1202 The configuration of these calorimeters is illustrated in Figure 22. **Note: I could**
 1203 **make this section much longer. It might be nice to include a more com-**
 1204 **plete description of showers for example. I will extend this section if their**
 1205 **is space at the end.**

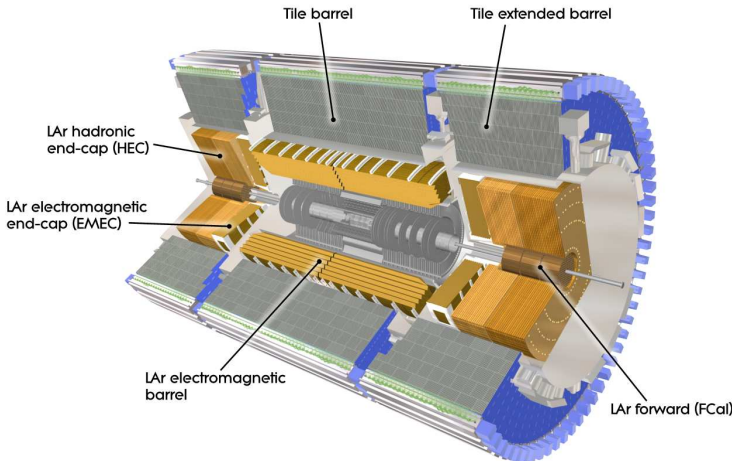


Figure 22

1206 The calorimeters are designed to absorb and measure the energy carried by
 1207 a particle, and completely stop the particle's propagation in the process. This
 1208 requires a significant amount of material to provide interactions. These interac-
 1209 tions then produce secondary particles, which can produce secondary particles
 1210 in turn, and thus form a cascade of particles called an electromagnetic ([EM](#)) or
 1211 hadronic shower, depending on the governing mechanism. Electromagnetic and
 1212 hadronic showers have very different properties and require different technolo-
 1213 gies to measure them accurately. All of the calorimeters in the [ATLAS](#) calorimeter
 1214 system are sampling calorimeters, that is they use alternating layers of absorbing
 1215 and active material. The dense absorbing layers initiate the showers while the ac-
 1216 tive layers measure the energy of the produced particles. A fraction of the energy
 1217 is lost in the inactive layers, so the energy measurement from the active layers
 1218 has to be corrected to estimate the actual energy of the particle.

1219 The [EM](#) calorimeter provides around 20 radiation lengths (X_0) while the hadronic
 1220 calorimeter provides around 10 interaction lengths (λ_0). As mentioned previ-
 1221 ously, radiation lengths measure the distance over which an electromagnetically
 1222 interacting particle loses a characteristic fraction of its energy. Interaction lengths,
 1223 on the other hand, measure the mean distance traveled by a hadronic particle be-
 1224 fore undergoing a nuclear interaction [7]. Figure 23 show the radiation lengths
 1225 in the layers of the [EM](#) calorimeter in the barrel region as well as the interaction
 1226 lengths for all calorimeters.

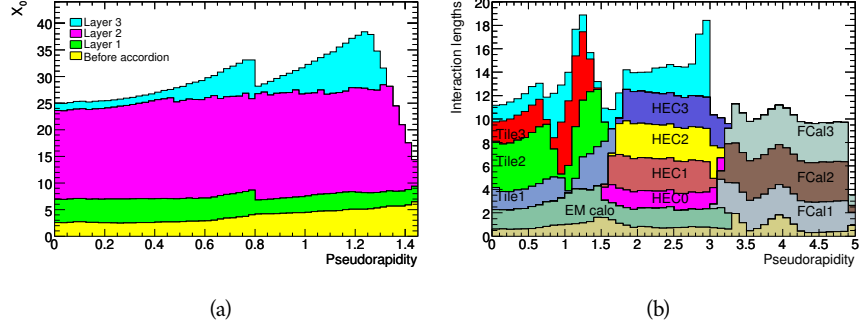


Figure 23: The depth of (a) the electromagnetic barrel calorimeter in radiation lengths and (b) all calorimeters in interaction lengths as a function of pseudorapidity.

1227 6.4.1 ELECTROMAGNETIC CALORIMETER

1228 The electromagnetic calorimeters use alternating layers of Liquid Argon
 1229 and lead in an accordion shape. The accordion shape allows a construction that pro-
 1230 vides complete coverage in the ϕ direction while also providing many alterna-
 1231 ting layers for the a particle to pass through. The configuration is detailed in
 1232 Figure 24. When an electron or photon passes through the lead, it produces an
 1233 electromagnetic shower. The particles produced in those showers then pass into
 1234 and ionize the Liquid Argon; the ions produced can then be collected by an elec-
 1235 trode in the Liquid Argon layer to provide the actual energy measurement.

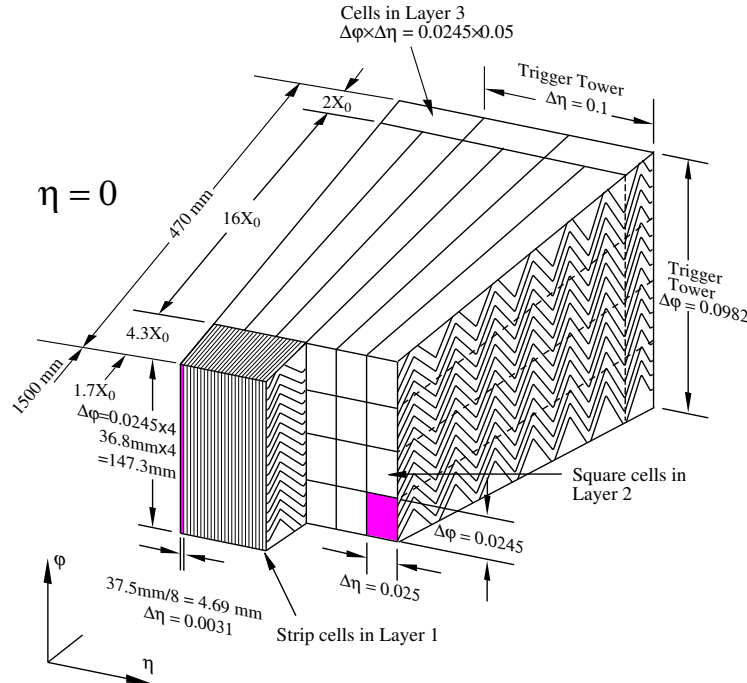


Figure 24: A schematic of the [LAr](#) calorimeter in the barrel region, highlighting the accordian structure.

The barrel region is covered by a presampler and three separate sampling layers with decreasing segmentation. The presampler is just a thin layer of Liquid Argon which measures the energy of any electromagnetic showers which are initiated before the particle reaches the calorimeter due to interactions with the detector material. The first layer is the strip layer, which has fine segmentation in η to enhance the identification of shower shapes and to provide a precise η measurement for reconstructing photons and electrons. The strip layer has only 4 radiation lengths worth of material, and has a segmentation of $\Delta\eta = 0.003$ and $\Delta\phi = 0.1$. The second layer is also finely segmented, with a segmentation of $\Delta\eta = 0.025$ and $\Delta\phi = 0.025$, and a thickness of $16 X_0$. This layer is designed to contain an electromagnetic shower and to measure the majority of the energy for photons and electrons. The third layer is only $2 X_0$ thick and measures the energy of electromagnetic showers which leak out of the second layer, and helps to separate electromagnetic showers from hadronic showers. The structure of the LAr endcap calorimeter is similar except that the layers are arranged parallel to the beampipe to measure energy deposits from high η particles.

6.4.2 HADRONIC CALORIMETERS

The hadronic calorimeters use a few different technologies to satisfy the resolution demands in the different areas of the detector, and together they cover the region $|\eta| < 2.7$. In the barrel region, for $|\eta| < 1.7$, the hadronic calorimeters are constructed of alternating tiles of steel and plastic scintillator. Like in the electromagnetic calorimeter, the dense layer initiates a shower (in this case the dense layer is the steel and the shower is hadronic) of particles which pass into and ionize the following layer. The ionization in the plastic scintillator instead produces a light signal proportional to the amount of ionization produced by the shower, and this signal is measured using photomultipliers and provides the actual energy measurement. The construction of a tile in the calorimeter is shown Figure 25, which highlights the alternating layers of steel and scintillator.

This tile calorimeter, as well as the remaining hadronic calorimeters, have a much coarser granularity than the electromagnetic calorimeters. The high granularity is not needed for an accurate energy measurement, and the hadronic calorimeters are not designed to distinguish particle types like the electromagnetic calorimeters. The tile granularity is approximately $\Delta\eta = 0.1$ and $\Delta\phi = 0.1$, and the segmentation in depth and η is shown in Figure 26.

The remaining hadronic calorimeters all use the same alternating, sampling structure but with different active and inactive materials. The hadronic endcap calorimeter covers the range of $1.5 < |\eta| < 3.2$ and uses an inactive layer of copper and an active layer of Liquid Argon. The forward calorimeter covers the range of $3.1 < |\eta| < 4.9$ and uses a dense matrix of copper and tungsten filled with Liquid Argon.

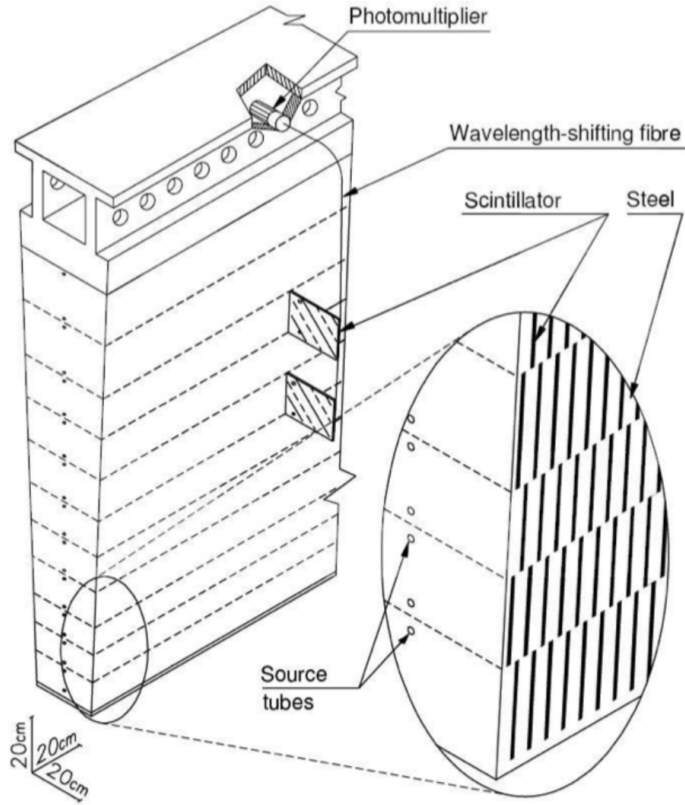


Figure 25: A schematic of a hadronic tile module which shows the alternating layers of steel and plastic scintillator.

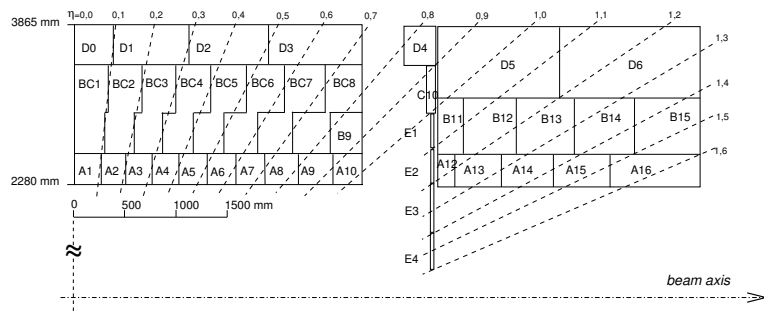


Figure 26: The segmentation in depth and η of the tile-calorimeter modules in the central (left) and extended (right) barrels.

1276 6.5 MUON SPECTROMETER

1277 Among SM particles, only muons and neutrinos consistently pass through the
 1278 calorimeters. Because the neutrinos are also electrically neutral, there is no fea-
 1279 sible option to measure them directly in ATLAS. The muons, on the other hand,
 1280 are charged and are thus already measured as a track in the inner detector. The
 1281 muon spectrometer provides a way to consistently identify muon tracks and also
 1282 a way to provide an additional measurement of their momentum.

1283 The muon spectrometer contains four subdetectors that cover the barrel and
 1284 endcap regions. In the barrel region, the muon spectrometer uses a combination
 1285 of Resistive Plate Chambers (RPCs) and MDTs to provide both a coarse, fast mea-
 1286 surement for triggering and a precise momentum measurement for offline event
 1287 reconstruction. Similarly, in the endcap region, the TGCs, MDTs, and CSCs allow
 1288 for both triggering and precise measurements. The CSCs are used only in the in-
 1289 nermost layer of the endcap region between $2.0 < |\eta| < 2.7$ where the particle
 1290 flux is too large for the MDTs to provide accurate measurements. The overall
 1291 layout of the muon systems are shown in the cut-away diagram in Figure 27,
 1292 and Figure 28 shows a precise schematic of the layout of each of the detecting
 1293 elements. The geometric arrangement shown provides consistent coverage for
 1294 muons produced up to $|\eta| < 2.7$, and takes full advantage of the bending of the
 1295 muons in the toroidal magnetic field, described in Section 6.2, to measure their
 1296 momentum. Figure 29 shows a cross-section of the arrangement of the muon
 1297 spectrometer in the barrel; the layers are divided into eight small and eight large
 1298 chambers that are overlapped to provide complete coverage in ϕ .

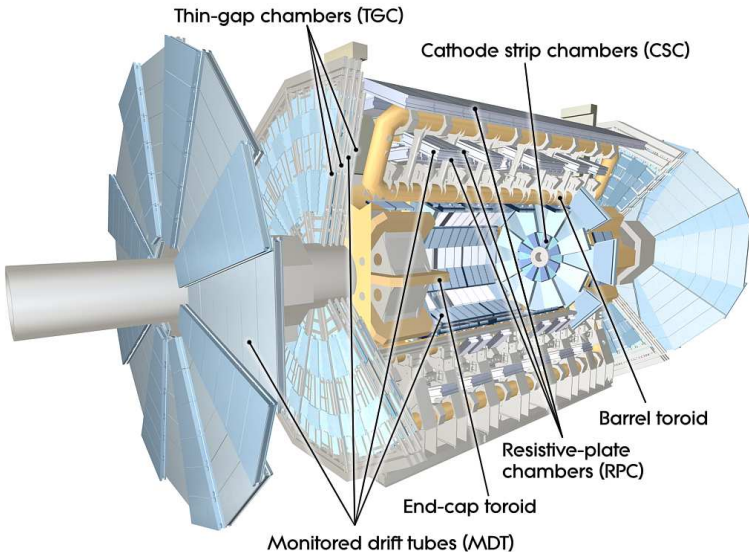


Figure 27: A cut-away diagram of the muon systems on ATLAS.

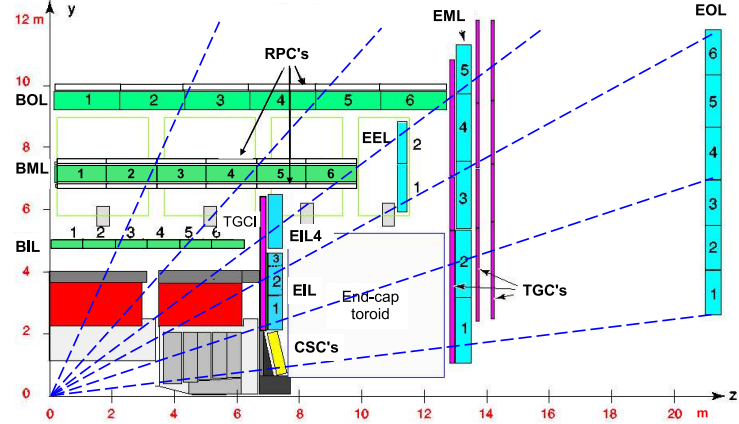


Figure 28: A quarter view of the muon spectrometer which highlights the layout of each of the detecting elements. The BOL, BML, BIL, EOL, EML, and EIL are all MDT elements, where the acronyms encode their positions.

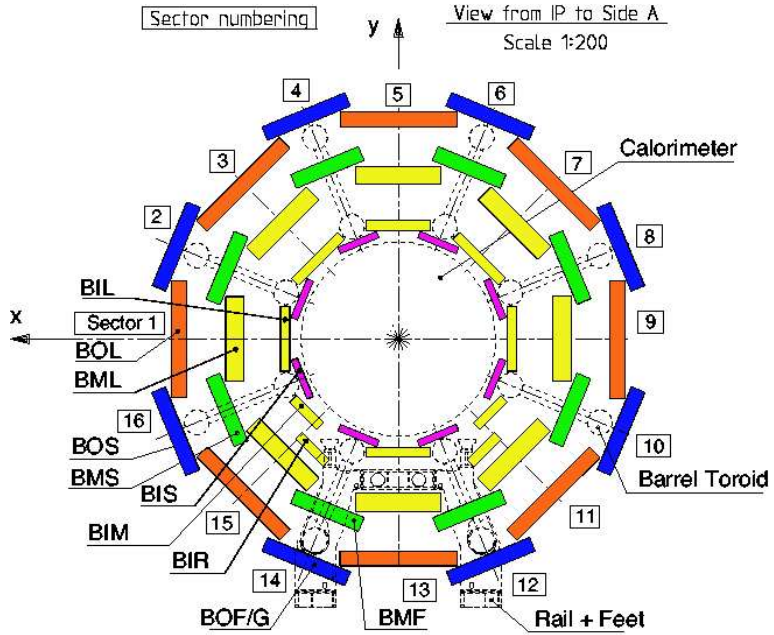


Figure 29: A schematic of the cross-section of the muon spectrometer in the barrel region.

1299 6.5.1 MONITORED DRIFT TUBE

1300 The momentum measurements in the barrel region are provided by three con-
 1301 secutive layers of MDT elements, located at approximately 5 m, 7 m, and 9 m from
 1302 the interaction point. Each of these layers is a composite of two multilayers of
 1303 drift tubes: two layers of three to four layers of tubes, as shown in Figure 30.
 1304 These aluminum tubes are 3 cm in diameter, with lengths between 0.9 and 6.2 m,
 1305 and are filled with a mixture of ArCO₂ kept at 3 bar absolute pressure. A central
 1306 tungsten-rhenium wire with a diameter of 50 μm runs along the length of the
 1307 tube, and is kept at a potential of 3080 V.

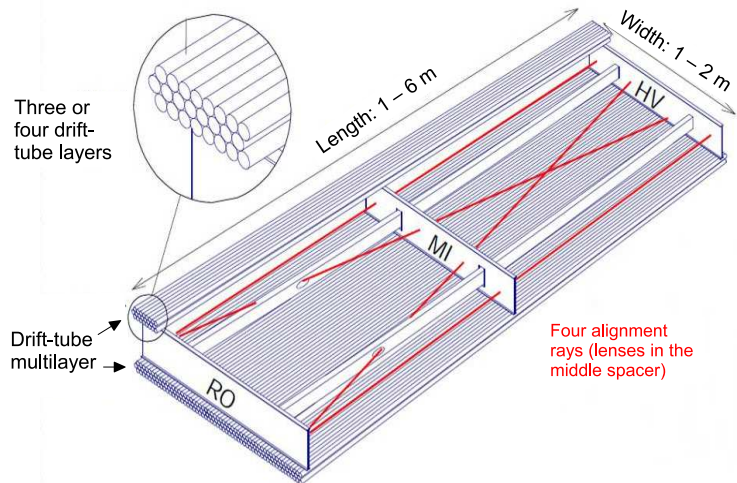


Figure 30: A schematic of a single MDT chamber, which shows the multilayers of drift tubes as well as the alignment system.

1308 A muon traversing these tubes ionizes the gas, and the ionization electrons
 1309 then drift in the electric field toward the central wire. Close to the wire, the
 1310 electric field is strong enough to cause the original ionization electrons to ion-
 1311 ize additional electrons, producing an avalanche that can be measured as a cur-
 1312 rent along the wire. The time of arrival of that current depends on how far the
 1313 muon entered from the wire, and can be used to achieve a position resolution of
 1314 80 μm in an individual tube. The combination of the measurements in the con-
 1315 secutive layers of tubes improves this position resolution to 35 μm .

1316 To achieve a good resolution over the entire length of a muon track, the rel-
 1317 ative positions of the tubes of the muon spectrometer must be known to an ac-
 1318 curacy of 30 μm . This is achieved by an optical laser alignment system placed in
 1319 each of the individual chambers and throughout the cavern. These monitor any
 1320 changes in position or alignment due to effects like gravitational sag, tempera-
 1321 ture shifts, and the magnetic field. The configuration of the alignment system
 1322 within an individual chamber is also shown in Figure 29.

1323 6.5.2 RESISTIVE PLATE CHAMBER

1324 The **RPC** is the outermost detecting layer in the muon spectrometer in the barrel
 1325 region, and provides a fast measurement of the ϕ position of muons for trig-
 1326 gering. The speed of the measurement, with a time resolution of just a few
 1327 nanoseconds, requires a poor spatial resolution of approximately 1 cm. There
 1328 are three **RPCs** layers in the muon spectrometer, two located on either side of
 1329 the central **MDT** layer and one located outside the final **MDT** layer, as shown in
 1330 Figure 28. The **RPCs** consist of two layers of parallel plates filled with a gas mix-
 1331 ture of $C_2H_2F_4$. A muon passing through these systems ionizes the gas, like in
 1332 the **MDT**, which causes an avalanche of ionization electrons in the electric field
 1333 maintained between the plates. Metal strips on the outside of the chamber ca-
 1334 pacitively couple to the accumulated charge, and are read out to measure the η
 1335 and ϕ positions of the muon track.

1336 6.5.3 CATHODE STRIP CHAMBER

1337 The majority of the momentum measurements in the endcap region are provided
 1338 by the **MDTs**. In the most forward region of the muon spectrometer, between
 1339 $2.0 < \eta < 2.7$, the particle flux is very high due to contributions from low energy
 1340 photons and neutrons. The **MDT** can only sustain a hit rate of approximately 150
 1341 Hz/cm² because of limitations in the drift times of the gas and the capacity of
 1342 the readout electronics. The **CSCs** were designed to handle higher hit rates, up to
 1343 1000 Hz/cm², and provide the necessary coverage in that high flux region.

1344 The **CSC** consists of several multiwire proportional chambers, where the wires
 1345 are oriented in the radial direction out from the beampipe. There are eight large
 1346 and eight small chambers, arranged to partially overlap in the ϕ direction, as
 1347 shown in Figure 31. Like in the **MDT**, a muon traversing the system produces
 1348 ionization in the gas; here, however, the ionization is collected on a number of
 1349 wires. These wires couple to cathodes on the chambers which are segmented
 1350 into strips in two directions. The relative amount of charge on each of the neigh-
 1351 boring strips can be used to interpolate to the position of the muon in both η
 1352 and ϕ .

1353 6.5.4 THIN GAP CHAMBER

1354 Like in the barrel region, a separate, fast detector is required to provide position
 1355 measurements of muons for trigger in the endcap region. This is provided by
 1356 the **TGC** which consists of seven layers in the middle station of the endcap, two
 1357 doublet layers and one triplet layer, and a single doublet layer in the inner endcap
 1358 station. Figure 32 shows the arrangement of the triple and doublet layers of the
 1359 **TGCs**.

1360 Like the **CSCs**, the **TGCs** are multiwire proportional chambers with a wire-to-
 1361 cathode distance of 1.4 mm and a wire-to-wire distance of 1.8 mm. Readout
 1362 strips on the outside of the chambers run perpendicular to the wires, and couple
 1363 to the charge collected on the wires to provide a position measurement in the η

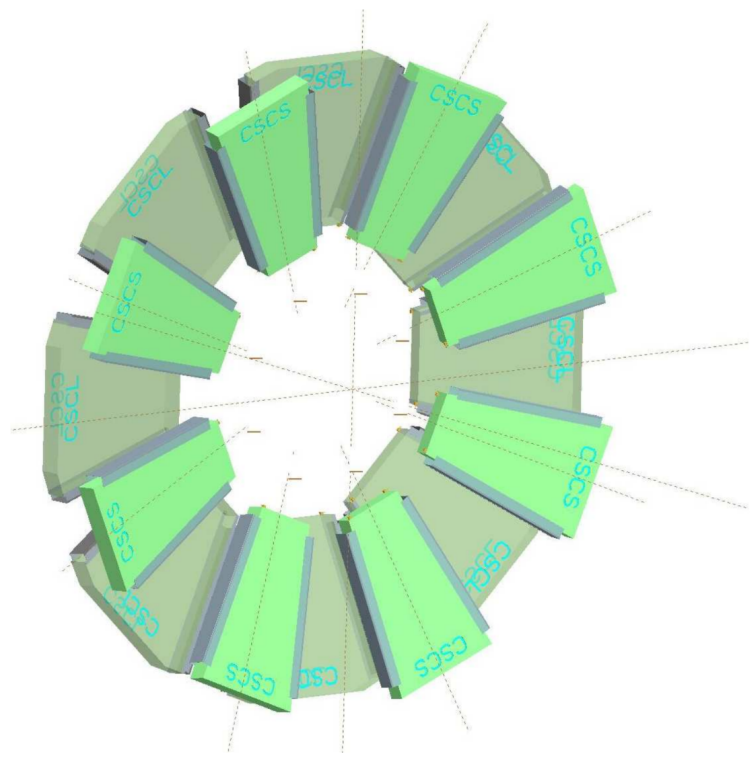


Figure 31: A schematic of the **CSC** endcap, showing the overlapping arrangement of the eight large and eight small chambers.

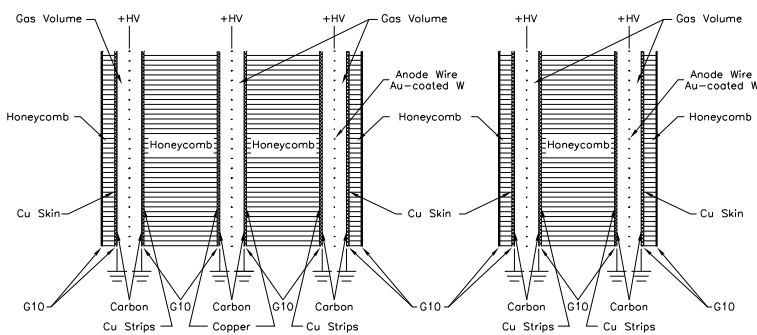


Figure 32: A schematic of the **TGC** doublet and triplet layers.

1364 direction. The current induced on the wires is also readout to provide a position
 1365 measurement in the ϕ direction. The high electric field and small wire-to-wire
 1366 distance give it the required good time resolution to be used for triggering events.

1367 6.6 TRIGGER

1368 It is not possible for the detector and the associated computing systems to record
 1369 the terabytes of data that the 40 MHz of proton-proton collisions produce every
 1370 second. Instead, a small fraction of these events are selected by the trigger sys-
 1371 tem to be recorded and later analyzed. Selecting interesting events at such a high
 1372 rate poses a significant challenge for the both the detector design and the imple-
 1373 mentation of a trigger decision and data acquisition system. The trigger must
 1374 balance the time needed to decide to keep an event, to avoid losing information,
 1375 with the filtering accuracy to consistently select a full menu of physics events
 1376 that can be used for the wide array of searches and measurements targeted by
 1377 [ATLAS](#).

1378 The [ATLAS](#) trigger system, as of Run 2, consists of two levels of decision mak-
 1379 ing. The first level, referred to as L1, is hardware based and uses inputs from
 1380 a subset of the detector elements to narrow the considered event rate from the
 1381 original 40 MHz down to 100 kHz. The 100 kHz rate is the maximal rate that
 1382 the event information can be transferred from the detector. The second level,
 1383 referred to as the [HLT](#), makes the final decisions on which events to keep for
 1384 analysis and selects a rate of around 1 kHz. The collection of selection criteria
 1385 used to make the L1 decisions feed into subsequent selection criteria in the [HLT](#),
 1386 and the set of these combinations of L1 and [HLT](#) criteria from the trigger menu
 1387 which defines exactly what events are recorded on [ATLAS](#). The entirety of the
 1388 trigger menu used for 2015 data collection is shown in Table 6, which summa-
 1389 rizes the selection requirements at both levels and additionally shows the peak
 1390 measured rates contributed by each.

1391 At L1, the trigger system uses information primarily from the calorimeters
 1392 and muon spectrometer to select high p_T jets, electrons, photons, and muons.
 1393 The electromagnetic calorimeter uses reduced granularity energy measurements
 1394 as well as isolation requirements to select electrons and photons. The hadronic
 1395 calorimeter also uses a combination of reduced granularity energy measurements
 1396 and isolation to select high momentum jets and hadronically decaying tau lept-
 1397 ons. The calorimeters are also used to provide triggers based on missing energy:
 1398 the coarse granularity energy measurements are used to calculate a directional
 1399 sum of energies and to trigger on a significant imbalance. Only the [RPCs](#) and [TGCs](#)
 1400 muon subdetectors contribute to the decision at L1, and are used to identify high
 1401 momentum muons. The contributions to the triggering rate of the various types
 1402 of L1 triggers are shown in Figure 33. The total rate is indicated in black and
 1403 is lower than the sum of individual rates because their is significant overlap be-
 1404 between different trigger channels. The majority of the rate comes from lepton
 1405 and photon triggers.

1406 After an event is chosen by the L1 trigger, the detector measurements from the
 1407 bunch crossing which fired the trigger is read out from the front-end electronics

Trigger	Typical offline selection	Trigger Selection		Level-1 Peak Rate (kHz)	HLT Peak Rate (Hz)
		Level-1 (GeV)	HLT (GeV)	$L = 5 \times 10^{33} \text{ cm}^{-2}\text{s}^{-1}$	
Single leptons	Single iso μ , $p_T > 21$ GeV	15	20	7	130
	Single e , $p_T > 25$ GeV	20	24	18	139
	Single μ , $p_T > 42$ GeV	20	40	5	33
	Single τ , $p_T > 90$ GeV	60	80	2	41
Two leptons	Two μ 's, each $p_T > 11$ GeV	2×10	2×10	0.8	19
	Two μ 's, $p_T > 19, 10$ GeV	15	18, 8	7	18
	Two loose e 's, each $p_T > 15$ GeV	2×10	2×12	10	5
	One e & one μ , $p_T > 10, 26$ GeV	$20 (\mu)$	7, 24	5	1
	One loose e & one μ , $p_T > 19, 15$ GeV	15, 10	17, 14	0.4	2
	Two τ 's, $p_T > 40, 30$ GeV	20, 12	35, 25	2	22
	One τ , one μ , $p_T > 30, 15$ GeV	12, 10 (+jets)	25, 14	0.5	10
	One τ , one e , $p_T > 30, 19$ GeV	12, 15 (+jets)	25, 17	1	3.9
Three leptons	Three loose e 's, $p_T > 19, 11, 11$ GeV	15, 2 \times 7	17, 2 \times 9	3	< 0.1
	Three μ 's, each $p_T > 8$ GeV	3 \times 6	3 \times 6	< 0.1	4
	Three μ 's, $p_T > 19, 2 \times 6$ GeV	15	18, 2 \times 4	7	2
	Two μ 's & one e , $p_T > 2 \times 11, 14$ GeV	$2 \times 10 (\mu's)$	$2 \times 10, 12$	0.8	0.2
	Two loose e 's & one μ , $p_T > 2 \times 11, 11$ GeV	2 \times 8, 10	2 \times 12, 10	0.3	< 0.1
One photon	one γ , $p_T > 125$ GeV	22	120	8	20
Two photons	Two loose γ 's, $p_T > 40, 30$ GeV	2×15	35, 25	1.5	12
	Two tight γ 's, $p_T > 25, 25$ GeV	2×15	2×20	1.5	7
Single jet	Jet ($R = 0.4$), $p_T > 400$ GeV	100	360	0.9	18
	Jet ($R = 1.0$), $p_T > 400$ GeV	100	360	0.9	23
E_T^{miss}	$E_T^{\text{miss}} > 180$ GeV	50	70	0.7	55
Multi-jets	Four jets, each $p_T > 95$ GeV	3×40	4×85	0.3	20
	Five jets, each $p_T > 70$ GeV	4×20	5×60	0.4	15
	Six jets, each $p_T > 55$ GeV	4×15	6×45	1.0	12
b -jets	One loose b , $p_T > 235$ GeV	100	225	0.9	35
	Two medium b 's, $p_T > 160, 60$ GeV	100	150, 50	0.9	9
	One b & three jets, each $p_T > 75$ GeV	3×25	4×65	0.9	11
	Two b & two jets, each $p_T > 45$ GeV	3×25	4×35	0.9	9
b -physics	Two μ 's, $p_T > 6, 4$ GeV plus dedicated b -physics selections	6, 4	6, 4	8	52
Total				70	1400

Table 6: The trigger menu for the 2015 data collection with $L = 5 \times 10^{33} \text{ cm}^{-2}\text{s}^{-1}$. Both the L1 and HLT selection requirements and their trigger rates are shown measured at the specified luminosity are shown. The typical offline selections represent a typical set of offline requirements imposed after the trigger in an analysis.

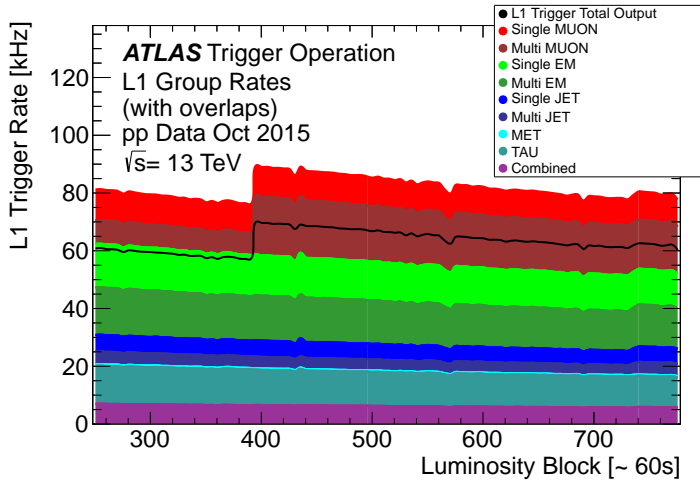


Figure 33: The L1 Trigger rate broken down into the types of triggers as a function of the luminosity block for the 2015 data collection period.

1408 and stored on read-out boards. This inclusive information is necessary to make
 1409 more the more precise event selections than is possible with the reduced infor-
 1410 mation at L1. The **HLT** then uses this information with software algorithms to
 1411 decide whether or not to permanently record the event. The L1 trigger also for-
 1412 wards which decision was made and Region of Interests (**RoIs**) to the **HLT**, which
 1413 allows the **HLT** to focus on particular algorithms and particular sections of the
 1414 detector to greatly improve the algorithmic selection speed. The additional in-
 1415 formation available to the **HLT** allows it to implement additional trigger targets,
 1416 such as identified jets from the decays of b-hadrons. The contributions to the
 1417 triggering rate of the various types of **HLT** triggers are shown in Figure 34.

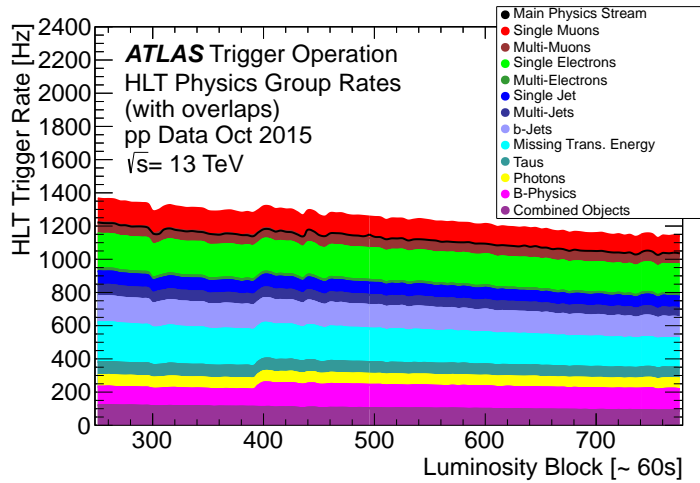


Figure 34: The HLT Trigger rate broken down into the types of triggers as a function of the luminosity block for the 2015 data collection period.

1418

1419 EVENT RECONSTRUCTION

1420 The ATLAS experiment combines measurements in the subdetectors to form a
 1421 cohesive picture of each physics event. The majority of particles that traverse
 1422 the detector leave behind some combination of ionization hits in the tracking
 1423 detectors or energy deposits in the calorimeters, and these measurements can
 1424 be used to reconstruct physical quantities like the particle's energy, momentum,
 1425 or trajectory. Even the type of the particle can be distinguished by comparing
 1426 the various ways that different species of stable particles interact with the subde-
 1427 tectors. Reconstruction is the process which takes the electronic outputs of the
 1428 detector and collects them into individual physics objects. The physics objects
 1429 summarize the properties of particles produced by the collision or subsequent
 1430 decays, either for individual isolated particles like leptons, or for a collection of
 1431 the cascade of products produced in the decay of an energetic hadron, called a
 1432 jet. These are the objects and quantities most often used in analysis to make
 1433 measurements of SM processes or to search for new physics.

1434 7.1 TRACKS AND VERTICES

1435 As described in Section 6.3, charged particles that traverse the inner detector
 1436 leave behind hits in the subdetectors. Each of these hits translates into a position
 1437 measurement along the trajectory of that particle, with position resolutions de-
 1438 pending on the subdetector that provided the measurement. Track reconstruc-
 1439 tion uses these position measurements to cluster hits in consecutive layers of
 1440 the detector into a trajectory consistent with a particle curving in a magnetic
 1441 field [10, 11]. The number of hits in the inner detector for each event makes
 1442 a combinatorial method completely infeasible: the algorithms that form tracks
 1443 must be significantly more intelligent so that event reconstruction does not ex-
 1444 haust computing resources.

1445 The first and primary algorithm employed in track reconstruction is called
 1446 the inside-out method, which begins with the assumption that the track orig-
 1447 inated from the interaction point. Its purpose is to identify primary particles,
 1448 those which originate in the proton-proton collisions and with a lifetime long
 1449 enough to reach the inner detector. Combinations of three space points are con-
 1450 sidered from measurements in the Pixel detector and the first layer of the SCT,
 1451 and form the seed for a track. The seed is then extrapolated into the SCT and
 1452 hits in each layer are considered to be added to the track using a combinatorial
 1453 Kalman filter [11]. After all of the SCT layers have been considered, tracks are
 1454 filtered to reduce ambiguities from other nearby tracks or from combinatorial
 1455 coincidences. Then the tracks are extended into the TRT in the same way. This
 1456 algorithm is how the hits are chosen to be incorporated into a single trajectory,

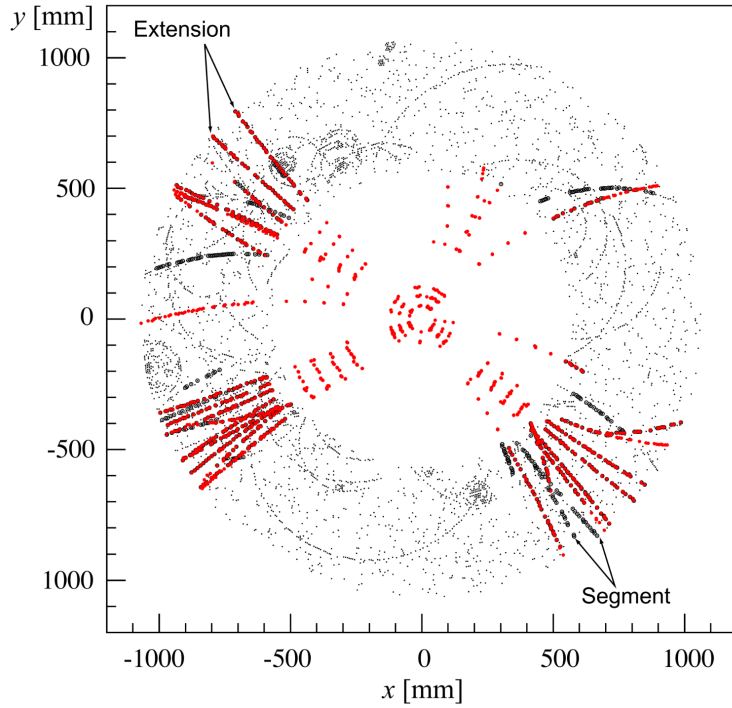


Figure 35: The x and y locations of the hits generated in a simulated $t\bar{t}$ event in the inner detector. The hits which belong to tracks formed using the inside-out algorithm are highlighted in red, while the hits which belong to tracks formed using the outside-in algorithm are circled in black.

1457 and then those hits are used together to form a best-fit trajectory which gives the
 1458 direction and momentum of the track.

1459 This inside-out algorithm is complemented by an outside-in algorithm, which
 1460 is used to find tracks from secondary particles, those produced in the decays
 1461 or interactions of the primary particles inside the detector. As the name indicates,
 1462 the outside-in algorithm begins by seeding tracks in the outermost layers
 1463 of the inner detector, in the [TRT](#). The seed in this case is formed by a segment
 1464 in the [TRT](#), and the track is propagated backwards into the [SCT](#) before being re-
 1465 fitted to use all the included points. Some tracks are found with [TRT](#) segments
 1466 only, which can result from interactions with the detector following the [SCT](#). Fig-
 1467 ure 35 shows an example of the geometry of tracks formed by both algorithms,
 1468 where the hits belonging to tracks found using the inside-out algorithm are high-
 1469 lighted in red, and the hits belonging to the tracks found using the outside-in
 1470 algorithm are circled in black. The figure highlights the presence of a large num-
 1471 ber of both primary and secondary tracks in a single event, as well as the overall
 1472 large number of hits present in the inner detector.

1473 The tracks resulting from these algorithms can be contaminated by nearby
 1474 particles confusing the tracking algorithm in a high luminosity environment.
 1475 For example, enough hits present in the inner detector can lead to fake tracks
 1476 from combinations of hits from multiple individual tracks. Therefore, after the
 1477 tracks are formed and fitted, additional quality requirements are imposed in
 order to reduce such backgrounds. Most tracking applications require at least

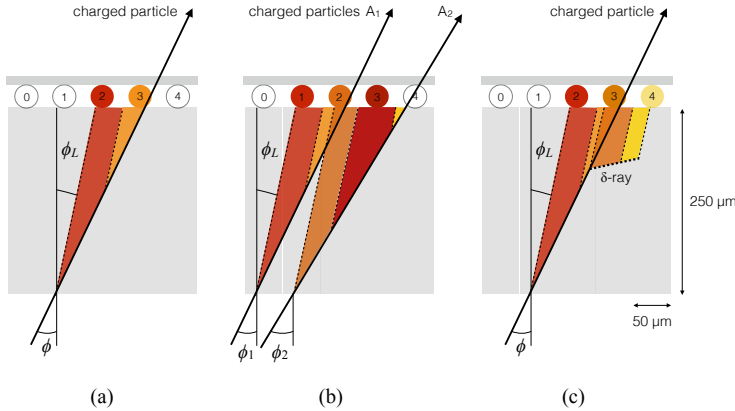


Figure 36: Examples of the clusters formed in a single layer of the pixel detector for (a) a single isolated particle, (b) two nearly-overlapping particles, and (c) a particle which emits a δ -ray [12].

1479 seven silicon hits, seven hits between the Pixel detector and **SCT**. Then the tracks
 1480 are required to have at most two holes in the Pixel detector, where holes are non-
 1481 existing but expected measurements in a layer of the subdetector. If the missing
 1482 hit corresponds to an inactive module, however, it is not counted as a hole but
 1483 instead as a hit for tracking as the lack of a measurement is expected in that case.

1484 7.1.1 PIXEL NEURAL NETWORK

1485 The hits in the Pixel detector are not typically confined to a single pixel, but
 1486 rather the charge is spread over several pixels per layer which are grouped to-
 1487 gether into clusters. The clustering of these pixels for isolated tracks is relatively
 1488 straightforward, but complications can arise in the high track density environ-
 1489 ment where hits from multiple particles can overlap in a single cluster. Figure 36
 1490 shows examples of clusters generated by a single isolated particle, two nearly
 1491 overlapping particles, and a particle which emits a δ -ray. A δ -ray is a secondary
 1492 electron which is generated with enough energy to escape a significant distance
 1493 away from the original particle and to generate additional ionization.

1494 A series of neural-networks analyzes the shape of the clusters to determine
 1495 how many particles produced the cluster and to find the positions of each of the
 1496 particles within the cluster. These allow for an identification of clusters caused
 1497 by more than one particle or by a particle that emits a δ -ray. In a high-density
 1498 tracking environment, the multiple position outputs can be used as the locations
 1499 of individual hits to allow reconstruction of tracks which almost overlap and
 1500 with a much better separation than is possible without the splitting of individual
 1501 clusters.

1502 7.1.2 PIXEL DE/DX

1503 A hit in the Pixel detector is determined by the voltage generated from ioniza-
 1504 tion current rising above a threshold value that is tuned to consistently record
 1505 the passing of a **MIPs**. A larger amount of charge deposited results in a larger volt-
 1506 age, and a larger signal remains above the threshold for a longer period of time.
 1507 The time over threshold (**ToT**) is read out of the Pixel detector, and is calibrated to
 1508 provide a measurement of the charge deposited in each pixel. The charge mea-
 1509 surements from each of the pixels included in a pixel cluster are combined to
 1510 form one charge measurement per layer of the pixel detector. That charge mea-
 1511 surement, combined with the angle of incidence of the track and the known sizes
 1512 of each detector element, can be converted into a measurement of dE/dx , the
 1513 ionization energy deposited per unit distance, measured in $\text{MeVg}^{-1}\text{cm}^2$. The
 1514 **IBL** only has sixteen (4 bits) available values of **ToT** to readout, compared to the
 1515 256 (8 bits) available values in the remaining pixel layers, so in addition to report-
 1516 ing the value the **IBL** also records if the ionization is large enough to be above its
 1517 range of values, called overflow.

1518 The measurements across multiple layers are combined to form an average
 1519 value of dE/dx for the track as a whole. To reduce the influence of the typical
 1520 long Landau tails of the distribution of dE/dx deposits [7], the average is calcu-
 1521 lated as a truncated mean. The value measured in the **IBL** is removed if it is in
 1522 overflow, as the value measured in that case is not reliable. If a track has five
 1523 measurements in the pixel detector, the two highest cluster values are removed
 1524 If a track has two, three, or four measurements in the pixel detector, only the
 1525 single highest cluster value is removed. The remaining values are averaged to
 1526 form the pixel dE/dx .

1527 7.1.3 VERTEX RECONSTRUCTION

1528 A vertex represents the intersection of multiple tracks and corresponds to the
 1529 location of an interaction between particles which resulted in either the produc-
 1530 tion or deflection of charged particles which are then measured in the detector.
 1531 Vertices are divided into two groups, primary vertices which correspond to the
 1532 actual proton-proton collisions, and secondary vertices which correspond to de-
 1533 cays of short-lived particles or interactions with the detector. Primary vertices
 1534 are particularly important for identifying the position of the interaction which
 1535 produced the event being measured and measuring its location is important in
 1536 order to understand the geometry of that event.

1537 Primary vertices are reconstructed by iteratively identifying seeds from re-
 1538 constructed tracks. Each track's extrapolated z position at the beamline forms a
 1539 seed, and nearby tracks are fitted using that position as a point along the trajec-
 1540 tory. The goodness of fit with that vertex is considered for each track, measured
 1541 in χ^2 , and the final position of the vertex is determined by a weighted fit where
 1542 the contribution from each track is weighted according to the χ^2 compatibility
 1543 with that vertex. Any tracks from this procedure that are displaced by more than

1544 7σ from that vertex are removed from the fit and used to seed a new vertex. This
 1545 procedure is iterated until no additional vertices can be found.

1546 This procedure is typically performed twice. The first set of vertices is used
 1547 to fit a profile for the beamspot, which indicates the position of the intersection
 1548 of beams in that particular bunch crossing. This fitted beamspot then provides
 1549 a constraint for the second attempt to locate primary vertices, where both the
 1550 track fitting and seeding of vertices are required to be consistent with interac-
 1551 tions occurring within the beamspot.

1552 7.2 ELECTRONS AND PHOTONS

1553 Electrons are measured as both a charged particle track and energy deposits in
 1554 the electromagnetic calorimeter. Photons, on the other hand, leave energy de-
 1555 posits in the electromagnetic calorimeter but do not produce a corresponding
 1556 track. Because the electromagnetic interactions with the calorimeter of both
 1557 photons and electrons produces more photons and electrons, the behaviour in
 1558 the calorimeter is the same and the same techniques can be used to identify both
 1559 particle types.

1560 The reconstruction of a photon or an electron in the calorimeter is based on
 1561 clustering algorithms which identify groups of energy deposits [13]. For this
 1562 purpose, the entire electromagnetic calorimeter is subdivided into a grid of 200
 1563 by 256 towers in the η and ϕ directions, respectively, where the individual grid
 1564 units have a size of $\Delta\eta = 0.025$ and $\Delta\phi = 0.025$. These towers correspond to
 1565 individual cells in the middle, coarsest layer of the EM calorimeter, and in the
 1566 remaining layers the cells are grouped together cover the same area in $\eta - \phi$
 1567 space. The clustering begins by finding seeds with a sliding-window algorithm
 1568 based on the towers: a window of 3x5 towers is formed and translated until the
 1569 sum of the energy within the window is maximized. If that energy is above 2.5
 1570 GeV, then that region becomes a seed. The choice of 2.5GeV was chosen to
 1571 compromise between maximizing reconstruction efficiency while minimizing
 1572 fake electron seeds from electronic noise or pileup. The seeds are rejected if the
 1573 energy measured in the hadronic calorimeter behind the seed is large, as this
 1574 typically indicates a hadron rather than an electron or photon.

1575 Next, the inner detector tracks within a cone of $\Delta R = 0.3$ are compared to
 1576 the location and energy of the seed. Tracks are matched to the cluster if the ex-
 1577 trapolation of the track to the energy-weighted center in the middle layer of the
 1578 EM calorimeter falls within $\Delta\phi < 0.2$ in the direction of the curvature of the
 1579 track or $\Delta\phi < 0.05$ in the direction opposite of the curvature of the track. If the
 1580 seed matches with a track that originated from a primary vertex, the combina-
 1581 tion of track and electromagnetic cluster is reconstructed as an electron. If the
 1582 seed matches with a track that did not originate from a primary vertex, then the
 1583 electromagnetic cluster is reconstructed as a converted photon. And if there is
 1584 no corresponding track in the inner detector, then the cluster is reconstructed
 1585 as a photon.

1586 After classification, the final clustering of the energy in the EM calorimeter
 1587 calorimeter is performed. The classification must be done first, as the expected

1588 size of the energy deposits in the calorimeter are different for electrons and pho-
 1589 tons. In the barrel region, the final clusters for electrons are formed in rectangles
 1590 of 3 towers in the η -direction and 7 towers in the ϕ -direction. This asymmetric
 1591 window accounts for the curving of the produced charged particles only in the
 1592 ϕ direction. For photons, the size of the rectangle is 3 towers by 5 towers. In the
 1593 endcap region, all object types are clustered in rectangels of 5 towers by 5 tow-
 1594 ers, as the effect of the magnetic field curvature is less pronounced in this region.
 1595 The sum of the energies in these clusters provide the final energy measurement
 1596 for the electron or photon.

1597 7.2.1 PHOTON IDENTIFICATION

1598 The original requirement for constructing a photon cluster, a significant energy
 1599 deposit in the electromagnetic calorimeter without a corresponding track or en-
 1600 ergy deposits in the hadronic calorimeter, is already effective in identifying pho-
 1601 tons. However, there is a significant background for prompt photon production
 1602 from the decays of pions, $\pi^0 \rightarrow \gamma\gamma$. These can be identified using the shape of
 1603 the cluster in the narrow η granularity in the first layer of the [EM](#) calorimeter.

1604 7.2.2 ELECTRON IDENTIFICATION

1605 Prompt electrons have a number of backgrounds, such as secondary electrons
 1606 from hadron decays or misidentified hadronic jets, that can be rejected using ad-
 1607 dditional information from the [EM](#) calorimeter and the inner detector. The most
 1608 basic level of electron identification, referred to as Loose, makes requirements
 1609 on the shower shapes in the high granularity first layer of the [EM](#) calorimeter
 1610 as well as the quality of the inner detector track. It also requires a good match
 1611 between the track and the calorimeter energy deposits and a small fraction of
 1612 energy in the hadronic calorimeter behind the electromagnetic cluster. [ATLAS](#)
 1613 defines several additional working points, including Medium and Tight, which
 1614 provide progressively lower background rates for electrons by imposing addi-
 1615 tionally strict requirements on the above variables as well as new requirements
 1616 like the impact parameter of the inner detector track or the comparison of the
 1617 cluster energy to the momentum in the inner detector.

1618 7.3 MUONS

1619 Muons produced in [ATLAS](#) first traverse the inner detector and leave behind a
 1620 track as described in Section 7.1. The muon then passes through the calorimeter,
 1621 leaving behind a small, characteristic amount of energy, and then passes through
 1622 the muon spectrometer where it produces hits in the [MDTs](#) or [CSCs](#). Muon tracks
 1623 are formed from local segments of hits in each layer of the [MDTs](#) or [CSCs](#), and
 1624 then the final muon spectrometer track is formed by combining the two local
 1625 segments. When a track is reconstructed in both the inner detector and the muon
 1626 spectrometer, they are combined to form a combined muon.

1627 In a few regions of the detector, a muon may fail to leave behind both a com-
 1628 plete inner detector and muon system track. For a very small fraction of the
 1629 acceptance of the muon system, there is only one layer of muon chambers and a
 1630 global muon system track is not formed. In this case, as long as the track in the
 1631 inner detector exists and geometrically matches to a segment, a segment-tagged
 1632 muon is formed using momentum measurements from the inner detector. In
 1633 the region where the muon system has coverage but the inner detector does not,
 1634 $2.5 < |\eta| < 2.7$, a stand-alone muon is formed which uses only information from
 1635 the muon system. And muons produced within one of the few holes in the muon
 1636 system, including $|\eta| < 0.1$, the characteristic energy deposits in the calorimeter
 1637 can be used to tag an inner detector track as a calo-tag muon. These additional
 1638 categories are used to achieve high efficiency over a larger range of acceptance,
 1639 but the combined muons are the most reliable.

1640 7.3.1 MUON IDENTIFICATION

1641 The various types of muons are incorporated into three working points: Loose,
 1642 Medium, and Tight, which reflect the increasing muon purity for each of the
 1643 selections definitions. Tight muons include only combined muons with a good
 1644 track fit quality and momentum resolution and at least two hits in a precision
 1645 muon system layer. Medium muons include those in tight as well as combined
 1646 muons with one precision hit and one precision hole, where hole is defined in
 1647 the same way as in Section 7.1. The medium working point also includes stand-
 1648 alone muons with $|\eta| > 2.5$ and at least two hits in precision layers. And finally
 1649 the loose working point includes both medium and tight muons, but additional
 1650 includes segment-tagged and calo-tagged muons in the region $|\eta| < 0.1$.

1651 7.4 JETS

1652 A jet does not directly correspond to a physical particle, unlike all of the recon-
 1653 structed objects described above, but instead tries to capture the conical cascade
 1654 of particles produced in the hadronization of a quark or gluon from the proton-
 1655 proton collision. The hadronization process creates a very large number of col-
 1656 limated particles, with a high enough density that individually reconstructing all
 1657 of the produced particles in the calorimeter is not possible within ATLAS. How-
 1658 ever most analyses are interested only in the kinematics of the particle which
 1659 produced the cascade, rather than the individual products. Therefore, jets are
 1660 a useful tool to measure the combined energy and direction of the ensemble of
 1661 products and thus represents the kinematics of the original. Jet algorithms are
 1662 very generic and can be used to group together a number of types of objects to
 1663 form aggregate representations. For example, truth particles in simulation can
 1664 be grouped in truth jets, or tracks from the inner detector can be grouped to-
 1665 gether to form track jets. This section, however, will focus on calorimeter jets
 1666 which take topoclusters of energy deposits in the calorimeter as inputs and pro-
 1667 duce a combined object which represents the energy measured by the calorime-
 1668 ter and the location where it was deposited.

1669 74.1 TOPOLOGICAL CLUSTERING

1670 Hadrons often deposit their energy into multiple individual cells in both the elec-
 1671 tromagnetic and hadronic calorimeters. The purpose of topological clustering is
 1672 to group cells in all three dimensions into clusters that represent a single energy
 1673 deposit. The procedure must be robust enough to reject noise fluctuations in
 1674 the cell energy measurements that can come from both electronic noise and ad-
 1675 dditional low energy particles produced in pileup activity. The background level
 1676 of calorimeter noise is called σ_{noise} , and is an important component of the topo-
 1677 logical clustering.

1678 The topological clusters are formed in a three step process called the 4-2-0
 1679 threshold scheme consistent of four classification of cells. Seed cells are any cell
 1680 with a measured energy above $4\sigma_{\text{noise}}$. Secondary cells are those adjacent to a
 1681 seed or to another secondary cell as long as they have a measured energy above
 1682 $2\sigma_{\text{noise}}$. Tertiary cells are those immediately adjacent to a seed or secondary cell
 1683 with a measured energy above zero. Adjacency in this sense is defined in three
 1684 dimensions, cells are adjacent if they are neighbors within a layer but also if they
 1685 have the same $\eta - \phi$ coordinates but are in adjacent layers or even in an adjacent
 1686 layer in another calorimeter.

1687 From these definitions, clusters are built by resolving the seeds in order of
 1688 significance, the ratio of $E_{\text{cell}}/\sigma_{\text{noise}}$. All adjacent secondary cells to the highest
 1689 significance seed are added to that seed's topocluster, and any of those cells which
 1690 would also have qualified as seeds are removed from the list of seeds. Once all
 1691 of the secondary cells have been added, the tertiary cells are then added to that
 1692 cluster as well. This procedure is then iterated until no seeds remain, forming
 1693 the first round of topoclusters.

1694 It is also useful to split topoclusters into multiples if local maxima are present
 1695 within the topocluster, as clusters produced by multiple nearby particles can
 1696 merge. The splitting process begins by finding local maxima cells in the middle
 1697 layer of the calorimeters with a minimum energy of 500 MeV and at least four
 1698 neighboring secondary cells. These requirements reduce the likelihood to split
 1699 a cluster due to random fluctuations, as the middle layers provide the most reli-
 1700 able energy measurements. Cells between two local maxima can then be shared
 1701 between two clusters to account for overlapping contributions from two parti-
 1702 cles. The energy sharing is weighted by the energy of each cluster as well as the
 1703 distance of the cell to the centroid of that cluster.

1704 The energies of all the cells in the cluster are then summed together to form
 1705 the energy of that cluster. The energy needs to be corrected for the various losses
 1706 expected in the calorimeter, as described in Section 6.4. The simplest correction,
 1707 scaling the measured energy by the sampling fraction, brings the cluster energies
 1708 to the EM scale. It is called the EM scale because it does a good job of describing
 1709 the energy of electromagnetic showers.

1710 Another scale is defined for hadronic processes, the local cluster weighted
 1711 (LCW) scale, that helps to correct for the expected variations in hadronic en-
 1712 ergy deposits. The LCW correction first determines if the shower is hadronic
 1713 or electromagnetic, based on the depth of the shower and the cluster energy

density. For hadronic showers, the energy is corrected for calorimeter non-compensation, an effect which reduces the measured energy of hadronic showers because some of the energy goes into invisible processes like the break up of nuclei. All clusters are then corrected for energy that may be deposited in uninstrumented regions in that cluster's location in the calorimeter, and they are also corrected with an estimate of how much energy falls outside the extent of the cluster based on its shape and the deposit type.

7.4.2 JET ALGORITHMS

Using the topological clusters as inputs, a jet algorithm groups them together into a collection of adjacent energy deposits that is intended to correspond to a single process. Jet algorithms need a few key characteristics to be useable for physics analysis. First, the jets produced by the algorithm should have little dependence on the addition of soft particles to the event (infrared safety), as a negligible addition of energy should not significantly modify the event topology. Similarly, the jets produced by the algorithm should also not significantly depend on mostly collinear splitting of an input particle (collinear safety); that is, a single quark splitting into two nearly parallel quarks should not change the resulting jets, which are intended to capture only the properties of the aggregate and not those of individual particles. And finally the algorithm needs to be sufficiently simple and fast to be used for the large rate of collected proton-proton collisions on [ATLAS](#).

The most commonly used algorithm on [ATLAS](#) that satisfies these requirements is called the anti- k_t algorithm, and is discussed in further detail in Reference [14]. The anti- k_t , in brief, relies on iteratively combining the input objects that are closest together, where closest is defined by the a particular distance metric, $d_{i,j}$. The combinations stop when the closest remaining object is the beam itself, where the distance to the beam is called $d_{i,B}$. An entire class of algorithms follows this procedure with the following distance metrics

$$d_{i,j} = \min(k_{ti}^{2p}, k_{tj}^{2p}) \frac{\Delta_{ij}^2}{R^2} \quad (6)$$

$$d_{i,B} = k_{ti}^{2p} \quad (7)$$

where $\Delta_{ij} = (y_i - y_j)^2 + (\phi_i - \phi_j)^2$, k_{ti} is the transverse momentum of the object, y is the rapidity, and p is a parameter of the algorithm. Anti- k_t is the particular case where $p = -1$, and is a choice that results in an algorithm that is both infrared and collinear safe.

The algorithm is repeated until there are no input objects remaining, which results in a series of jets. Each jet has a complete four momentum from the combination of its input clusters. The jet energies then need to be calibrated to attempt to match the energy of the object which produced the jet.

1750 74.3 JET ENERGY SCALE

1751 Though the [LCW](#) scheme attempts to correct the topoclusters to reflect the true
 1752 deposited energy, the correction does not fully account for energy lost within
 1753 the calorimeters. Because of these effects, the original reconstructed jet energy
 1754 does not reflect the true energy of the particle which initiated the jet. Therefore
 1755 it is necessary to additionally correct the reconstructed jet itself, in addition to
 1756 the corrections on the inputs. This correction is referred to as the [JES](#), which
 1757 combines several individual steps of calibration.

1758 The first calibration step corrections the direction of the jet to ensure that it
 1759 points back to the primary vertex. Next, the energy of the jet is corrected for
 1760 pileup by subtracting the expected contribution from pileup (measured in simu-
 1761 lation) based on the momentum, η , and area of the jet as well as the number of
 1762 reconstructed vertices and expected number of interactions per crossing. The
 1763 largest single correction is the absolute η and [JES](#) correction, where the jet energy
 1764 and pseudorapidity is corrected to attempt to match the energy and pseudorapid-
 1765 ity of the parton which produced it. The correction is measured in simulation
 1766 by comparing the reconstructed jet energies to the energy of the truth particle
 1767 which produced it. However the simulation is not relied on alone to estimate
 1768 this correction, and an additional step applies an additional energy correction
 1769 based on in-situ measurements in data. These corrections come from various
 1770 techniques which measure jet energies indirectly by balancing them with other,
 1771 well-measured objects. In the central region ($|\eta| < 1.2$, jets are balanced against
 1772 photons and the leptonic decays of Z bosons and high momentum jets ($p_T > 210$
 1773 GeV) are also balanced against multiple smaller jets in multijet events. Jets at
 1774 larger pseudorapidities, above $|\eta| = 1.2$, are calibrated by balancing them with
 1775 lower pseudorapidity jets.

1776 These steps introduce a number of systematic uncertainties, referred to as
 1777 the [JES](#) uncertainty. The largest of these comes from the in-situ measurements,
 1778 which are statistically limited in measuring high momentum and high pseudora-
 1779 pidity jets. The total, fractional [JES](#) uncertainty is shown as a function of p_T in
 1780 Figure 37. The uncertainty falls to a minimum value of just over 1.0% around
 1781 a few hundred GeV, and raises again at high momentum because of the diffi-
 1782 culty of measuring jet balance in data above 2-3 TeV. The uncertainty is also
 1783 minimized at low $|\eta|$, and grows at large $|\eta|$ again where making in-situ mea-
 1784 surements is difficult. This technique does not actually provide a measurement
 1785 of the uncertainty for the highest energy jets, above 3 TeV, because there are not
 1786 enough measured data events to provide them. An alternative method for deriv-
 1787 ing the [JES](#) and [JES](#) uncertainty that can be used even for very high p_T jets will be
 1788 discussed in Chapter 9.

1789 7.5 MISSING TRANSVERSE ENERGY

1790 Among [SM](#) particles, only the neutrino cannot be directly measured in the [ATLAS](#)
 1791 detector. Because the neutrino carries neither electric nor color charge, it is very
 1792 unlikely to interact with the tracking detectors or the calorimeters, and instead

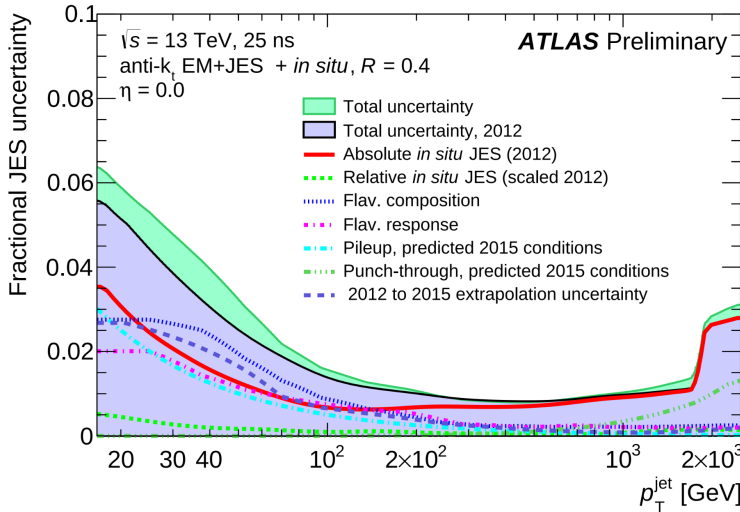


Figure 37: The total, fractional JES uncertainties estimated for 2015 data as a function of jet p_T .

1793 passes through the detector completely unobserved. Some particles which have
 1794 been conjectured to exist, like the LSP in many SUSY models, would also have
 1795 the same behavior. Therefore, it is important for ATLAS to provide some way to
 1796 assess the momentum carried away by an neutral, colorless particles. This can
 1797 be accomplished through a measurement of missing energy in the transverse di-
 1798 rection, or E_T^{miss} , which quantifies the momentum imbalance of the observed
 1799 particles. From the conservation of momentum and the lack of the initial mo-
 1800 mentum in the transverse plane in the proton-proton collisions, any imbalance
 1801 of momentum can be inferred to be carried away by an unmeasured particle.

1802 E_T^{miss} is more precisely defined as the magnitude of the vector sum of the
 1803 (p_x, p_y) components of each observed object's momentum. The definition is
 1804 simple, but their can be significant complexity in defining the inputs. As of Run
 1805 2, ATLAS uses a common algorithmic approach to carefully calculate missing en-
 1806 ergy, but each analysis is free to define it's own inputs. For the analysis discussed
 1807 throughout this thesis, the missing energy inputs consist of the electrons, pho-
 1808 tons, muons, and jets discussed in the previous sections, in addition to a track-
 1809 based soft term.

1810 To produce the most precise measurement of E_T^{miss} , it is important to use the
 1811 best representation of the momentum of each of the input objects, which can
 1812 often be reconstructed as multiple different types in a single event. For example,
 1813 an electron can be reconstructed separately as an electron (Section 7.2) and a
 1814 jet (Section 7.4), but the electron representation has the highest precision for
 1815 reconstructing the true electron momentum. To ensure no duplications in the
 1816 E_T^{miss} definition, the inputs are collectively considered for overlap removal. Only
 1817 the most precise object type is kept for objects that fall within a cone of $\Delta R < 0.2$
 1818 for pairs of electrons and jets and a cone of $\Delta R < 0.4$ for other pair types.

1819 The fully reconstructed objects do not include all of the energy within the
 1820 events, as some clusters do not enter into a jet and some tracks are not classified
 1821 as electrons or muons. These momentum carried by these objects is accounted

1822 for in a soft-term, which tallies all of the energy carried by the particles too soft
1823 to form separate objects. The track soft term uses only tracking information to
1824 estimate the contribution of soft objects, and does so by vectorially summing the
1825 momentum of all well-reconstructed tracks with momentum above 400 MeV.

1826 All of these contributions together give a single E_T^{miss} value for a given event.
1827 The direction of that missing energy is taken as opposite the vector sum of all the
1828 constituents, to correspond to the momentum an invisible particle would have to
1829 have to make the event balanced. Depending on the context, this missing energy
1830 can be considered the energy of a neutrino or an LSP, with a large missing energy
1831 being a common signal criteria for searches for new physics.

1832

PART IV

1833

CALORIMETER RESPONSE

1834

You can put some informational part preamble text here.

1835

1836 RESPONSE MEASUREMENT WITH SINGLE HADRONS

1837 As discussed in Section 7.4, colored particles produced in collisions hadronize
1838 into jets of multiple hadrons. One approach to understanding jet energy mea-
1839 surements in the ATLAS calorimeters is to evaluate the calorimeter response to
1840 those individual hadrons; measurements of individual hadrons can be used to
1841 build up an understanding of the jets that they form. The redundancy of the
1842 momentum provided by the tracking system and the energy provided by the
1843 calorimeter provides an opportunity to study calorimeter response using real
1844 collisions, as described further in Section 8.2.

1845 Calorimeter response includes a number of physical effects that can be ex-
1846 tracted to provide insight into many aspects of jet modeling. First, many charged
1847 hadrons interact with the material of the detector prior to reaching the calorime-
1848 ters and thus do not deposit any energy. Comparing this effect in data and simu-
1849 lation is a powerful tool in validating the interactions of particles with the mate-
1850 rial of the detector and the model of the detector geometry in simulation, see Sec-
1851 tion 8.2.2. The particles which do reach the calorimeter deposit their energy into
1852 several adjacent cells, which are then clustered together. The energy of the clus-
1853 ter is then the total energy deposited by that particle. Comparing the response of
1854 hadrons in data to that of simulated hadrons provides a direct evaluation of the
1855 showering of hadronic particles and the energy deposited by particles in matter
1856 (Section 8.2.4).

1857 The above studies all use an inclusive selection of charged particles, which are
1858 comprised predominantly of pions, kaons, and (anti)protons. It is also possible to
1859 measure the response to various identified particle types separately to evaluate
1860 the simulated interactions of each particle, particularly at low energies where
1861 differences between species are very relevant. Pions and (anti)protons can be
1862 identified through decays of long-lived particles, in particular Λ , $\bar{\Lambda}$, and K_S^0 , and
1863 then used to measure response as described above. This is discussed in detail in
1864 Section 8.3.

1865 The results in this chapter use data collected at 7 and 8 TeV collected in 2010
1866 and 2012, respectively. Both are included as the calorimeter was repaired and
1867 recalibrated between those two data-taking periods. Both sets of data are com-
1868 pared to an updated simulation that includes new physics models provided by
1869 Geant4 [15] and improvements in the detector description [16, 17]. The present
1870 results are published in European Physical Journal C (EPJC) [18] and can be com-
1871 pared to a similar measurement performed in 2009 and 2010 [19], which used
1872 the previous version of the simulation framework [20].

1873 8.1 DATASET AND SIMULATION

1874 8.1.1 DATA SAMPLES

1875 The two datasets used in this chapter are taken from dedicated low-pileup runs
 1876 where the fraction of events with multiple interactions was negligible. These
 1877 datasets are used rather than those containing full-pileup events to facilitate mea-
 1878 surement of isolated hadrons. The 2012 dataset at $\sqrt{s} = 8$ TeV contains 8 mil-
 1879 lion events and corresponds to an integrated luminosity of 0.1 nb^{-1} . The 2010
 1880 dataset at $\sqrt{s} = 7$ TeV contains 3 million events and corresponds to an inte-
 1881 grated luminosity of 3.2 nb^{-1} . The latter dataset was also used for the 2010 re-
 1882 sults [19], but it has since been reanalyzed with an updated reconstruction in-
 1883 cluding the final, best understanding of the detector description for the material
 1884 and alignment from Run 1.

1885 8.1.2 SIMULATED SAMPLES

1886 The two datasets above are compared to simulated single-, double-, and non-
 1887 diffractive events generated with Pythia8 [21] using the A2 configuration of
 1888 hadronization [22] and the MSTW 2008 parton-distribution function set [23,
 1889 24]. The admixture of the single-, double-, and non-diffractive events uses the
 1890 default relative contributions from Pythia8. The conditions and energies for
 1891 the two simulations are chosen so that they match those of the corresponding
 1892 dataset.

1893 To evaluate the interaction of hadrons with detector material, the simulation
 1894 uses two different collections of hadronic physics models, called physics lists, in
 1895 Geant4 9.4 [25]. The first, QGSP_BERT, combines the Bertini intra-nuclear
 1896 cascade [26–28] below 9.9 GeV, a parametrized proton inelastic model from 9.5
 1897 to 25 GeV [29], and a quark-gluon string model above 12 GeV [30–34]. The
 1898 second, FTFP_BERT, combines the Bertini intra-nuclear cascade [26–28] below
 1899 5 GeV and the Fritiof model [35–38] above 4 GeV. In either list, Geant4 en-
 1900 forces a smooth transition between models where multiple models overlap.

1901 8.1.3 EVENT SELECTION

1902 The event selection for this study is minimal, as the only requirement is selecting
 1903 good-quality events with an isolated track. Such events are triggered by requir-
 1904 ing at least two hits in the minimum-bias trigger scintillators. After trigger, each
 1905 event is required to have exactly one reconstructed vertex, and that vertex is re-
 1906 quired to have four or more associated tracks.

1907 The particles which are selected for the response measurements are first iden-
 1908 tified as tracks in the inner detector. The tracks are required to have at least 500
 1909 MeV of transverse momentum. To ensure a reliable momentum measurement,
 1910 these tracks are required to have at least one hit in the pixel detector, six hits in
 1911 the SCT, and small longitudinal and transverse impact parameters with respect
 1912 to the primary vertex [19]. For the majority of the measurements in this chapter,

1913 the track is additionally required to have 20 hits in the TRT, which significantly
 1914 reduces the contribution from tracks which undergo nuclear interactions. This
 1915 requirement and its effect is discussed in more detail in Section 8.2.5. In addition,
 1916 tracks are rejected if there is any other reconstructed track which extrapolates
 1917 to the calorimeter within a cone of $\Delta R = \sqrt{(\Delta\phi)^2 + (\Delta\eta)^2} < 0.4$. This require-
 1918 ment guarantees that the contamination of energy from nearby charged particles
 1919 is negligible [19].

1920 8.2 INCLUSIVE HADRON RESPONSE

1921 The calorimeter response is more precisely defined as the ratio of the measured
 1922 calorimeter energy to the true energy carried by the particle, although this true
 1923 energy is unknown. For charged particles, however, the inner detector provides
 1924 a very precise measurement of momentum (with uncertainty less than 1%) that
 1925 can be used as a proxy for true energy. The ratio of the energy deposited by
 1926 the charged particle in the calorimeter, E , to its momentum measured in the
 1927 inner detector p , forms the calorimeter response measure called E/p . Though
 1928 the distribution of E/p contains a number of physical features, this study focuses
 1929 on the trends in two aggregated quantities: $\langle E/p \rangle$, the average of E/p for the
 1930 selected tracks, and the zero fraction, the fraction of tracks with no associated
 1931 energy in the calorimeter for those tracks.

1932 The calorimeter energy assigned to a track is defined using clusters. The clus-
 1933 ters are formed using a 4–2–0 algorithm [39] that begins with seeds requiring
 1934 at least 4 times the average calorimeter cell noise. The neighboring cells with
 1935 at least twice that noise threshold are then added to the cluster, and all bound-
 1936 ing cells are then added with no requirement. This algorithm minimizes noise
 1937 contributions through its seeding process, and including the bounding cells im-
 1938 proves the energy resolution [40]. The clusters are associated to a given track
 1939 if they fall within a cone of $\Delta R = 0.2$ of the extrapolated position of the track,
 1940 which includes about 90% of the energy on average [19]. This construction is
 1941 illustrated in Figure 38.

1942 8.2.1 E/P DISTRIBUTION

1943 The E/p distributions measured in both data and simulation are shown in Fig-
 1944 ure 39 for two example bins of track momentum and for tracks in the central
 1945 region of the detector. These distributions show several important features of
 1946 the E/p observable. The large content in the bin at $E = 0$ comes from tracks that
 1947 have no associated cluster, which occurs due to interactions with detector mate-
 1948 rial prior to reaching the calorimeter or the energy deposit being insufficiently
 1949 large to generate a seed, and are discussed in Section 8.2.2. The small negative
 1950 tail also comes from tracks that do not deposit any energy in the calorimeter but
 1951 are randomly associated to a cluster with an energy below the noise threshold.
 1952 The long positive tail above 1.0 comes from the contribution of neutral parti-
 1953 cles. Nearby neutral particles deposit (sometimes large) additional energy in the
 1954 calorimeter but do not produce tracks in the inner detector, so they cannot be

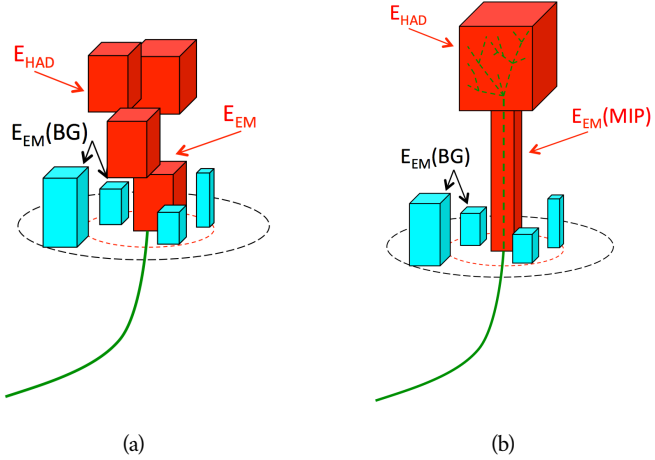


Figure 38: An illustration (a) of the E/p variable used throughout this paper. The red energy deposits come from the charged particle targeted for measurement, while the blue energy deposits are from nearby neutral particles and must be subtracted. The same diagram (b) for the neutral-background selection, described in Section 8.2.3.

1955 rejected by the track isolation requirement. Additionally the peak and mean of
 1956 the distribution falls below 1.0 because of the loss of energy not found within
 1957 the cone as well as the non-compensation of the calorimeter.

1958 The data and simulation share the same features, but the high and low tails
 1959 are significantly different. The simulated events tend to overestimate the con-
 1960 tribution of neutral particles to the long tail, an effect which can be isolated and
 1961 removed as discussed in Section 8.2.3. Additionally, the simulated clusters have
 1962 less noise on average, although this is a small effect on the overall response.

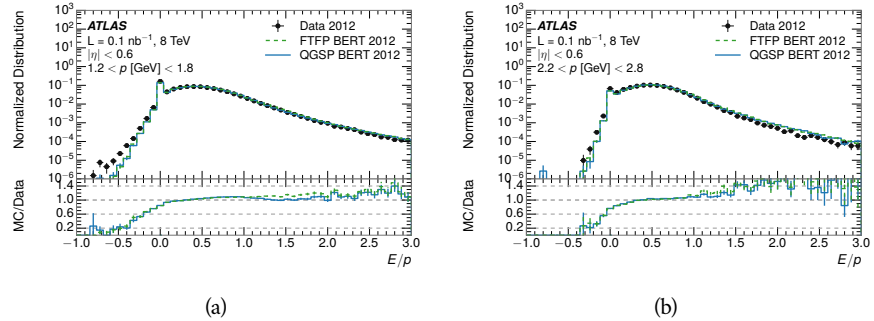


Figure 39: The E/p distribution and ratio of simulation to data for isolated tracks with (a) $|\eta| < 0.6$ and $1.2 < p/\text{GeV} < 1.8$ and (b) $|\eta| < 0.6$ and $2.2 < p/\text{GeV} < 2.8$.

1963 8.2.2 ZERO FRACTION

1964 The fraction of particles with no associated clusters, or similarly those with $E \leq$
 1965 0, reflects the modeling of both the detector geometry and hadronic interactions.

1966 The zero fraction is expected to rise as the amount of material a particle traverses
 1967 increases, while it is expected to decrease as the particle energy increases. This
 1968 dependence can be seen in Figure 40, where the zero fraction in data and simulation
 1969 is shown as a function of momentum and the amount of material measured
 1970 in interaction lengths. The trends are similar between 2010 and 2012 and for
 1971 positively and negatively charged particles. The zero fraction decreases with
 1972 energy as expected. The absolute discrepancy in zero fraction decreases with
 1973 momentum from 5% to less than 1%, but this becomes more pronounced in the
 1974 ratio as the zero fraction shrinks quickly with increasing momentum. There is
 1975 a small constant difference between the data and simulation in both interaction
 1976 models that becomes more pronounced. The amount of material in the detector
 1977 increases with η , which is used to obtain results for interaction lengths ranging
 1978 between 0.1 and 0.65 λ . As the data and simulation have significant disagree-
 1979 ment in the zero fraction over a number of interaction lengths, the difference
 1980 must be primarily from the modeling of hadronic interactions with detector ma-
 1981 terial and not just the detector geometry. Although two different hadronic in-
 1982 teraction models are shown in the figure, they have very similar discrepancies to
 1983 data because both use the same description (the BERT model) at low momentum.

1984 8.2.3 NEUTRAL BACKGROUND SUBTRACTION

1985 The isolation requirement on hadrons is only effective in removing an energy
 1986 contribution from nearby charged particles. Nearby neutral particles, predomi-
 1987 nantly photons from π^0 decays, also add their energy to the calorimeter clusters,
 1988 but mostly in the electromagnetic calorimeter. It is possible to measure this con-
 1989 tribution, on average, using late-showering hadrons that minimally ionize in the
 1990 electromagnetic calorimeter. Such particles are selected by requiring that they
 1991 deposit less than 1.1 GeV in the EM calorimeter within a cone of $\Delta R < 0.1$
 1992 around the track. To ensure that these particles are well measured, they are addi-
 1993 tionally required to deposit between 40% and 90% of their energy in the hadronic
 1994 calorimeter within the same cone.

1995 These particles provide a clean sample to measure the nearby neutral back-
 1996 ground because they do not deposit energy in the area immediately surrounding
 1997 them in the EM calorimeter, as shown in Figure 38. So, the energy deposits in the
 1998 region $0.1 < \Delta R < 0.2$ can be attributed to neutral particles alone. To estimate
 1999 the contribution to the whole cone considered for the response measurement,
 2000 that energy is scaled by a geometric factor of 4/3. This quantity, $\langle E/p \rangle_{BG}$, mea-
 2001 sured in aggregate over a number of particles, gives the contribution to $\langle E/p \rangle$
 2002 from neutral particles in the EM calorimeter. Similar techniques were used in
 2003 the individual layers of the hadronic calorimeters to show that the background
 2004 from neutrals is negligible in those layers [19].

2005 The distribution of this background estimate is shown in Figure 41 for data
 2006 and simulation with the two different physics lists. The contribution from neu-
 2007 tral particles falls from 0.1 at low momentum to around 0.03 for particles above
 2008 7 GeV. Although the simulation captures the overall trend, it significantly over-
 2009 estimates the neutral contribution for tracks with momentum between 2 and 8

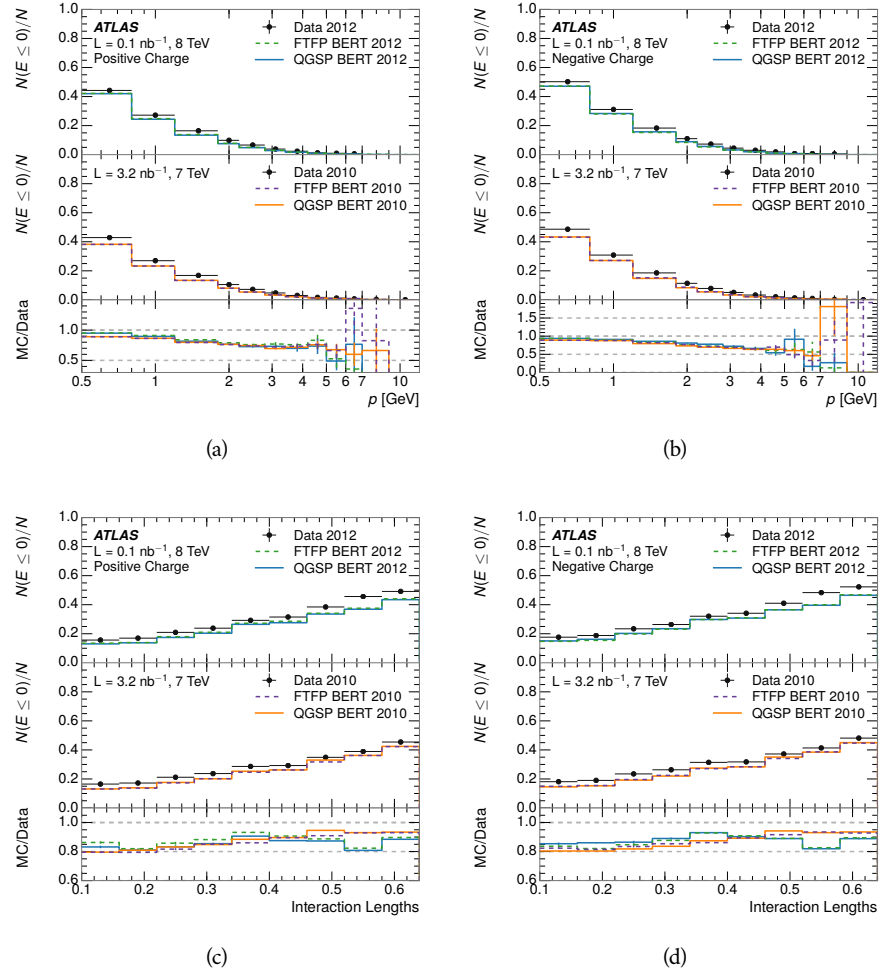


Figure 40: The fraction of tracks as a function (a, b) of momentum, (c, d) of interaction lengths with $E \leq 0$ for tracks with positive (on the left) and negative (on the right) charge.

2010 GeV. This effect was also seen in the tails of the E/p distributions in Figure 39.
 2011 This difference is likely due to modeling of coherent neutral particle radiation
 2012 in Pythia8 that overestimates the production of π^0 near the production of the
 2013 charged particles. The discrepancy does not depend on η and thus is unlikely to
 2014 be a mismodeling of the detector. This difference can be subtracted to form a
 2015 corrected average E/p , as in Section 8.2.4.

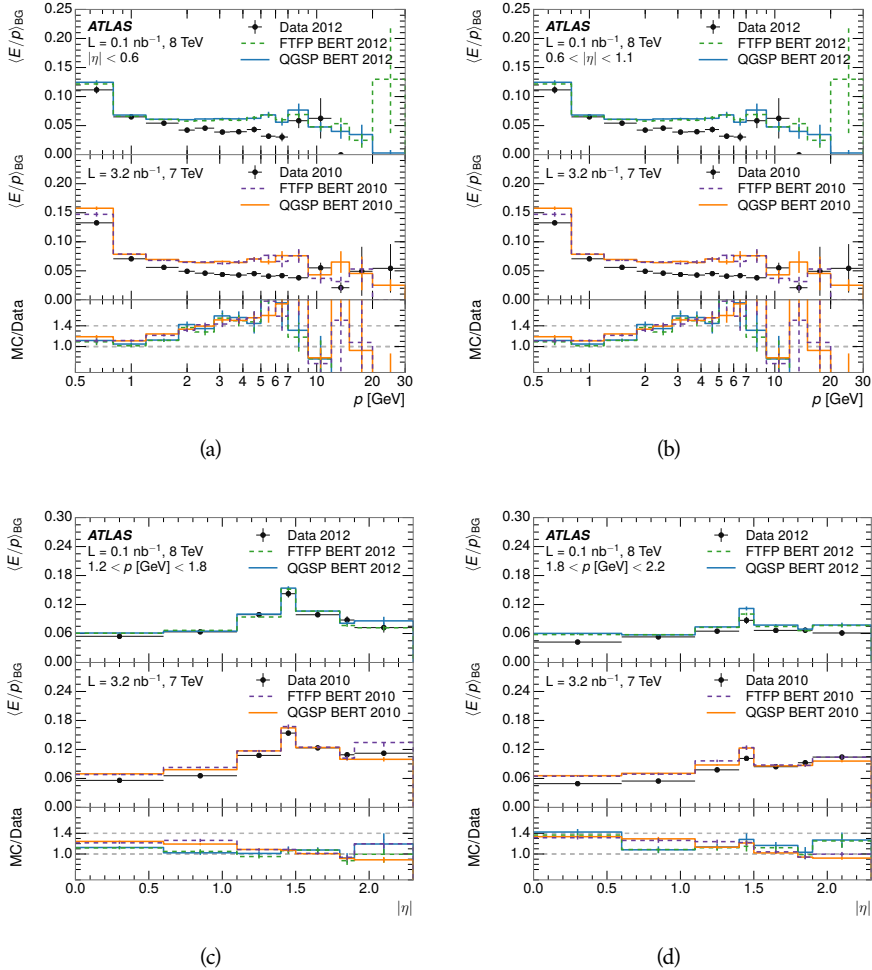


Figure 41: $\langle E/p \rangle_{BG}$ as a function of the track momentum for tracks with (a) $|\eta| < 0.6$,
 (b) $0.6 < |\eta| < 1.1$, and as a function of the track pseudorapidity for tracks
 with (c) $1.2 < p/\text{GeV} < 1.8$, (d) $1.8 < p/\text{GeV} < 2.2$.

2016 8.2.4 CORRECTED RESPONSE

2017 Figure 42 shows $\langle E/p \rangle_{COR}$ as a function of momentum for several bins of pseudo-
 2018 rapidity. This corrected $\langle E/p \rangle_{COR} \equiv \langle E/p \rangle - \langle E/p \rangle_{BG}$ measures the average
 2019 calorimeter response without the contamination of neutral particles. It is the
 2020 most direct measurement of calorimeter response in that it is the energy mea-
 2021 sured for fully isolated hadrons. The correction is performed separately in data
 2022 and simulation, so that the mismodeling of the neutral background in simulation

2023 is removed from the comparison of response. The simulation overestimates the
 2024 response at low momentum by about 5%, an effect that can be mostly attributed
 2025 to the underestimation of the zero fraction mentioned previously. For $|\eta| < 0.6$,
 2026 the data-simulation agreement has a larger discrepancy by about 5% for 2010
 2027 than 2012, although this is not reproduced in at higher pseudorapidity.

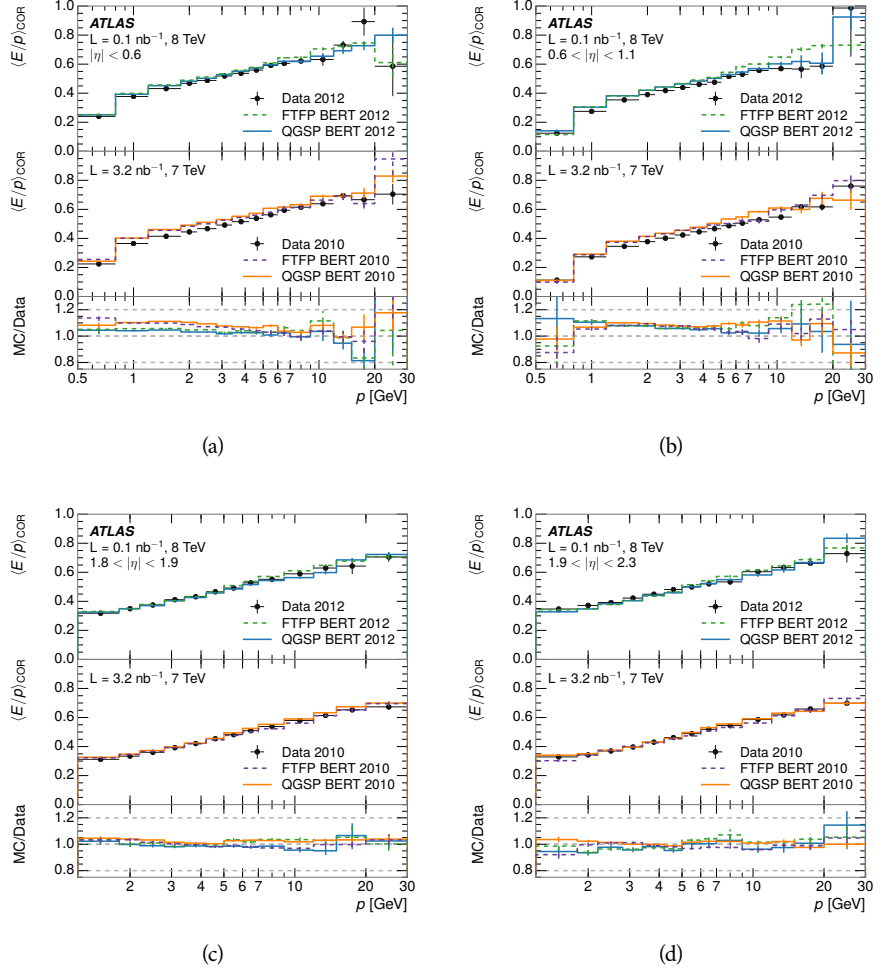


Figure 42: $\langle E/p \rangle_{\text{COR}}$ as a function of track momentum, for tracks with (a) $|\eta| < 0.6$, (b) $0.6 < |\eta| < 1.1$, (c) $1.8 < |\eta| < 1.9$, and (d) $1.9 < |\eta| < 2.3$.

2028 The response measurement above used topological clustering at the EM scale,
 2029 that is clusters were formed to measure energy but no corrections were applied
 2030 to correct for expected effects like energy lost outside of the cluster or in unin-
 2031 strumented material. It is also interesting to measure $\langle E/p \rangle_{\text{COR}}$ using LCW en-
 2032 ergies, which accounts for those effects by calibrating the energy based on the
 2033 properties of the cluster such as energy density and depth in the calorimeter.
 2034 Figure 43 shows these distributions for tracks with zero or more clusters and
 2035 separately for tracks with one or more clusters. The calibration moves the mean
 2036 value of $\langle E/p \rangle_{\text{COR}}$ significantly closer to 1.0 as desired. The agreement between
 2037 data and simulation improves noticeably when at least one cluster is required, as
 2038 this removes the contribution from the mismodeling of the zero fraction. The

good agreement in that case again demonstrates that the difference in $\langle E/p \rangle_{\text{COR}}$ between data and simulation is caused predominantly by the difference in zero fraction.

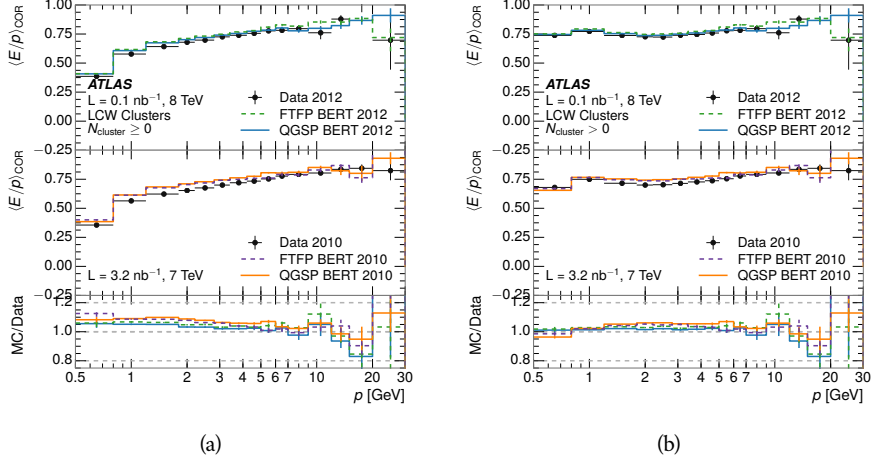


Figure 43: $\langle E/p \rangle_{\text{COR}}$ calculated using LCW-calibrated topological clusters as a function of track momentum for tracks with (a) zero or more associated topological clusters or (b) one or more associated topological clusters.

8.2.5 ADDITIONAL STUDIES

As has been seen in several measurements in previous sections, the simulation does not correctly model the chance of a low momentum hadron to reach the calorimeter. Because of the consistent discrepancy across pseudorapidity and interaction lengths, this can be best explained by incomplete understanding of hadronic interactions with the detector [18]. For example, a hadron that scatters off of a nucleus in the inner detector can be deflected through a significant angle and not reach the expected location in the calorimeter. In addition, these interactions can produce secondary particles that are difficult to model.

The requirement used throughout the previous sections on the number of hits in the TRT reduces these effects by preferentially selecting tracks that do not undergo nuclear interactions. It is interesting to check how well the simulation models tracks with low numbers of TRT hits, which selects tracks that are more likely to have undergone a hadronic interaction. Figure 44 compares the distributions with $N_{\text{TRT}} < 20$ to $N_{\text{TRT}} > 20$ for real and simulated particles. As expected, the tracks with fewer hits are poorly modeled in the simulation as $\langle E/p \rangle_{\text{COR}}$ differs by as much as 25% at low momentum.

Another interesting aspect of the simulation is the description of antiprotons at low momentum, where QGSP_BERT and FTFP_BERT have significant differences. This can be seen to have an effect in the inclusive response measurement when separated into positive and negative charge. The $\langle E/p \rangle_{\text{COR}}$ distributions for positive and negative particles are shown in Figure 45, where a small difference between QGSP_BERT and FTFP_BERT can be seen in the distribution for

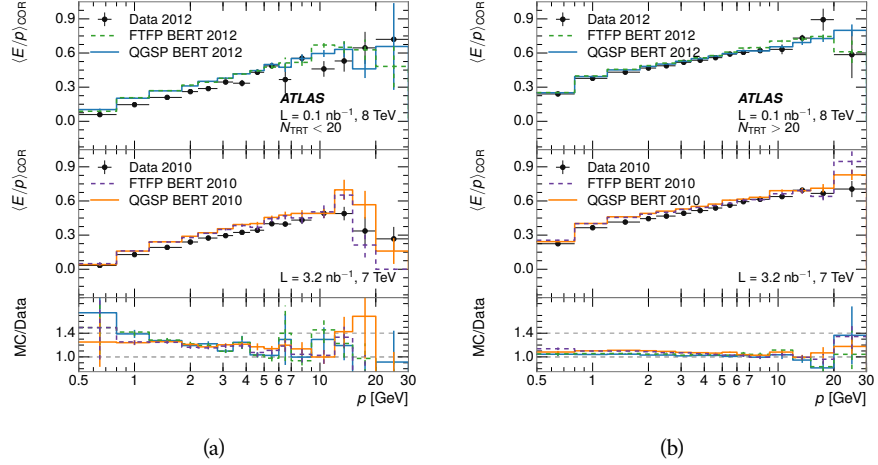


Figure 44: Comparison of the $\langle E/p \rangle_{\text{COR}}$ for tracks with (a) less than and (b) greater than 20 hits in the TRT.

negative tracks. This is demonstrated more clearly in Figure 46, which shows the E/p distribution in the two simulations separated by charge. There is a clear difference around $E/p > 1.0$, which can be explained by the additional energy deposited by the annihilation of the antiproton in the calorimeter that is modeled well only in FTFP_BERT. This is also explored with data using identified antiprotons in Section 8.3.

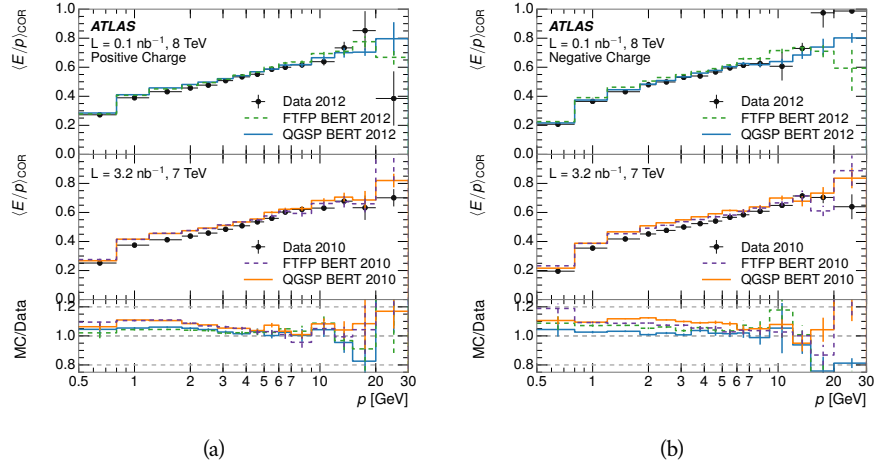


Figure 45: Comparison of the $\langle E/p \rangle_{\text{COR}}$ for (a) positive and (b) negative tracks as a function of track momentum for tracks with $|\eta| < 0.6$.

The $\langle E/p \rangle$ results in previous sections have considered the electromagnetic and hadronic calorimeters together as a single energy measurement, to emphasize the total energy deposited for a given particle. However, the deposits in each calorimeter are available separately and $\langle E/p \rangle$ can be constructed for each layer. As the layers are composed of different materials and are modeled separately in the detector geometry, confirmation that the simulation matches the data well

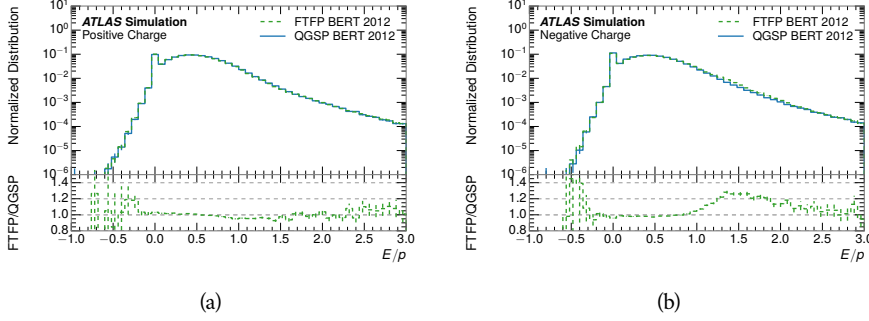


Figure 46: Comparison of the E/p distributions for (a) positive and (b) negative tracks with $0.8 < p/\text{GeV} < 1.2$ and $|\eta| < 0.6$, in simulation with the FTFP_BERT and QGSP_BERT physics lists.

in each layer adds confidence in both the description of hadronic interactions with the two different materials and also the geometric description of each.

The technique discussed in Section 8.2.3 for selecting MIPs in the electromagnetic calorimeter is also useful in studying deposits in the hadronic calorimeter. Those MIPs deposit almost all of their energy exclusively in the hadronic calorimeter. Figure 47 shows $\langle E/p \rangle_{\text{RAW}}^{\text{Had}}$, where RAW indicates that no correction has been applied for neutral backgrounds and Had indicates that only clusters for the hadronic calorimeter are included. The RAW and COR versions of $\langle E/p \rangle$ in this case are the same, as the neutral background is negligible in that calorimeter layer. The distributions are shown both for the original EM scale calibration and after LCW calibration. The data and simulation agree very well in this comparison, except in the lowest momentum bin which has 5% discrepancy that has already been seen in similar measurements.

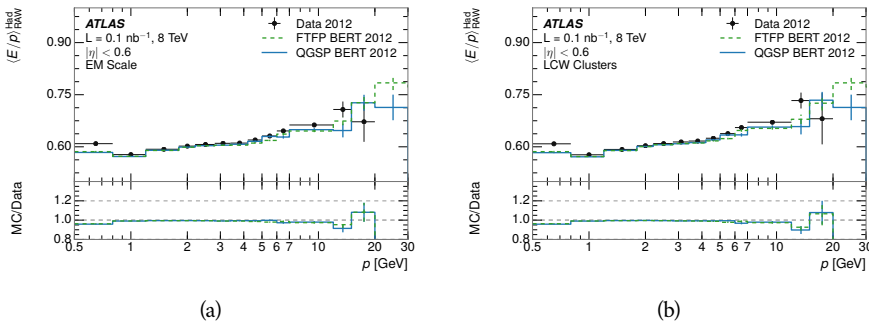


Figure 47: Comparison of the response of the hadronic calorimeter as a function of track momentum (a) at the EM-scale and (b) after the LCW calibration.

A similar comparison can be made in the electromagnetic calorimeter by selecting particles which have no associated energy in the hadronic calorimeter. These results are measured in terms of $\langle E/p \rangle_{\text{COR}}^{\text{EM}}$, where EM designates that only clusters in the electromagnetic calorimeter are included and COR designates that the neutral background is subtracted as the neutral background is present in this case. Figure 48 shows the analogous comparisons to Figure 47 in

2096 the electromagnetic calorimeter. In this case the disagreement between data and
 2097 simulation is more pronounced, with discrepancies as high as 5% over a larger
 2098 range of momenta. This level of discrepancy indicates that the description of
 2099 the electromagnetic calorimeter is actually the dominant source of discrepancy
 2100 in the combined distributions in Section 8.2.4.

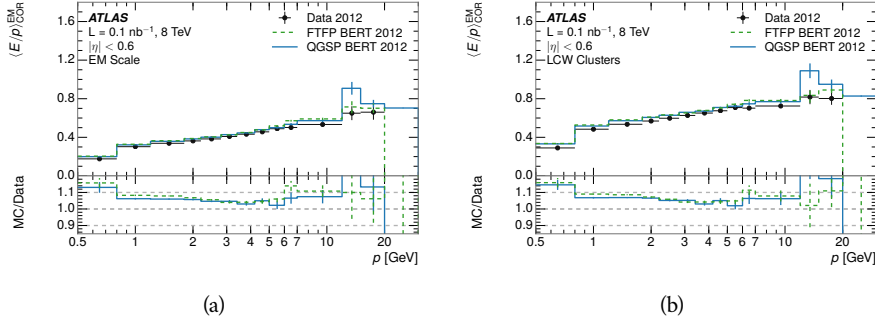


Figure 48: Comparison of the response of the EM calorimeter as a function of track momentum (a) at the EM-scale and (b) with the LCW calibration.

2101 **NOTE: There are more studies that I skipped for brevity that could be in-**
 2102 **cluded if interesting. E/p at different cluster threshold settings, E/p with**
 2103 **pileup, E/p with cells. I also left out a lot of eta bins that appear in the**
 2104 **paper so that this section didn't turn into 20 pages of plots.**

2105 8.3 IDENTIFIED PARTICLE RESPONSE

2106 The inclusive response measurement for hadrons can be augmented by measur-
 2107 ing the response for specific particle species. The simulation models each parti-
 2108 cle type separately, and understanding the properties of each is important in con-
 2109 straining the uncertainty on jets. In order to select and measure specific hadrons,
 2110 this section relies on the displaced decays of long-lived particles. Such decays
 2111 can be identified by reconstructing secondary vertices with a requirement on
 2112 mass. In particular, Λ , $\bar{\Lambda}$, and K_S^0 can be used to select a pure sample of protons,
 2113 antiprotons, and pions, respectively.

2114 8.3.1 DECAY RECONSTRUCTION

2115 The measurement of response for identified particles uses the same selection as
 2116 for inclusive particles (Section 8.1.3) with a few additions. Each event used is
 2117 required to have at least one secondary vertex, and the tracks are required to
 2118 match to that vertex rather than the primary vertex. Pions are selected from
 2119 decays of $K_S^0 \rightarrow \pi^+ \pi^-$, which is the dominant decay for K_S^0 to charged particles.
 2120 Protons are selected from decays of $\Lambda \rightarrow \pi^- p$ and antiprotons from $\bar{\Lambda} \rightarrow \pi^+ \bar{p}$,
 2121 which are similarly the dominant decays of Λ and $\bar{\Lambda}$ to charged particles. The
 2122 species of parent hadron in these decays is determined by reconstructing the
 2123 mass of the tracks associated to the secondary vertex. The sign of the higher

momentum decay particle can distinguish between Λ and $\bar{\Lambda}$, which of course have the same mass, as the proton or antiproton is kinematically favored to have higher momentum. Examples of the reconstructed masses used to select these decays are shown in Figure 49.

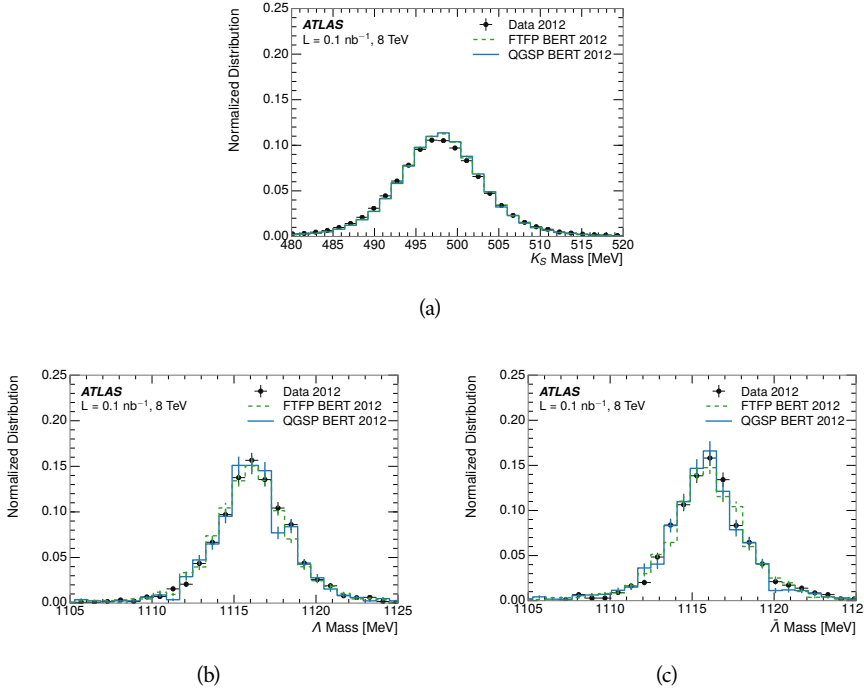


Figure 49: The reconstructed mass peaks of (a) K_S^0 , (b) Λ , and (c) $\bar{\Lambda}$ candidates.

The dominant backgrounds for the identified particle decays are nuclear interactions and combinatoric sources. These are suppressed by the kinematic requirements on the tracks as well as an additional veto which removes candidates that are consistent with both a Λ or $\bar{\Lambda}$ and a K_S^0 hypothesis, which is possible because of the different assumptions on particle mass in each case [19]. After these requirements, the backgrounds are found to be negligible compared to the statistical errors on these measurements.

8.3.2 IDENTIFIED RESPONSE

With these techniques the E/p distributions are extracted in data and simulation for each particle species and shown in Figure 50. These distributions are shown for a particular bin of E_a ($2.2 < E_a/\text{GeV} < 2.8$), rather than p . E_a is the energy available to be deposited in the calorimeter: for pions $E_a = \sqrt{p^2 + m^2}$, for protons $E_a = \sqrt{p^2 + m^2} - m$, and for antiprotons $E_a = \sqrt{p^2 + m^2} + m$. The features of the E/p distributions are similar to the inclusive case. There is a small negative tail from noise and a large fraction of tracks with zero energy from particles which do not reach the calorimeter. The long positive tail is noticeably more pronounced for antiprotons because of the additional energy generated by the annihilation in addition to the neutral background.

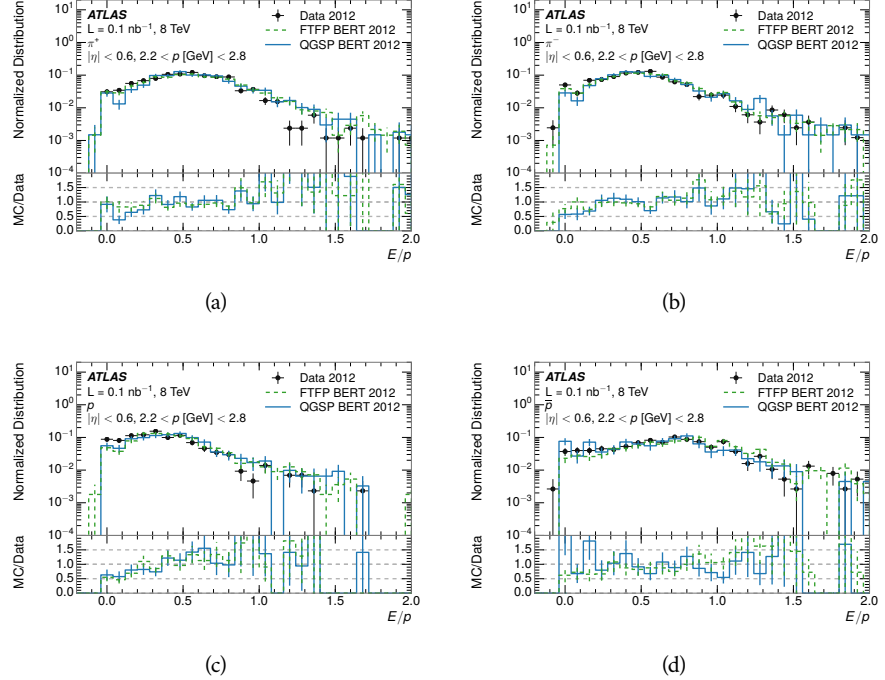


Figure 50: The E/p distribution for isolated (a) π^+ , (b) π^- , (c) proton, and (d) anti-proton tracks.

The zero fraction is further explored in Figure 51 for pions and protons in data and simulation. The simulation consistently underestimates the zero fraction independent of particle species, which implies that this discrepancy is not caused by the model of a particular species but rather a feature common to all.

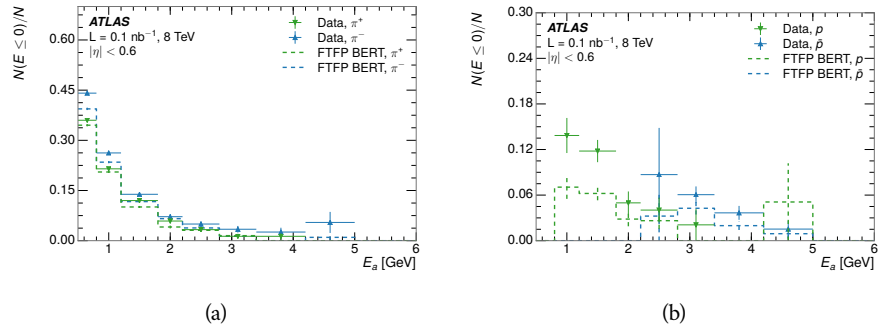


Figure 51: The fraction of tracks with $E \leq 0$ for identified (a) π^+ and π^- , and (b) proton and anti-proton tracks

It is also interesting to compare the response between the different particle species. One approach to do this is to measure the difference in $\langle E/p \rangle$ between two types, which has the advantage of removing the neutral background. These differences are shown in various combinations in Figure 52. The response for π^+ is greater on average than the response to π^- because of a charge-exchange effect which causes the production of additional neutral pions in the showers of

2156 π^+ [41]. The response for π^+ is also greater on average than the response to p ,
 2157 because a large fraction of the energy of π^+ hadrons is converted to an electro-
 2158 magnetic shower [42, 43]. However, the \bar{p} response is significantly higher than
 2159 the response to π^- because of the annihilation of the antiproton. FTFP_BERT
 2160 does a better job of modeling this effect than QGSP_BERT because of their differ-
 2161 ent descriptions of \bar{p} interactions with material.

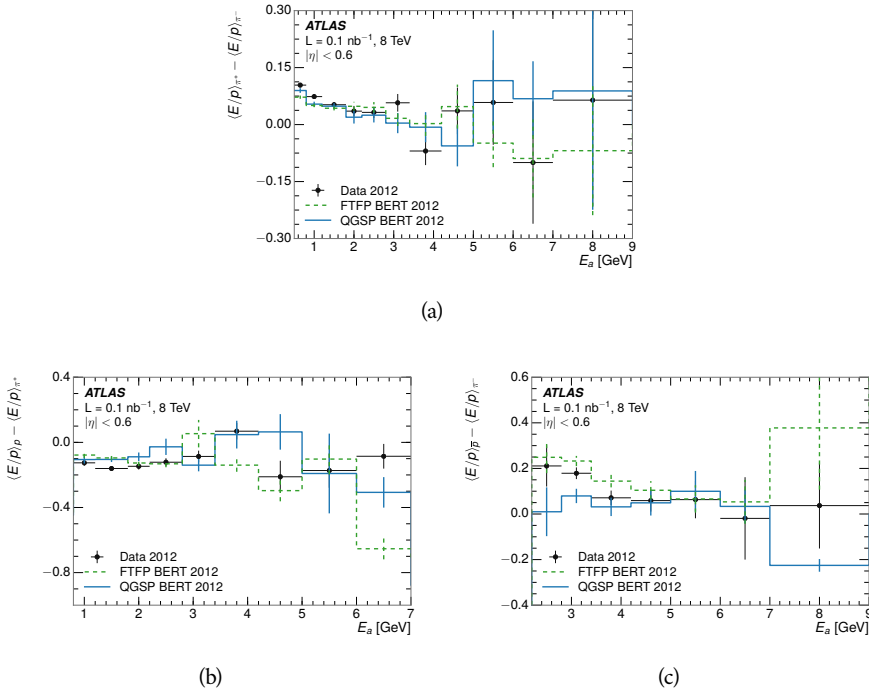


Figure 52: The difference in $\langle E/p \rangle$ between (a) π^+ and π^- (b) p and π^+ , and (c) \bar{p} and π^- .

2162 It is also possible to remove the neutral background from these response dis-
 2163 tributions using the same technique as in Section 8.2.3. The technique is largely
 2164 independent of the particle species and so can be directly applied to $\langle E/p \rangle$ for
 2165 pions. The $\langle E/p \rangle_{\text{COR}}$ distributions for pions are shown in Figure 53, which are
 2166 very similar to the inclusive results. The inclusive hadrons are comprised mostly
 2167 of pions, so this similarity is not surprising. It is also possible to see the small
 2168 differences between π^+ and π^- response here, where $\langle E/p \rangle_{\text{COR}}$ is higher on av-
 2169 erage for π^+ . The agreement between data and simulation is significantly worse
 2170 for the π^- distributions than for the π^+ , with a discrepancy greater than 10%
 2171 below 2-3 GeV.

2172 8.3.3 ADDITIONAL SPECIES IN SIMULATION

2173 The techniques above provide a method to measure the response separately for
 2174 only pions and protons. However the hadrons which forms jets include a num-
 2175 ber of additional species such as kaons and neutrons. The charged kaons are
 2176 an important component of the inclusive charged hadron distribution, which is
 2177 comprised of roughly 60-70% pions, 15-20% kaons, and 5-15% protons. These

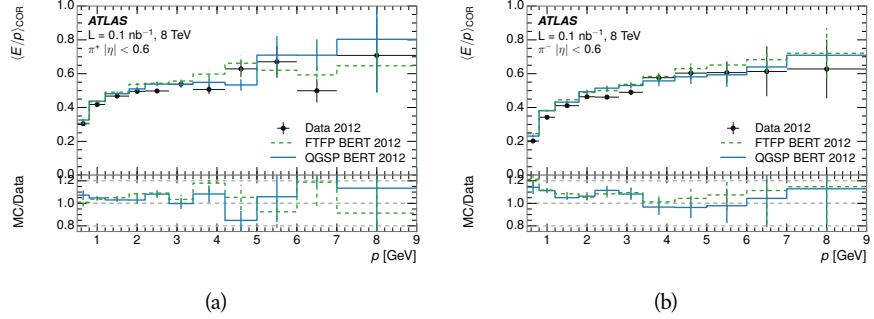


Figure 53: $\langle E/p \rangle_{\text{COR}}$ as a function of track momentum for (a) π^+ tracks and (b) π^- tracks.

2178 are difficult to measure in data at the ATLAS detector, although a template sub-
 2179 traction technique has been proposed which may be effective with larger sample
 2180 sizes [18]. The simulation of these particles includes noticeable differences in
 2181 response at low energies, which are shown in Figure 54 for FTFP_BERT. The
 2182 significant differences in response between low energy protons and antiprotons
 2183 are accounted for above in the definitions of E_a .

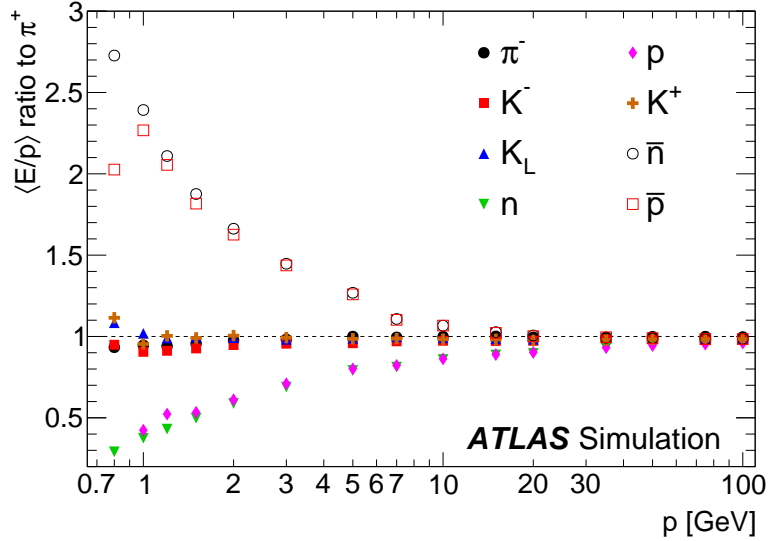


Figure 54: The ratio of the calorimeter response to single particles of various species to the calorimeter response to π^+ with the physics list FTFP_BERT.

2184 8.4 SUMMARY

2185 These various measurements of calorimeter response shown above for data and
 2186 simulation illuminate the accuracy of the simulation of hadronic interactions at
 2187 the ATLAS detector. The results were done using 2010 and 2012 data at 7 and 8
 2188 TeV, but reflect the most current understanding of the detector alignment and
 2189 geometry. A number of measurements focusing on a comparison between pro-

2190 tons and antiprotons suggest that FTFP_BERT models those interaction more
2191 accurately than QGSP_BERT. These measurements, among others, were the moti-
2192 vation to switch the default Geant4 simulation from FTFP_BERT to QGSP_BERT
2193 for all ATLAS samples.

2194 Even with these updates, there are a number of small, approximately 5%, dis-
2195 crepancies in response between the data and simulation at low energies. At
2196 higher energies the simulation of hadronic interactions is very consistent with
2197 data. Chapter 9 discusses how to use these observed differences to constrain the
2198 jet energy scale and its associated uncertainties.

2199

2200 JET ENERGY RESPONSE AND UNCERTAINTY

2201 9.1 MOTIVATION

2202 As jets form a major component of many physics analyses at ATLAS, it is crucial
 2203 to carefully calibrate the measurement of jet energies and to derive an uncer-
 2204 tainty on that measurement. These uncertainties have often been the dominant
 2205 systematic uncertainty in high-energy analyses at the LHC. Dijet and multijet
 2206 balance techniques provide a method to constrain the JES and its uncertainty in
 2207 data, and provide the default values used for ATLAS jet measurements at most
 2208 energies [44]. These techniques are limited by their reliance on measuring jets
 2209 in data, so they are statistically limited in estimating the jet energy scale at the
 2210 highest jet energies. This chapter presents another method for estimating the jet
 2211 energy scale and its uncertainty which builds up a jet from its components and
 2212 thus can be naturally extended to high jet momentum. Throughout this chapter
 2213 the jets studied are simulated using Pythia8 with the CT10 parton distribution
 2214 set [45] and the AU2 tune [22], and corrections are taken from the studies includ-
 2215 ing data and simulation in Chapter 8.

2216 As described in Section 7.4, jets are formed from topological clusters of energy
 2217 in the calorimeters using the anti- k_t algorithm. These clusters originate from a
 2218 diverse spectrum of particles, in terms of both species and momentum, leading to
 2219 significantly varied jet properties and response between jets of similar produced
 2220 momentum. Figure 55 shows the simulated distribution of particles within jets
 2221 at a few examples energies. The E/p measurements provide a thorough under-
 2222 standing of the dominant particle content of jets, the charged hadrons.

2223 9.2 UNCERTAINTY ESTIMATE

2224 Simulated jets are not necessarily expected to correctly model the energy de-
 2225 posits in the calorimeters, because of the various discrepancies discussed in Chap-
 2226 ter 8. To evaluate a jet energy response, the simulated jet energies are compared
 2227 to a corrected jet built up at the particle level. Each cluster in a jet is associated
 2228 to the truth particle which deposited it, and the energy in that cluster is then
 2229 corrected for a number of effects based on measurements in data. The primary
 2230 corrections come from the single hadron response measurements in addition to
 2231 response measured using the combined test beam which covers higher momen-
 2232 tum particles [46]. These corrections include both a shift (Δ), in order to make
 2233 the simulation match the average response in data, and an uncertainty (σ) asso-
 2234 ciated with the ability to constrain the difference between data and simulation.
 2235 Some of the dominant sources of uncertainty are itemized in Table 7 with typi-
 2236 cal values, and the full list considered is described in detail in the associated pa-

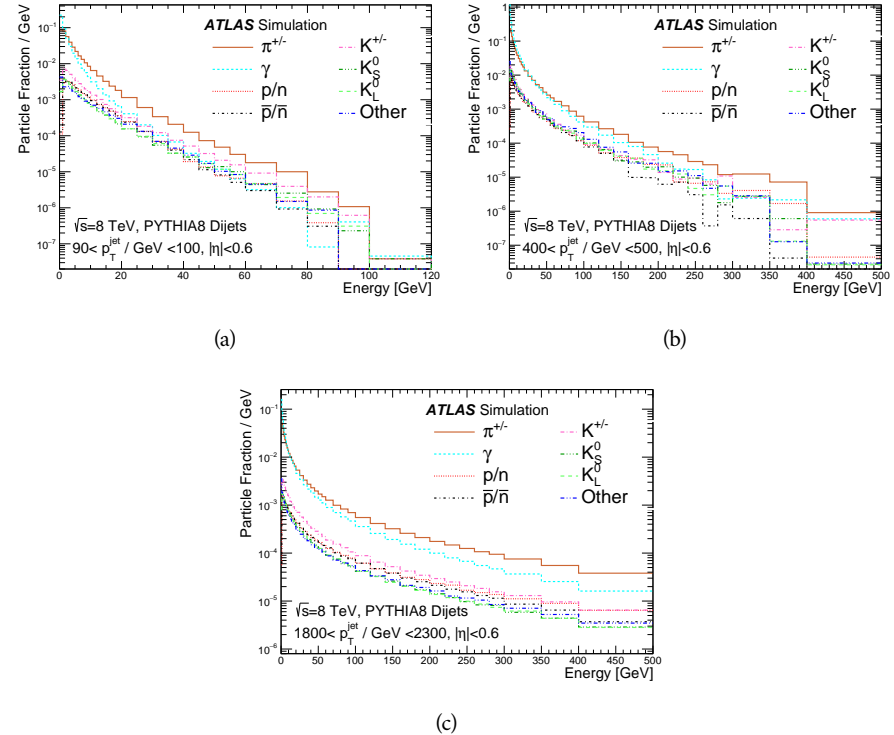


Figure 55: The spectra of true particles inside anti- k_t , $R = 0.4$ jets with (a) $90 < p_T/\text{GeV} < 100$, (b) $400 < p_T/\text{GeV} < 500$, and (c) $1800 < p_T/\text{GeV} < 2300$.

2237 per [18]. These uncertainties cover differences between the data and simulation
 2238 in the modeling of calorimeter response to a given particle. No uncertainties are
 2239 added for the difference between particle composition of jets in data and simu-
 2240 lation.

2241 From these terms, the jet energy scale and uncertainty is built up from indi-
 2242 vidual energy deposits in simulation. Each uncertainty term is treated indepen-
 2243 dently, and are taken to be gaussian distributed. The resulting scale and uncer-
 2244 tainty is shown in Figure 56, where the mean response is measured relative to
 2245 the calibrated energy reported by simulation. The dominant uncertainties come
 2246 from the statistical uncertainties on the E/p measurements at lower energies and
 2247 the additional uncertainty for out of range measurements at higher energies. The
 2248 total uncertainty from this method at intermediate jet energies is comparable to
 2249 other simulation-based methods [47] and is about twice as large as in-situ meth-
 2250 ods using data [44]. This method is the only one which provides an estimation
 2251 above 1.8 TeV, however, and so is still a crucial technique in analyses that search
 2252 for very energetic jets.

2253 These techniques can also be used to measure the correlation between bins of
 2254 average reconstructed jet momentum across a range of p_T and $|\eta|$, where cor-
 2255 relations are expected because of a similarity in particle composition at similar
 2256 energies. Figure 57 shows these correlations, where the uncertainties on jets in
 2257 neighboring bins are typically between 30% and 60% correlated. The uncertainty
 2258 on all jets becomes significantly correlated at high energies and larger pseudora-

Abbrev.	Description	Δ (%)	σ (%)
In situ E/p	The comparison of $\langle E/p \rangle_{\text{COR}}$ as described in Chapter 8 with statistical uncertainties from 500 MeV to 20 GeV.	0-3	1-5
CTB	The main $\langle E/p \rangle$ comparison uncertainties, binned in p and $ \eta $, as derived from the combined test beam results, from 20 to 350 GeV [46].	0-3	1-5
E/p Zero Fraction	The difference in the zero-fraction between data and MC simulation from 500 MeV to 20 GeV.	5-25	1-5
E/p Threshold	The uncertainty in the EM calorimeter response from the potential mismodeling of threshold effects in topological clustering.	0	0-10
Neutral	The uncertainty in the calorimeter response to neutral hadrons based on studies of physics model variations.	0	5-10
K_L	An additional uncertainty in the response to neutral K_L in the calorimeter based on studies of physics model variations.	0	20
E/p Misalignment	The uncertainty in the p measurement from misalignment of the ID.	0	1
Hadrons, $p > 350$ GeV	A flat uncertainty for all particles above the energy range or outside the longitudinal range probed with the combined test beam.	0	10

Table 7: The dominant sources of corrections and systematic uncertainties in the [JES](#) estimation technique, including typical values for the correcting shift (Δ) and the associated uncertainty (σ).

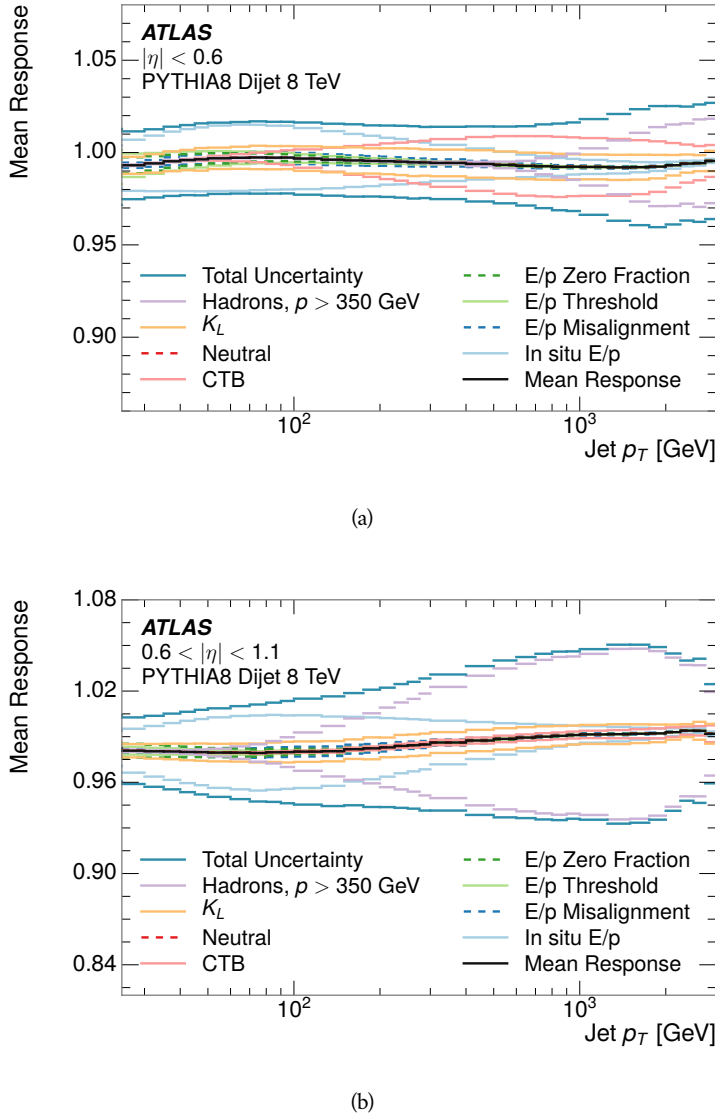


Figure 56: The [JES](#) uncertainty contributions, as well as the total [JES](#) uncertainty, as a function of jet p_T for (a) $|\eta| < 0.6$ and (b) $0.6 < |\eta| < 1.1$.

2259 pidiaries, when the uncertainty becomes dominated by the single term reflecting
 2260 out of range particles.

2261 9.3 SUMMARY

2262 The technique described above provides a jet energy scale and uncertainty by
 2263 building up jet corrections from the energy deposits of constituent particles. The
 2264 E/p measurements are crucial in providing corrections for the majority of parti-
 2265 cles in the jets. The uncertainty derived this way is between 2 and 5% and is about
 2266 twice as large at corresponding momentum than jet balance methods. However
 2267 this is the only uncertainty available for very energetic jets using 2012 data and
 2268 simulation, and repeating this method with Run 2 data and simulation will be

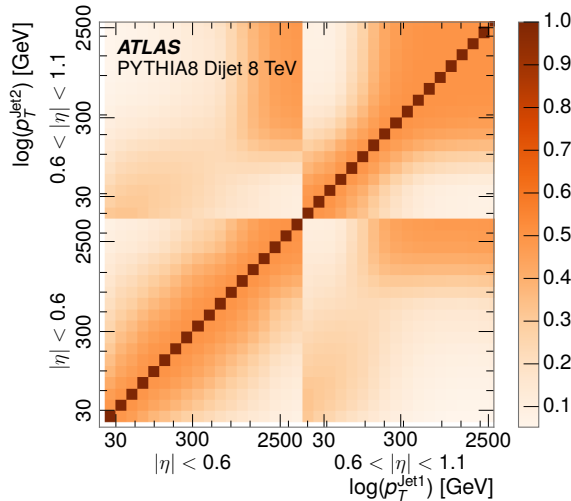


Figure 57: The **JES** correlations as a function of jet p_T and $|\eta|$ for jets in the central region of the detector.

2269 important in providing an uncertainty for the most energetic jets in 13 TeV col-
 2270 lisions.

2271

PART V

2272

SEARCH FOR LONG-LIVED PARTICLES

2273

You can put some informational part preamble text here.

2274

2275 LONG-LIVED PARTICLES IN ATLAS

2276 As discussed in Section 2.3, various limitations in the SM suggest a need for new
 2277 particles at the TeV scale. A wide range of extensions to the Standard Model
 2278 predict that these new particles can have lifetimes greater than approximately
 2279 one-hundredth of a nanosecond. These include theories with universal extra-
 2280 dimensions [48, 49], with new fermions [50], and with leptoquarks [51]. Many
 2281 SUSY theories also produce these Long-Lived Particles (LLPs), in both R-Parity
 2282 violating [52–54] and R-Parity conserving [55–58] formulations. Split super-
 2283 symmetry [59, 60], for example, predicts long-lived gluinos with O(TeV) masses.
 2284 This search focuses specifically on the SUSY case, but many of the results are
 2285 generic to any model with LLPs.

2286 Long-lived gluinos or squarks carry color-charge and will thus hadronize into
 2287 color neutral bound states called R-Hadrons. These are composit particles like
 2288 the usual hadrons but with one supersymmetric constituent, for example $\tilde{g}q\bar{q}$
 2289 and $\tilde{q}\bar{q}$. Through this hadronization process, the neutral gluino can acquire a
 2290 charge. Gluino pair production, $pp \rightarrow \tilde{g}\tilde{g}$ has the largest cross sectional increase
 2291 with the increase in energy to 13 TeV, and so this search focuses on gluino R-
 2292 Hadrons. Planned future updates will extend the case to explicitly include squark
 2293 and chargino models, but the method covers any long-lived, charged, massive
 2294 particle.

2295 10.1 EVENT TOPOLOGY

2296 The majority of SUSY models predict that gluinos will be produced in pairs at
 2297 the LHC, through processes like $pp \rightarrow q\bar{q} \rightarrow \tilde{g}\tilde{g}$ and $pp \rightarrow gg \rightarrow \tilde{g}\tilde{g}$, where the
 2298 gluon mode dominates for the collision energy and gluino masses considered
 2299 for this search. During their production, the long-lived gluinos hadronize into
 2300 color singlet bound states including $\tilde{g}q\bar{q}$, $\tilde{g}qqq$, and even $\tilde{g}g$ [61]. The probability
 2301 to form the gluon-only bound states is a free parameter usually taken to be 0.1,
 2302 while the meson states are favored among the R-Hadrons [62]. The charged and
 2303 neutral states are approximately equally likely for mesons, so the R-Hadrons will
 2304 be charged roughly 50% of the time.

2305 These channels produce R-Hadrons with large p_T , comparable to their mass,
 2306 so that they typically propagate with $0.2 < \beta < 0.9$ [62]. The fragmentation that
 2307 produces these hadrons is very hard, so the jet structure around the R-Hadron
 2308 is minimal, with less than 5 GeV of summed particle momentum expected in a
 2309 cone of $\Delta R < 0.25$ around the R-Hadron [62]. After hadronization, depending
 2310 on the gluino lifetime, the R-Hadrons then decay into hadrons and a LSP [61].

2311 In summary, the expected event for pair-produced long-lived gluinos is very
 2312 simple: two isolated, high-momentum R-Hadrons that propagate through the
 2313 detector before decaying into jets. The observable features of such events depend

2314 strongly on the interaction of the R-Hadron with the material of the detector and
 2315 also its lifetime. Section 10.1.1 describes the interactions of R-Hadrons which
 2316 reach the various detector elements in ATLAS and Section 10.1.2 provides a sum-
 2317 mary of the observable event descriptions for R-Hadrons of various lifetimes.

2318 10.11 DETECTOR INTERACTIONS

2319 After approximately 0.2 ns, the R-Hadron reaches the pixel detector. If charged,
 2320 it deposits energy into the material through repeated single collisions that result
 2321 in ionization of the silicon substrate [7]. Because of its comparatively low β , the
 2322 ionization energy can be significantly greater than expected for SM particles be-
 2323 cause the most-probable energy loss grows significantly as β decreases [7]. This
 2324 large ionization can be measured through the ToT read out from the pixel detec-
 2325 tor as described in Section 7.1.2. Large ionization in the inner detector is one of
 2326 the major characteristic features of LLPs.

2327 Throughout the next few nanoseconds, the R-Hadron propagates through the
 2328 remainder of the inner detector. A charged R-Hadron will provide hits in each
 2329 of these systems as would any other charged particle, and can be reconstructed
 2330 as a track. The track reconstruction provides a measurement of its trajectory
 2331 and thus its momentum as described in Section 7.1. The large momentum is
 2332 another characteristic feature of massive particles produced at the LHC. **Note: At**
 2333 **this point I am failing to mention that the TRT provides a possible dE/dx**
 2334 **measurement, because no one uses it as far as I know.**

2335 As of roughly 20 ns, the R-Hadron enters the calorimeter where it interacts
 2336 hadronically with the material. Because of its large mass and momentum, the
 2337 R-Hadron does not typically stop in the calorimeter, but rather deposits a small
 2338 fraction of its energy through repeated interactions with nucleons. The proba-
 2339 bility of interaction between the gluino itself and a nucleon is low because the
 2340 cross section drops off with the inverse square of its mass, so the interactions are
 2341 primarily governed by the light constituents [63]. Each of these interactions can
 2342 potentially change that quark content and thus change the sign of the R-Hadron,
 2343 so that the charge at exit is typically uncorrelated with the charge at entry [62].
 2344 The total energy deposited in the calorimeters during the propagation is small
 2345 compared to the kinetic energy of the R-Hadron, around 20-40 GeV, so that
 2346 E/p is typically less than 0.1 [62].

2347 Then, 30 ns after the collision, it reaches the muon system, where it again
 2348 ionizes in the material if charged and can be reconstructed as a muon track. Be-
 2349 cause of the charge-flipping interactions in the calorimeter, this track may have
 2350 the opposite sign of the track reconstructed in the inner detector, or there may
 2351 be a track present when there was none in the inner detector and vice-versa. The
 2352 propagation time at the typically lower β results in a significant delay compared
 2353 to muons, and that delay can be assessed in terms of a time-of-flight measure-
 2354 ment. Because of the probability of charge-flip and late arrival, there is a signif-
 2355 icant chance that an R-Hadron which was produced with a charge will not be
 2356 identified as a muon. The long time-of-flight is another characteristic feature of
 2357 R-Hadrons which are reconstructed as muons.

2358 10.1.2 LIFETIME DEPENDENCE

2359 The above description assumed a lifetime long enough for the R-Hadron to exit
 2360 the detector, which through this search is referred to as “stable”, even though
 2361 the particle may decay after exiting the detector. There are several unique sig-
 2362 natures at shorter lifetimes where the R-Hadron decays in various parts of the
 2363 inner detector; these lifetimes are referred to as “metastable”.

2364 The shortest case where the R-Hadron is considered metastable is for life-
 2365 times around 0.01 ns, where the particle decays before reaching any of the de-
 2366 tector elements. Although the R-Hadrons are produced opposite each other in
 2367 the transverse plane, each R-Hadron decays to a jet and an [LSP](#). The [LSPs](#) are not
 2368 measured, so the produced jets can be significantly imbalanced in the transverse
 2369 plane which results in large missing energy. That missing energy can be used
 2370 to trigger candidate events, and provides the most efficient trigger option for
 2371 shorter lifetimes. Additionally, the precision of the tracking system allows the
 2372 displaced vertex of the R-Hadron decay to be reconstructed from the charged
 2373 particles in the jet. The distance of that vertex from the interaction point can
 2374 be used to distinguish R-Hadron decays from other processes. Figure 58 shows
 2375 a schematic diagram of an example R-Hadron event with such a lifetime. The
 2376 diagram is not to scale, but instead illustrates the detector interactions in the
 2377 pixel detector, calorimeters, and muon system. It includes a representation of
 2378 the charged R-Hadron and the neutral R-Hadron, as well as the [LSPs](#) and jets
 2379 (shown as charged hadrons) produced in the decay. Neutral hadrons may also
 2380 be produced in the decay but are not depicted. Previous searches on [ATLAS](#) have
 2381 used the displaced vertex to target [LLP](#) decays [64].

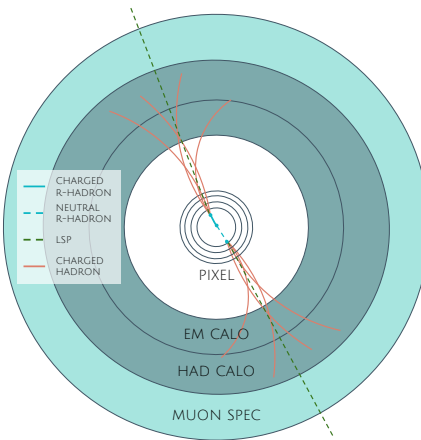


Figure 58: A schematic diagram of an R-Hadron event with a lifetime around 0.01 ns.
 The diagram includes one charged R-Hadron (solid blue), one neutral R-
 Hadron (dashed blue), [LSPs](#) (dashed green) and charged hadrons (solid orange).
 The pixel detector, calorimeters, and muon system are illustrated but not to
 scale.

2382 The next distinguishable case occurs at lifetimes greater than 0.1 ns, where
 2383 the R-Hadron forms a partial track in the inner detector. If the decay products
 2384 are sufficiently soft, they may not be reconstructed, and this forms a unique sig-

2385 nature of a disappearing track. An example of such an event is illustrated in
 2386 Figure 59, which shows the short track in the inner detector and the undetected
 2387 soft charged hadron and LSP that are produced. A dedicated search on ATLAS used
 2388 the disappearing track signature to search for LLP in Run 1 [65]. **zNote: might**
 2389 **not be worth mentioning the disappearing track here since it is actually a**
 2390 **chargino search, the soft pion is pretty unique to charginos.**

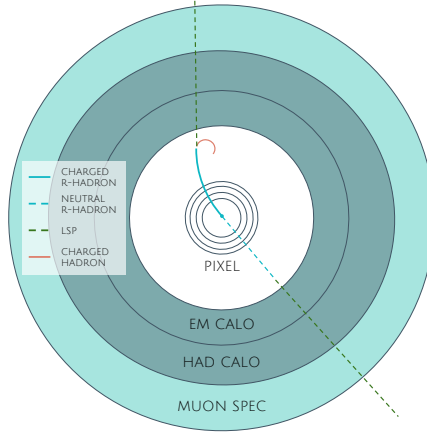


Figure 59: A schematic diagram of an R-Hadron event with a lifetime around 4 ns. The diagram includes one charged R-Hadron (solid blue), one neutral R-Hadron (dashed blue), LSPs (dashed green) and a charged hadron (solid orange). The pixel detector, calorimeters, and muon system are illustrated but not to scale.

2391 If the decay products are not soft, the R-Hadron daughters form jets, resulting
 2392 in an event-level signature of up to two high-momentum tracks, jets, and signif-
 2393 icant missing energy. The missing energy has the same origin as in the case of
 2394 0.01 ns lifetimes, from the decay to unmeasured particles, and again can be large.
 2395 The high-momentum tracks will also have the characteristically high-ionization
 2396 of massive, long-lived particles in the inner detector. Figure 60 illustrates an ex-
 2397 ample event with one charged R-Hadron which decays after approximately 10 ns,
 2398 and shows how the jets from the decay can still be reconstructed in the calorime-
 2399 ter. Several previous searches on ATLAS from Run 1 have used this signature to
 2400 search for R-Hadrons [66, 67], including a dedicated search for metastable parti-
 2401 cles [68].

2402 If the lifetime is longer than several nanoseconds, in the range of 15-30 ns,
 2403 the R-Hadron decay can occur in or after the calorimeters, but prior to reaching
 2404 the muon system. This case is similar to the above, although the jets may not be
 2405 reconstructed, and is covered by many of the same search strategies. The events
 2406 still often have large missing energy, although it is generated through different
 2407 mechanisms. The R-Hadrons do not deposit much energy in the calorimeters, so
 2408 a neutral R-Hadron will not enter into the missing energy calculation. A charged
 2409 R-Hadron opposite a neutral R-Hadron will thus generate significant missing en-
 2410 ergy, and close to 50% of pair-produced R-Hadron events fall into this category.
 2411 If both R-Hadrons are neutral then the missing energy will be low because nei-
 2412 ther is detected. Two charged R-Hadrons will also result in low missing energy
 2413 because both are reconstructed as tracks and will balance each other in the trans-

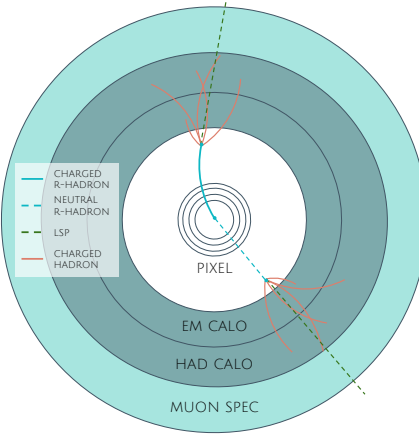


Figure 60: A schematic diagram of an R-Hadron event with a lifetime around 5 ns. The diagram includes one charged R-Hadron (solid blue), one neutral R-Hadron (dashed blue), LSPs (dashed green) and charged hadrons (solid orange). The pixel detector, calorimeters, and muon system are illustrated but not to scale.

verse plane. A small fraction of the time, one of the charged R-Hadron tracks may fail quality requirements and thus be excluded from the missing energy calculation and again result in significant missing energy. Figure 61 illustrates another example event with one charged R-Hadron which decays after approximately 20 ns, and shows how the jets from the decay might not be reconstructed.

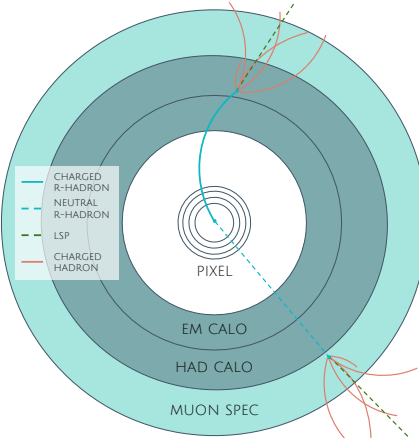


Figure 61: A schematic diagram of an R-Hadron event with a lifetime around 20 ns. The diagram includes one charged R-Hadron (solid blue), one neutral R-Hadron (dashed blue), LSPs (dashed green) and charged hadrons (solid orange). The pixel detector, calorimeters, and muon system are illustrated but not to scale.

The longest lifetimes, the stable case, has all of the features of the 30-50 ns case but with the addition of muon tracks for any R-Hadrons that exit the calorimeter with a charge. That muon track can provide additional information from time-of-flight measurements to help identify LSPs. An example of the event topology for one charged and one neutral stable R-Hadron is shown in Figure 62. Some searches on ATLAS have included this information to improve the search reach for stable particles [67, 69].

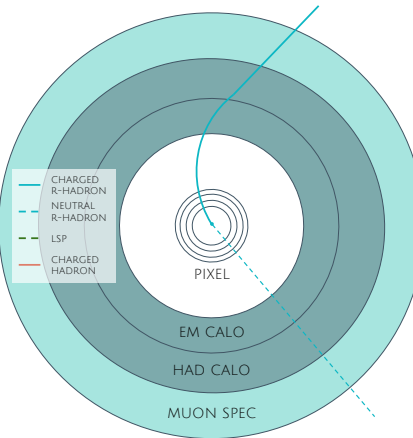


Figure 62: A schematic diagram of an R-Hadron event with a lifetime around 20 ns. The diagram includes one charged R-Hadron (solid blue) and one neutral R-Hadron (dashed blue). The pixel detector, calorimeters, and muon system are illustrated but not to scale.

2426 10.2 SIMULATION

2427 All of the event topologies discussed above are explored by simulations of R-
 2428 Hadron events in the [ATLAS](#) detector. A large number of such samples are gen-
 2429 erated to determine signal efficiencies, to measure expected yields, and to esti-
 2430 mate uncertainties. The primary interaction, pair production of gluinos with
 2431 masses between 400 and 3000 GeV, is simulated using [Pythia 6.4.27](#) [70]
 2432 with the AUET2B [71] set of tuned parameters for the underlying event and
 2433 the CTEQ6L1 [45] parton distribution function ([PDF](#)) set. The simulated inter-
 2434 actions include a modeling of pileup by adding secondary, minimum bias in-
 2435 teractions from both the same (in-time pileup) and nearby (out-of-time pileup)
 2436 bunch crossings. This event generation is then augmented with a dedicated
 2437 hadronization routine to hadronize the long-lived gluinos into final states with
 2438 R-Hadrons [72], with the probability to form a gluon-gluino bound set at 10% [73].

2439 The cross sections used for these processes are calculated at next-to-leading
 2440 order ([NLO](#)) in the strong coupling constant with a resummation of soft-gluon
 2441 emmission at next-to-leading logarithmic ([NLL](#)) [74–78]. The nominal predic-
 2442 tions and the uncertainties for each mass point are taken from an envelope of
 2443 cross-section predictions using different [PDF](#) sets and factorization and renor-
 2444 malization scales [79].

2445 The R-Hadrons then undergo a full detector simulation [], where the interac-
 2446 tions of the R-Hadrons with the material of the detector are described by dedi-
 2447 cated [Geant4](#) [15] routines. These routines model the interactions described in
 2448 Section 10.1.1, including the ionizing interactions in the silicon modules of the
 2449 inner detector and the R-Hadron-nucleon interactions in the calorimeters [80,
 2450 81]. The specific routine chosen to describe the interactions of the R-Hadrons
 2451 with nucleons, the “generic model”, uses a pragmatic approach where the scatter-
 2452 ing cross section is taken to be a constant 12 mb per light quark. In this model

2453 the gluino itself does not interact at all except through its role as a reservoir of
 2454 kinetic energy.

2455 The lifetimes of these R-Hadrons are then simulated at several working points,
 2456 $\tau = 0.1, 1.0, 3.0, 10, 30, 50$ and detector stable, where the particle is required to
 2457 decay after propagating for a time compatible with its lifetime. Only one decay
 2458 mode is simulated for these samples, $\tilde{g} \rightarrow q\bar{q}\tilde{\chi}_1^0$ with the neutralino mass set to
 2459 100 GeV, which is chosen because it has the highest sensitivity among all of the
 2460 modes studied in previous searches [68]. Heavier neutralinos have similar results
 2461 but generate less missing energy which reduces the efficiency of triggering.

2462 All of the simulated events are then reconstructed using the same software
 2463 used for collision data. The fully reconstructed events are then reweighted to
 2464 match the distribution of initial state radiation in an alternative sample of events,
 2465 generated with MG5_aMC@NLO [82], which has a more accurate description of ra-
 2466 diate effects than Pythia6. This reweighting provides a more accurate descrip-
 2467 tion of the momentum of the gluino-gluino system and is important in modeling
 2468 the efficiency of triggering and offline event selection.

2469

2470 EVENT SELECTION

2471 The [LLPs](#) targeted by this search differ in their interactions with the detector from
 2472 [SM](#) particles primarily because of their large mass. When produced at the energies
 2473 available at the [LHC](#), that large mass results in a low β (typically $0.2 < \beta <$
 2474 0.9). Such slow-moving particles heavily ionize in detector material. Each layer
 2475 of the pixel detector provides a measurement of that ionization, through [ToT](#), as
 2476 discussed in Section 7.1.2. The ionization in the pixel detector, quantified in
 2477 terms of dE/dx , provides the major focus for this search technique, along with
 2478 the momentum measured in the entire inner detector. It is effective both for its
 2479 discriminating power and its use in reconstructing a particle's mass, and it can
 2480 be used for a wide range of masses and lifetimes as discussed in Section 10.1.2.
 2481 However dE/dx needs to be augmented with a few additional selection requirements
 2482 to provide a mechanism for triggering and to further reduce backgrounds.

2483 Ionization itself is not currently accessible for triggering, so this search instead
 2484 relies on E_T^{miss} to trigger signal events. Although triggering on E_T^{miss} can
 2485 be inefficient, E_T^{miss} is often large for many production mechanisms of [LLPs](#), as
 2486 discussed in Section 10.1.

2487 The use of ionization to reject [SM](#) backgrounds relies on well-measured, high-
 2488 momentum tracks, so some basic requirements on quality and kinematics are
 2489 placed on the tracks considered in this search. These quality requirements have
 2490 been significantly enhanced in Run 2 by a newly introduced tracking variable
 2491 that is very effective in removing highly-ionizing backgrounds caused by over-
 2492 lapping tracks. A few additional requirements are placed on the tracks consid-
 2493 ered for [LLP](#) candidates that increase background rejection by targeting specific
 2494 types of [SM](#) particles. These techniques provide a significant analysis improve-
 2495 ment over previous iterations of ionization-based searches on ATLAS by provid-
 2496 ing additional background rejection with minimal loss in signal efficiency.

2497 The ionization measurement with the Pixel detector can be calibrated to pro-
 2498 vide an estimator of $\beta\gamma$. That estimate, together with the momentum measure-
 2499 ment provided by tracking, can be used to reconstruct a mass for each track
 2500 which traverses the pixel detector. That mass variable will be peaked at the [LLP](#)
 2501 mass for any signal, and provides an additional tool to search for an excess. In
 2502 addition to an explicit requirement on ionization, this search constructs a mass-
 2503 window for each targeted signal mass in order to evaluate any excess of events
 2504 and to set limits.

2505 The strategy discussed here is optimized for lifetimes of $O(1) - O(10)$ ns.
 2506 Pixel ionization is especially useful in this regime as particles only need to prop-
 2507 agate through the first seven layers of the inner detector, about 37 cm from the
 2508 beam axis. The search is still competitive with other searches for [LLPs](#) at longer
 2509 lifetimes, because the primary discriminating variables are still applicable even
 2510 for particles that do not decay within the detector [69]. Although the majority of

2511 the requirements will be the same for all lifetimes, two signal regions are defined
 2512 to optimize separately for intermediate and long lifetime particles.

2513 11.1 TRIGGER

2514 Triggering remains a significant difficulty in defining an event selection with
 2515 high signal efficiency in a search for LLPs. There are no triggers available in
 2516 the current ATLAS system that can fire directly from a high momentum track
 2517 with large ionization (Section 6.6). Although in some configurations a charged
 2518 LLP can fire muon triggers, this requirement introduces significant model depen-
 2519 dence on both the allowed lifetimes and the interactions in the calorimeter [62],
 2520 as discussed in Section 10.1.1.

2521 For a search targeting particles which may decay prior to reaching the muon
 2522 system, the most efficient available trigger is based on missing energy [62]. As
 2523 discussed in Section 10.1, signal events can produce significant E_T^{miss} by a few
 2524 mechanisms. At the trigger level however, the missing energy is only calculated
 2525 using the calorimeters (Section 6.6) where the R-Hadrons deposit little energy.
 2526 So, at short lifetimes, E_T^{miss} measured in the calorimeter is generated by an im-
 2527 balance between the jets and undetected LSPs produced in R-Hadron decays. At
 2528 longer lifetimes, without the decay products, missing energy is only produced in
 2529 the calorimeters when the R-Hadrons recoil against an initial state radiation (ISR)
 2530 jet.

2531 These features are highlighted in Figure 63, which shows the E_T^{miss} distribu-
 2532 tions for simulated short lifetime (3 ns) and stable R-Hadron events. The figure
 2533 includes both the offline E_T^{miss} , the missing energy calculated with all available
 2534 information, and Calorimeter E_T^{miss} , the missing energy calculated using only
 2535 information available at the calorimeter which approximates the missing energy
 2536 available at the trigger. The short lifetime sample has significantly greater E_T^{miss}
 2537 and Calorimeter E_T^{miss} than the stable sample as expected. For the stable sam-
 2538 ple, a small fraction of events with very large E_T^{miss} (about 5%) migrate into the
 2539 bin with very small Calorimeter E_T^{miss} because the E_T^{miss} produced by a charged
 2540 R-Hadron track opposite a neutral R-Hadron track does not contribute any miss-
 2541 ing energy in the calorimeters.

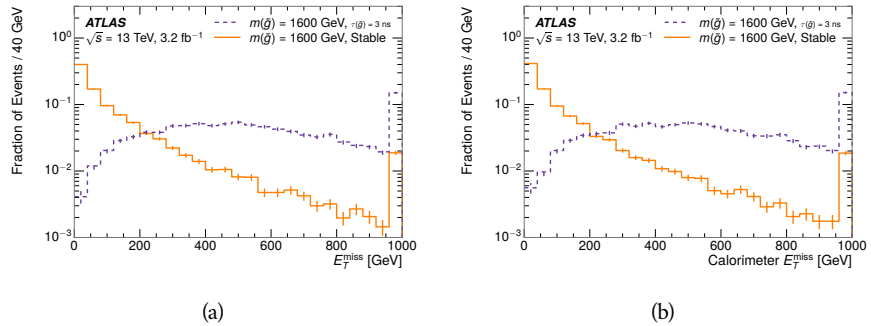


Figure 63: The distribution of (a) E_T^{miss} and (b) Calorimeter E_T^{miss} for simulated signal events before the trigger requirement.

2542 So, either case to some extent relies on kinematic degrees of freedom to pro-
 2543 duce missing energy, as the pair-produced LLPs tend to balance each other in
 2544 the transverse plain. That balance results in a relatively low efficiency for long-
 2545 lifetime particles, roughly 40%, and efficiencies between 65% and 95% for shorter
 2546 lifetimes depending on both the mass and the lifetime. For long lifetimes in par-
 2547 ticular, the presence of ISR is important in providing an imbalance in the trans-
 2548 verse plane, and is an important aspect of modeling the selection efficiency for
 2549 R-Hadron events.

2550 The missing energy trigger with the lowest threshold available is chosen for
 2551 this selection in order to maximize the trigger efficiency. During 2015 data col-
 2552 lection this was the HLT_xe70 trigger, which used a 50 GeV threshold on miss-
 2553 ing energy at LVL1 and a 70 GeV threshold on missing energy at the HLT. These
 2554 formation of the trigger decision for missing energy was discussed in more detail
 2555 in Section 6.6.

2556 11.2 KINEMATICS AND ISOLATION

2557 After the trigger requirement, each event is required to have a primary vertex
 2558 reconstructed from at least two well-measured tracks in the inner detector, each
 2559 with $p_T > 400$ MeV. If more than one such vertex exists, the primary vertex
 2560 is taken to be the one with the largest summed track momentum for all tracks
 2561 associated to that vertex. The offline reconstructed E_T^{miss} is required to be above
 2562 130 GeV to additionally reject SM backgrounds. The transverse missing energy
 2563 is calculated using fully reconstructed and calibrated offline objects, as described
 2564 in Section 7.5. In particular the E_T^{miss} definition in this selection uses jets recon-
 2565 structed with the anti- k_t algorithm with radius $R = 0.4$ from clusters of energy
 2566 in the calorimeter (Section 7.4) and with $p_T > 20$ GeV, as well as reconstructed
 2567 muons, electrons, and tracks not identified as another object type.

2568 The E_T^{miss} distributions are shown for data and a few simulated signals in Fig-
 2569 ure 64, after the trigger requirement. The cut placed at 130 GeV is 95% effi-
 2570 cient for metastable and 90% efficient for stable particles, after the trigger re-
 2571 quirement, because of the missing energy generating mechanisms discussed pre-
 2572 viously. The distribution of data in this figure and subsequent figures in this sec-
 2573 tion can be interpreted as the distribution of backgrounds, as any signal contam-
 2574 ination would be negligible if present at these early stages of the selection (prior
 2575 to the final requirement on ionization). The background falls rapidly with miss-
 2576 ing energy, motivating the direct requirement on E_T^{miss} for the signal region. Al-
 2577 though a tighter requirement than the specified value of 130 GeV would seem to
 2578 increase the search potential from these early distributions, other requirements
 2579 are more optimal when taken as a whole. The specific values for each require-
 2580 ment in signal region were optimized considering the increase in discovery reach
 2581 for tightening the requirement on each discriminating variable. **NOTE: If space**
 2582 **and time permit, I will add a whole section about signal region optimiza-**
 2583 **tion..**

2584 It is typically the practice for searches for new physics on ATLAS to place an
 2585 offline requirement on the triggering variable that is sufficiently tight to guar-

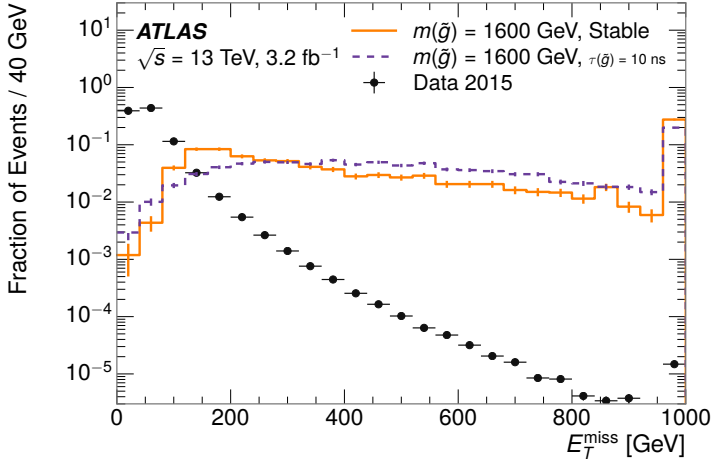


Figure 64: The distribution of E_T^{miss} for data and simulated signal events, after the trigger requirement.

2586 antee that the event would pass the trigger. Such a tight requirement makes the
 2587 uncertainty on the trigger efficiency of the simulation negligible, as modeling the
 2588 regime where the trigger is only partially efficient can be difficult. In this analy-
 2589 sis, however, because of the atypical interactions of R-Hadrons with the tracker
 2590 and the calorimeter, the offline requirement on E_T^{miss} is not sufficient to guar-
 2591 antee a 100% trigger efficiency even at large values, as can be seen in Figure 65.
 2592 This figure shows the efficiency for passing the HLT_xe70 trigger as a function
 2593 of the requirement on E_T^{miss} , which plateaus to roughly 85% even at large values.
 2594 This plateau does not reach 100% because events which have large offline miss-
 2595 ing energy from a neutral R-Hadron produced opposite of a charged R-Hadron
 2596 can have low missing energy in the calorimeters. The Calorimeter E_T^{miss} , on the
 2597 other hand, does not have this effect and reaches 100% efficiency at large values
 2598 because it is the quantity that directly corresponds to the trigger threshold. In
 2599 both cases the efficiency of triggering is greater for the short lifetime sample be-
 2600 cause the late decays to hadrons and LSPs produce an imbalance in the calorime-
 2601 ters even though they may not be reconstructed offline as tracks or jets. For this
 2602 reason, the requirement on E_T^{miss} is determined by optimizing the background
 2603 rejection even though it corresponds to a value of trigger efficiency significantly
 2604 below 1.0.

2605 Potential signal events are then required to have at least one candidate LLP
 2606 track. Although the LLPs are produced in pairs, many models do not consistently
 2607 yield two charged particles. For example, in the R-Hadron model highlighted
 2608 here, only 20% of events have two charged R-Hadrons while 47% of events have
 2609 just one. A signal region requiring two charged candidates could be a powerful
 2610 improvement in background rejection for a larger dataset, but it is not consid-
 2611 ered in this version of the analysis as it was found to be unnecessary to reject the
 2612 majority of backgrounds.

2613 For a track to be selected as a candidate, it must have $p_T > 50 \text{ GeV}$ and pass
 2614 basic quality requirements. The track must be associated to the primary vertex.

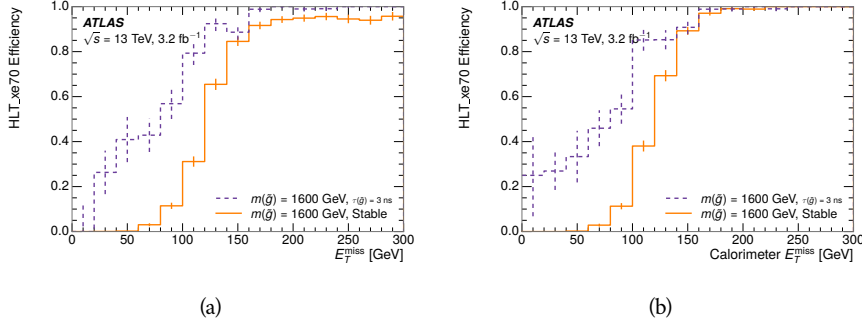


Figure 65: The trigger efficiency for the HLT_xe70 trigger requirement as a function of (a) E_T^{miss} and (b) Calorimeter E_T^{miss} for simulated signal events.

It must also have at least seven clusters in the silicon layers in the inner detector to ensure an accurate measurement of momentum. Those clusters must include one in the innermost layer if the extrapolated track is expected to pass through that layer. And to ensure a reliable measurement of ionization, the track is required to have at least two clusters in the pixel detector that provide a measurement of dE/dx .

At this point in the selection, there is a significant high-ionization background from multiple tracks that significantly overlap in the inner detector. Previous version of this analysis have rejected these overlaps by an explicit overlap rejection between pairs of fully reconstructed tracks, typically by requiring no additional tracks within a cone around the candidate. This technique, however, fails to remove the background from tracks that overlap so precisely that the tracks cannot be separately resolved, which can be produced in very collimated photon conversions or decays of pions.

A new method, added in Run 2, identifies cluster shapes that are likely formed by multiple particles based on a neural network classification algorithm. The number of clusters that are classified this way in the pixel detector for a given track is called N_{split} . As the shape of clusters requires significantly less spatial separation to identify overlaps than it does to reconstruct two fully resolved tracks, this variable is more effective at rejecting backgrounds from overlaps. Figure 66 shows the dependence of ionization on N_{split} ; as N_{split} increases the most probable value of dE/dx grows significantly up to twice the expected value when $N_{\text{split}} = 4$.

This requirement is very successful in reducing the long positive tail of the dE/dx distributions, as can be seen in Figure 67. Comparing the distribution for “baseline tracks”, tracks with only the above requirements on clusters applied and before the requirement on N_{split} , to the distribution with $N_{\text{split}} = 0$, it is clear that the fraction of tracks with large dE/dx is reduced be several orders of magnitude. The tracks without split hits are very close to the dE/dx distribution of identified muons, which are extremely well isolated on average. Figure 67 also includes the distribution of dE/dx in an example signal simulation to demonstrate how effective dE/dx is as a discriminating variable with this isolation applied. The background falls rapidly for $dE/dx > 1.8 \text{ MeVg}^{-1}\text{cm}^2$

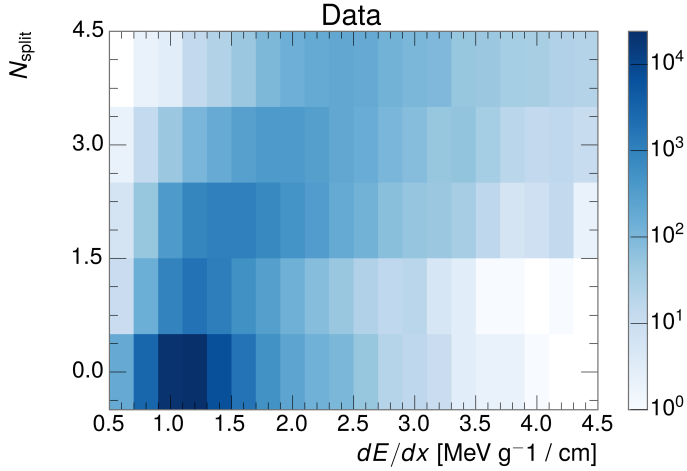


Figure 66: The dependence of dE/dx on N_{split} in data after basic track hit requirements have been applied.

while the majority of the signal, approximately 90% depending on the mass, falls above that threshold. Over 90% of LLP tracks in simulated signal events pass the N_{split} -based isolation requirement.

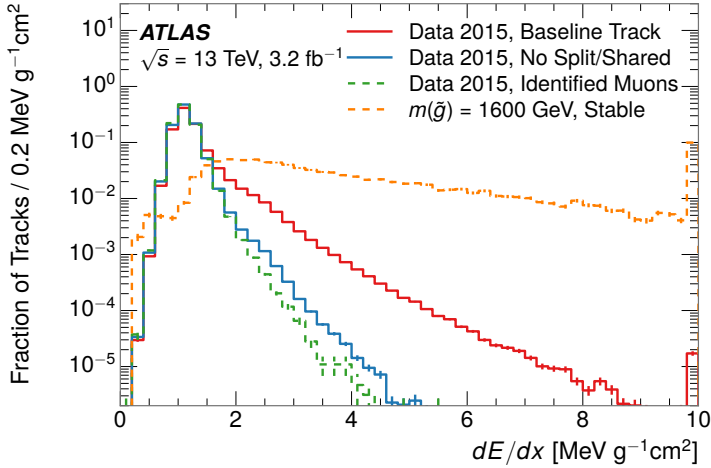


Figure 67: The distribution of dE/dx with various selections applied in data and simulated signal events.

A few additional kinematic requirements are imposed to help reduce SM backgrounds. The momentum of the candidate track must be at least 150 GeV, and the uncertainty on that measurement must be less than 50%. The distribution of momentum is shown in Figure 68 for tracks in data and simulated signal events after the previously discussed requirements on clusters, transverse momentum, and isolation have been imposed. The signal particles are much harder on aver-

age than their backgrounds because of the high energy interactions required to produce them. The transverse mass, M_T , defined as

$$M_T = \sqrt{2p_T E_T^{\text{miss}}(1 - \cos(\Delta\phi(E_T^{\text{miss}}, \text{track})))} \quad (8)$$

estimates the mass of a decay of to a single charged particle and an undetected particle and is required to be greater than 130 GeV to reject contributions from the decay of W bosons. Figure 69 shows the distribution of M_T for data and simulated signal events. The signal is distributed over a wide range of M_T , with about 90% above the threshold value of 130 GeV. The data shows a dual-peaked structure, where the first peak comes from W boson decays and the second peak is a kinematic shaping from the requirements on E_T^{miss} and the track p_T in dijet events.

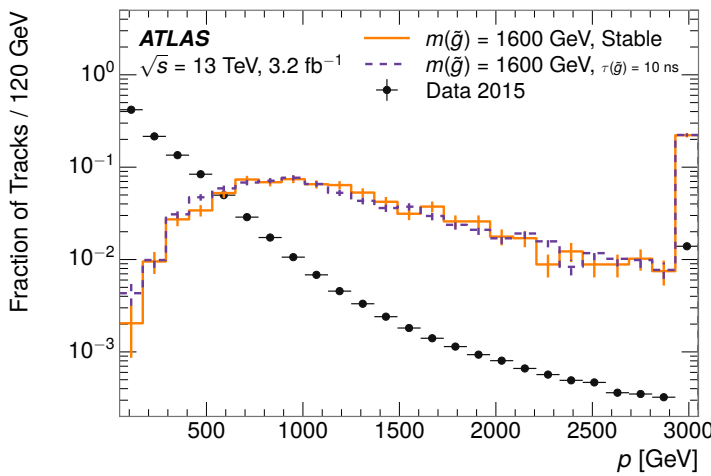


Figure 68: The distribution of track momentum for data and simulated signal events, after previous selection requirements have been applied.

11.3 PARTICLE SPECIES REJECTION

The amount of ionization deposited by particles with low mass and high momentum has a large positive tail [7], so backgrounds can be formed by a wide variety of SM processes when various charged particles have a few randomly large deposits of energy in the pixel detector. Those backgrounds can be additionally reduced by targeting other interactions with the detector where they are expected to have different behavior than R-Hadrons. The interactions with the detector depend on the types of particles produced rather than the processes which produce them, so this search forms a series of rejections to remove backgrounds from individual particle species. These rejections focus on using additional features of the event, other than the kinematics of the candidate track, as they can provide a powerful source of background rejection with very high signal efficiency. However, the lifetime of an R-Hadron can significantly change its

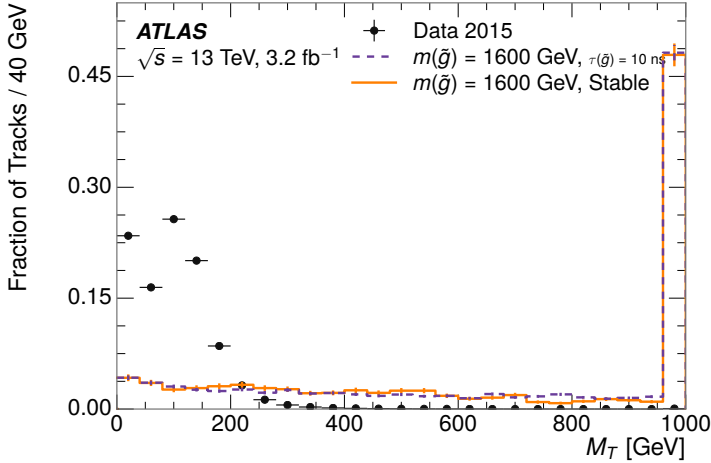


Figure 69: The distribution of M_T for data and simulated signal events, after previous selection requirements have been applied.

detector characteristics, as discussed in Section 10.1.2. To accommodate these differences, the SM rejections defined in this section are split to form two signal regions, one for long-lifetimes particles, the stable region ($50 \leq \tau[\text{ns}] < \infty \text{ ns}$), and one for intermediate lifetime particles, the metastable region ($0.4 < \tau[\text{ns}] < 50$).

Jets can be very effectively rejected by considering the larger-scale isolation of the candidate track. In this case the isolation focuses on the production of nearby particles as a jet-veto, rather than the isolation from overlapping tracks based on N_{split} that was used to reduce high-ionization backgrounds. As explained in Section 10.1, the fragmentation process which produces an R-Hadron is very hard and thus is not expected to produce additional particles with a summed momentum of more than 5 GeV. The jet-veto uses the summed momentum of tracks with a cone of $\Delta R < 0.25$, referred to as p_T^{Cone} , which is shown in Figure 70 for data and simulated signal events. In the data this value has a peak at zero from isolated tracks such as leptons, and a long tail from jets which contains as much as 80% of the background above 20 GeV at this stage of the selection. In signal events p_T^{Cone} is strongly peaked at zero and significantly less than 1% of signal events have p_T^{Cone} above 20 GeV. This makes a requirement of $p_T^{\text{Cone}} < 20 \text{ GeV}$ a very effective method to reject background without losing signal efficiency. For the stable signal region, this cut is further tightened to $p_T^{\text{Cone}} < 5 \text{ GeV}$ as it is the most effective variable remaining to extend the search reach for long lifetimes.

Even for fully isolated particles, there are additional methods to reject each type of particle using information in the muon system and calorimeters. Muons can be identified very reliably using the tracks in the muon system, as described in Section 7.3. For intermediate lifetimes the LLPs do not survive long enough to reach the muon system, and so muons are vetoed by rejecting tracks that associate to a muon with medium muon identification requirements (Section 7.3). For longer lifetimes, this rejection is not applied because LLPs which reach the

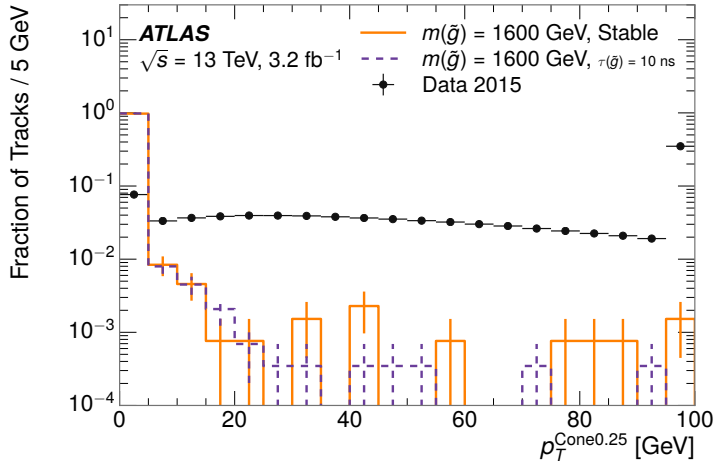


Figure 70: The distribution of summed tracked momentum within a cone of $\Delta R < 0.25$ around the candidate track for data and simulated signal events, after previous selection requirements have been applied.

2709 muon system can be identified as muons as often as 30% of the time in simulated
2710 samples.

2711 Calorimeter-based particle rejection relies on the expected small deposits of
2712 energy from LLPs. When the lifetime is long enough to reach the calorimeter, a
2713 LLP deposits little of its energy as it traverses the material, as discussed in Sec-
2714 tion 10.1. Even when the particle does decay before the calorimeter, the major-
2715 ity of its energy is carried away by the LSP and not deposited in the calorimeter.
2716 In both cases the energy is expected to be distributed across the layers of the
2717 calorimeters and not peaked in just one layer. This can be quantified in terms
2718 of E/p , the ratio of calorimeter energy of a nearby jet to the track momentum,
2719 and f_{EM} , the fraction of energy in that jet within the electromagnetic calorime-
2720 ter. When no jets fall within a cone of 0.05 of the particle, E/p and f_{EM} are both
2721 defined as zero. E/p is expected to be above 1.0 for typical SM particles because
2722 of calibration and the contributions from other nearby particles, as discussed in
2723 Chapter 8. At these momenta there is no significant zero fraction due to inter-
2724 actions with the detector or insufficient energy deposits (see Section 8.2.2). f_{EM}
2725 is peaked close to 1.0 for electrons, and distributed between 10% and 90% for
2726 hadrons.

2727 These trends can be seen in the two dimensional distribution for signal in
2728 Figure 71 for stable and metastable (10 ns) events. The majority of R-Hadrons
2729 in both samples fall into the bin for $E/p = 0$ and $f_{\text{EM}} = 0$ because the majority
2730 of the time there is no associated jet. In the stable sample, when there often is
2731 an associated jet, E/p is typically still below 0.1, and the f_{EM} is predominantly
2732 under 0.8. In the metastable sample, on the other hand, E/p is larger but still
2733 typically below 0.1 because of actual jets produced during the decay. The f_{EM} is
2734 much lower on average in this case, below 0.1, because the 10 ns lifetime particles
2735 rarely decay before passing through the electromagnetic calorimeter. Figure 71
2736 also includes simulated Z decays to electrons or tau leptons. From the decays

2737 to electrons it is clear that the majority of electrons have f_{EM} above 0.9. The
 2738 tau decays include a variety of products. Muons can be seen in the bin where
 2739 $E/p = 0$ and $f_{\text{EM}} = 0$ because they do not have an associated jet. Electrons fall
 2740 into the range where $E/p > 1$ and $f_{\text{EM}} > 0.9$. Hadronic tau decays are the most
 2741 common, and fall in the range of $0.1 < f_{\text{EM}} < 0.9$ and $E/p > 1.0$.

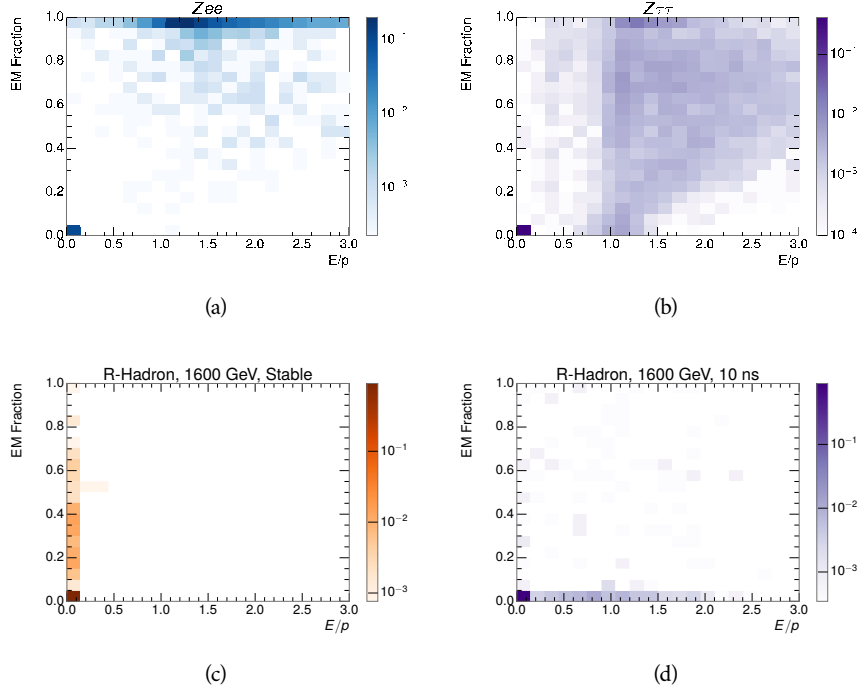


Figure 71: The normalized, two-dimensional distribution of E/p and f_{EM} for simulated
 (a) $Z \rightarrow ee$, (b) $Z \rightarrow \tau\tau$, (c) 1200 GeV Stable R-Hadron events, and (d) 1200
 GeV, 10 ns R-Hadron events.

2742 These differences motivate an electron rejection by requiring an f_{EM} below
 2743 0.9. Similarly, isolated hadrons are rejected by requiring $E/p < 1.0$. These re-
 2744 quirements combine to remove the majority of isolated electrons and hadrons
 2745 but retain over 95% of the simulated signal across a range of masses and lifetimes.

2746 11.4 IONIZATION

2747 The final requirement on the candidate track is the primary discriminating vari-
 2748 able, the ionization in the pixel detector. That ionization is measured in terms
 2749 of dE/dx , which was shown for data and simulated signal events in Figure 67.
 2750 dE/dx is dramatically greater for the high mass signal particles than the back-
 2751 grounds, which start to fall immediately after the minimally ionizing peak at 1.1
 2752 $\text{MeV g}^{-1} \text{cm}^2$. The dE/dx for candidate tracks must be greater than a pseudorapidity-
 2753 dependent threshold, specifically $1.80 - 0.11|\eta| + 0.17\eta^2 - 0.05\eta^3 \text{ MeV g}^{-1} \text{ cm}^{-2}$,
 2754 in order to correct for an approximately 5% dependence of the MIP peak on η .
 2755 The requirement was chosen as part of the signal region optimization, and man-

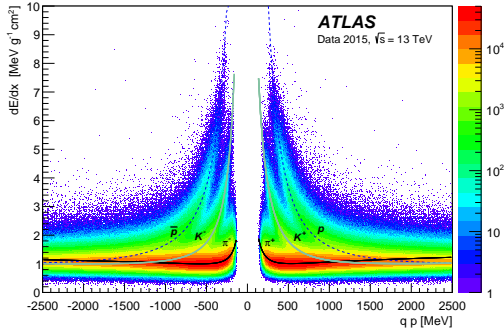


Figure 72: Two-dimensional distribution of dE/dx versus charge signed momentum (qp) for minimum-bias tracks. The fitted distributions of the most probable values for pions, kaons and protons are superimposed.

ages to reduce the backgrounds by a factor of 100 while remaining 70-90% efficient for simulated signal events depending on the mass.

11.4.1 MASS ESTIMATION

The mean value of ionization in silicon is governed by the Bethe equation and the most probable value follows a Landau-Vavilov distribution [7]. Those forms inspire a parametric description of dE/dx in terms of $\beta\gamma$,

$$(dE/dx)_{MPV}(\beta\gamma) = \frac{p_1}{\beta^{p_3}} \ln(1 + [p_2 \beta\gamma]^{p_5}) - p_4 \quad (9)$$

which performs well in the range $0.3 < \beta\gamma < 1.5$. This range includes the expected range of $\beta\gamma$ for the particles targeted for this search, with $\beta\gamma \approx 2.0$ for lower mass particles ($O(100 \text{ GeV})$) and up to $\beta\gamma \approx 0.5$ for higher mass particles ($O(1000 \text{ GeV})$). The parameters, p_i , are fit using a 2015 data sample of low-momentum pions, kaons, and protons as described in Ref. [83]. Figure 72 shows the two-dimensional distribution of dE/dx and momentum along with the above fitted values for $(dE/dx)_{MPV}$.

The above equation (9) is then numerically inverted to estimate $\beta\gamma$ and the mass for each candidate track. In simulated signal events, the mean of this mass value reproduces the generated mass up to around 1800 GeV to within 3%, and a 3% shift is applied to correct for this difference. The mass distributions prior to this correction are shown for a few stable mass points in Figure 73. The large widths of these distributions come from the high variability in energy deposits in the pixel detector as well as the uncertainty on momentum measurements at high momentum, but the means converge to the expected values.

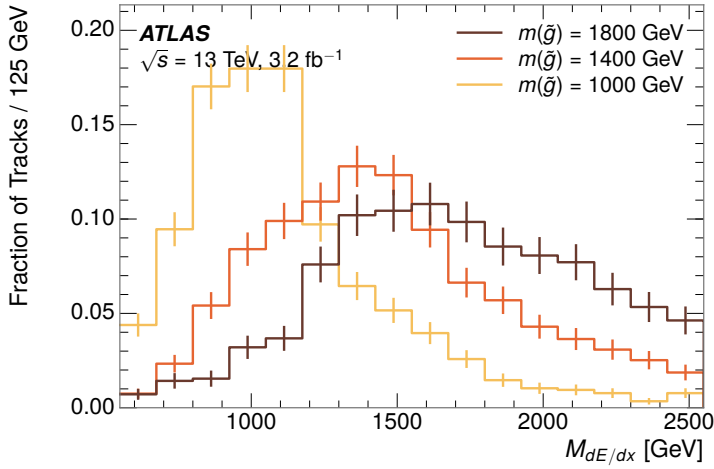


Figure 73: The distribution of mass estimated using dE/dx for simulated stable R-Hadrons with masses between 1000 and 1600 GeV.

2777 This analysis evaluates expected yields and the resulting cross sectional limits
 2778 using windows in this mass variable. The windows are formed by fitting mass
 2779 distributions in simulated signal events like those in Figure 73 to Gaussian distri-
 2780 butions and taking all events that fall within $\pm 1.4\sigma$ of the mean. As can be seen
 2781 in Figure 73, typical values for this width are $\sigma \approx 300 - 500$ GeV depending on
 2782 the generated mass.

2783 11.5 EFFICIENCY

2784 The numbers of events passing each requirement through ionization are shown
 2785 in Table 8 for the full 2015 dataset and a simulated 1600 GeV, 10 ns lifetime R-
 2786 Hadron sample. The table highlights the overall acceptance \times efficiency for sig-
 2787 nals events, which for this example is 19%. Between SM rejection and ionization,
 2788 this signal region reduces the background of tracks which pass the kinematic
 2789 requirements down by an additional factor of almost 2000.

2790 There is a strong dependence of this efficiency on lifetime and mass, with effi-
 2791 ciencies dropping to under 1% at low lifetimes. Figure 74 shows the dependence
 2792 on both mass and lifetime for all signal samples considered in this search. The
 2793 dependence on mass is relatively slight and comes predominantly from the in-
 2794 creasing fraction of R-Hadrons which pass the ionization cut with increasing
 2795 mass. The trigger and E_T^{miss} requirements are most efficient for particles that
 2796 decay before reaching the calorimeters. However, the chance of a particle to be
 2797 reconstructed as a high-quality track decreases significantly at low lifetimes as
 2798 the particle does not propagate sufficiently through the inner detector. These
 2799 effects lead to a maximum in the selection efficiency for lifetimes around 10-30
 2800 ns.

2801 The inefficiency of this signal region at short lifetimes comes almost exclu-
 2802 sively from an acceptance effect, in that the particles do not reach the necessary

Selection	Exp. Signal Events	Observed Events in 3.2 fb^{-1}
Generated	26.0 ± 0.3	
E_T^{miss} Trigger	24.8 ± 0.3 (95%)	
$E_T^{\text{miss}} > 130 \text{ GeV}$	23.9 ± 0.3 (92%)	
Track Quality and $p_T > 50$	10.7 ± 0.2 (41%)	368324
Isolation Requirement	9.0 ± 0.2 (35%)	108079
Track $p > 150 \text{ GeV}$	6.6 ± 0.2 (25%)	47463
$M_T > 130 \text{ GeV}$	5.8 ± 0.2 (22%)	18746
Electron and Hadron Veto	5.5 ± 0.2 (21%)	3612
Muon Veto	5.5 ± 0.2 (21%)	1668
Ionization Requirement	5.0 ± 0.1 (19%)	11

Table 8: The expected number of events at each level of the selection for metastable $1600 \text{ GeV}, 10 \text{ ns}$ R-Hadrons, along with the number of events observed in data, for 3.2 fb^{-1} . The simulated yields are shown with statistical uncertainties only. The total efficiency \times acceptance is also shown for the signal.

2803 layers of the SCT. This can be seen more clearly by defining a fiducial region
 2804 which includes events with at least one R-Hadron that is produced with non-
 2805 zero charge, $p_T > 50 \text{ GeV}$, $p > 150 \text{ GeV}$, $|\eta| < 2.5$, and a decay distance greater
 2806 than 37 cm in the transverse plane. At short (1 ns) lifetimes, the acceptance into
 2807 this region is as low as 4%. Once this acceptance is accounted for, the selection
 2808 efficiency ranges from 25% at lifetimes of 1 ns up to 45% at lifetimes of 10 ns.

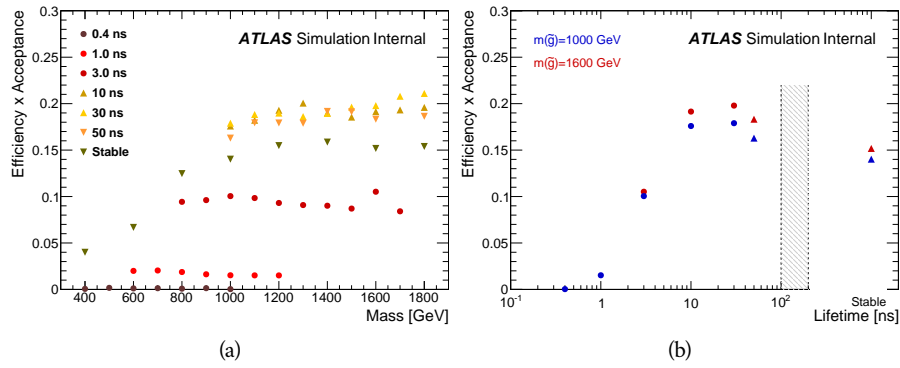


Figure 74: The acceptance \times efficiency as a function of R-Hadron (a) mass and (b) lifetime. (a) shows all of the combinations of mass and lifetime considered in this search, and (b) highlights the lifetime dependence for 1000 GeV and 1600 GeV R-Hadrons.

2809

2810 BACKGROUND ESTIMATION

2811 The event selection discussed in the previous section focuses on detector signa-
 2812 tures, emphasizing a single high-momentum, highly-ionizing track. That track
 2813 is then required to be in some way inconsistent with the expected properties
 2814 of SM particles, with various requirements designed to reject jets, hadrons,
 2815 electrons, and muons (Section 11.3). Therefore the background for this search comes
 2816 entirely from reducible backgrounds that are outliers of various distributions in-
 2817 cluding dE/dx , f_{EM} , and p_T^{Cone} . The simulation can be tuned in various ways to
 2818 do an excellent job of modeling the average properties of each particle type [84],
 2819 but it is not necessarily expected to accurately reproduce outliers. For this rea-
 2820 sons, the background estimation used for this search is estimated entirely using
 2821 data.

2822 12.1 BACKGROUND SOURCES

2823 SM charged particles with lifetimes long enough to form tracks in the inner de-
 2824 tector can be grouped into three major categories based on their detector inter-
 2825 actions: hadrons, electrons, and muons. Every particle that enters into the back-
 2826 ground for this search belongs to one of these types. Relatively pure samples of
 2827 tracks from each of these types can be formed in data by inverting the various
 2828 rejection techniques in Section 11.3. Specifically, muons are selected requiring
 2829 medium muon identification, electrons requiring $E/p > 1.0$ and $f_{EM} > 0.95$,
 2830 and hadrons requiring $E/p > 1.0$ and $f_{EM} < 0.95$.

2831 Figure 75 shows the distributions of momentum and dE/dx for these cate-
 2832 gories in data, after requiring the event level selection as well as the track re-
 2833 quirements on p_T , hits, and N_{split} , as discussed in Section 11.2. Simulated signal
 2834 events are included for reference. These distribution are only illustrative of the
 2835 differences between types, as the rejection requirements could alter their shape.
 2836 This is especially significant for momentum which enters directly into E/p and
 2837 can indirectly affect muon identification. However the various types show clear
 2838 differences in both distributions. The distributions of momentum are not nec-
 2839 essarily expected to match between the various types because the production
 2840 mechanisms for each type result in different kinematic distributions. dE/dx is
 2841 also different between types because of incomplete isolation; although the re-
 2842 quirement on N_{split} helps to reduce the contribution of nearby particles it does
 2843 not completely remove the effect of overlaps. Muons are better isolated because
 2844 they do not have the additional particle from hadronization present for hadrons
 2845 and they are significantly less likely do interact with the detector and produce
 2846 secondary particles compared to hadrons and electrons. Thus muons have the
 2847 smallest fraction of dE/dx above the threshold of $1.8 \text{ MeVg}^{-1}\text{cm}^2$; hadrons and
 2848 electrons have a larger fraction above this threshold.

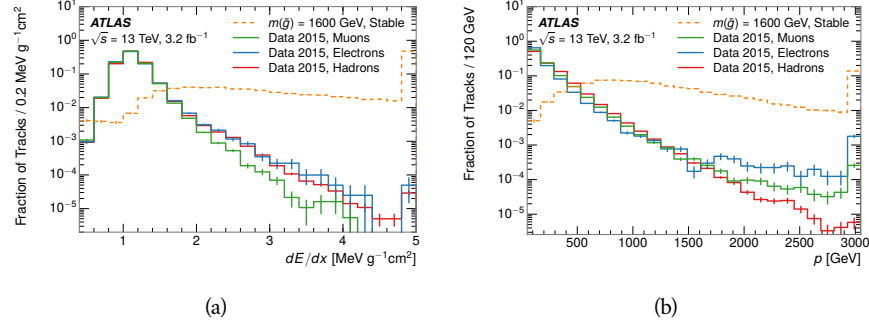


Figure 75: The distribution of (a) dE/dx and (b) momentum for tracks in data and simulated signal after requiring the event level selection and the track selection on p_T , hits, and N_{split} . Each sub-figure shows the normalized distributions for tracks classified as hadrons, electrons, and muons in data and R-Hadrons in the simulated signal.

2849 It is difficult to determine what fraction of each particle type enters into the fi-
 2850 nal signal region. The background method will not have significant dependence
 2851 on the relative contributions of each species, but it is useful to understand the
 2852 differences between each when considering the various tests of the method.

2853 12.2 PREDICTION METHOD

2854 The data-driven background estimation relies on the independence between ion-
 2855 ization and other kinematic variables in the event. For standard model particles
 2856 with momenta above 50 GeV, dE/dx is not correlated with momentum; though
 2857 there is a slight relativistic rise as momentum increases, the effect is small com-
 2858 pared to the width of the distribution of ionization energy deposits.. So, the
 2859 proposed method to estimate the mass distribution of the signal region is to use
 2860 momentum from a track with low dE/dx (below the threshold value) and to com-
 2861 bine it with a random dE/dx value from a dE/dx template. The resulting track is
 2862 just as likely as the original, so a number of such random generations provide the
 2863 expected distributions of momentum and ionization. These are then combined
 2864 using the parametrization described in Section 11.4.1 to form a distribution of
 2865 mass for the signal region.

2866 Algorithmically this method is implemented by forming two distinct Control
 2867 Regions (**CR**s). The first **CR**, CR1, is formed by applying the entire event selec-
 2868 tion from Chapter 11 up to the dE/dx and mass requirements. The dE/dx re-
 2869 quirement is instead inverted for this region. Because of the independence of
 2870 dE/dx , the tracks in this control region have the same kinematic distribution
 2871 as the tracks in the signal region, and are used to measure a two-dimensional
 2872 template of p and η . The second **CR**, CR2, is formed from the event selection
 2873 through the dE/dx requirement, but with an inverted E_T^{miss} requirement. The
 2874 tracks in this control region are expected to have similar dE/dx distributions to
 2875 the signal region before the ionization requirement, and so this region is used to
 2876 measure a two-dimensional template of dE/dx and η .

2877 The contribution of any signal to the control regions is minimized by the in-
 2878 verted selection requirements. Only less than 10% of simulated signal events
 2879 have either dE/dx or E_T^{miss} below the threshold values in the original signal re-
 2880 gion, while the backgrounds are significantly enhanced by inverting those re-
 2881 quirements. The signal contamination is less than 1% in both control regions
 2882 for all of the simulated masses and lifetimes considered in this analysis.

2883 With those measured templates, the shape of the mass estimation is generated
 2884 by first selecting a random (p, η) combination from CR1. This momentum
 2885 value is combined with a dE/dx value taken from the appropriate distribution
 2886 of dE/dx for the selected η from CR2. The use of η in both random samplings
 2887 controls for any correlation between p , dE/dx , and η . Those values are then
 2888 used to calculate a mass in the same way that is done for regular tracks in data,
 2889 see Section 11.4.1. As this procedure includes all dE/dx values, the cut at 1.8
 2890 MeVg $^{-1}$ cm 2 is then enforced to fully model the signal region. The generated
 2891 mass distribution is then normalized by scaling the background estimate to the
 2892 data in the region $M < 160$ GeV, where signals of this type have already been
 2893 excluded [68]. This normalization uses the distributions of mass generated with-
 2894 out the ionization requirement.

2895 The statistical uncertainties on these background distributions are calculated
 2896 by independently fluctuating each bin of the input templates according to their
 2897 Poisson uncertainties. These fluctuations are repeated a large number of times,
 2898 and the uncertainty on the resulting distribution is taken as the root mean square
 2899 (RMS) deviation of the fluctuations from the average. As the procedure uses one
 2900 million random combinations to generate the distributions, The statistical un-
 2901 certainty from the actual random generations is negligible compared to the un-
 2902 certainty from measuring the templates.

2903 12.3 VALIDATION

2904 The validity of the background estimation technique can be evaluated in both
 2905 data and simulation. The underlying assumption that random combinations of
 2906 dE/dx and momentum can predict a mass distribution in an orthogonal region
 2907 can be tested using simulated samples where concerns like multiple particle types
 2908 can be controlled. Using the same technique in another set of signal-depleted
 2909 regions in data then extends this confidence to the more complicated case where
 2910 several particle species are inherently included.

2911 12.3.1 CLOSURE IN SIMULATION

2912 The first test of the procedure is done using a simulated sample of $W \rightarrow \mu\nu$
 2913 decays. These types of events provide the ingredients required to test the back-
 2914 ground estimate, E_T^{miss} and isolated tracks, with high statistics. In this example
 2915 there is no signal, so simulated events in the orthogonal CRs are used to estimate
 2916 the shape of the mass distribution of the simulated events in the signal region. To
 2917 reflect the different topology for W boson decays, the CRs use slightly modified
 2918 definitions. In all CRs, the requirement of $p > 150$ GeV and the SM rejection

2919 requirements are removed. Additionally, for the signal region the requirement
 2920 on E_T^{miss} is relaxed to 30 GeV and the corresponding inverted requirement on
 2921 CR2 is also set at 30 GeV.

2922 With these modified selections, the simulated and randomly generated distri-
 2923 butions of $M_{dE/dx}$ are shown in Figure 76. This figure includes the mass distri-
 2924 butions before and after the requirement on dE/dx , which significantly shapes
 2925 the distributions. In both cases the background estimation technique repro-
 2926 duces the shape of $M_{dE/dx}$ in the signal region. There is a small difference in the pos-
 2927 itive tail of the mass distribution prior to the ionization cut, where the random
 2928 events underestimate the fraction of tracks with mass above 150 GeV by about
 2929 20%. After the ionization requirement, however, this discrepancy is not present
 2930 and the two distributions agree to within statistical uncertainties.

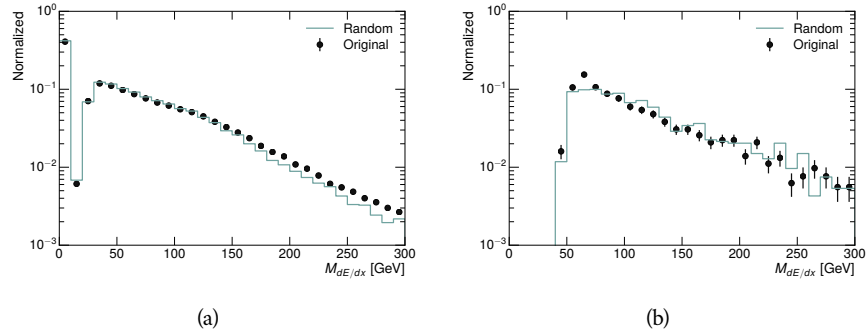


Figure 76: The distribution of $M_{dE/dx}$ (a) before and (b) after the ionization requirement for tracks in simulated W boson decays and for the randomly generated back-
 ground estimate.

2931 This ability to reproduce the shape of the mass distribution in simulated events
 2932 shows that the technique works as expected. No significant biases are acquired
 2933 in using low dE/dx events to select kinematic templates or in using low E_T^{miss}
 2934 events to select ionization templates, as either would result in a mismodeling of
 2935 the shape of the mass distribution. The simulated events contain only one par-
 2936 ticle type, however, so this test only establishes that the technique works well
 2937 when the the CRs are populated by exactly the same species.

2938 12.3.2 VALIDATION REGION IN DATA

2939 The second test of the background estimate is performed using data in an or-
 2940 thogonal validation region. The validation region, and the corresponding CRs,
 2941 are formed using the same selection requirements as in the nominal method but
 2942 with a modified requirement on momentum, $50 < p[\text{GeV}] < 150$. This allows
 2943 the technique to be checked in a region with very similar properties but where
 2944 the signal is depleted, as the majority of the signal has momentum above 150
 2945 GeV while the backgrounds are enhanced below that threshold. Any biases on
 2946 the particle composition of the CRs for the signal region will be reflected in the
 2947 CRs used to estimate the mass distribution in the validation region.

2948 Figure 77 shows the measured and randomly generated mass distributions for
 2949 data before and after the ionization requirement. The background estimate does
 2950 an excellent job of modeling the actual background before the ionization require-
 2951 ment, with good agreement to within the statistical uncertainties out to the limit
 2952 of the mass distribution. There are very few events in the validation region after
 2953 the ionization requirement, but the few observed events are consistent with the
 2954 background prediction. The good agreement in this validation region provides
 2955 a confirmation that the technique works even in the full-complexity case with
 2956 multiple particle types entering the distributions. Any bias from changes in par-
 2957 ticle composition between regions is small compared to statistical uncertainties.

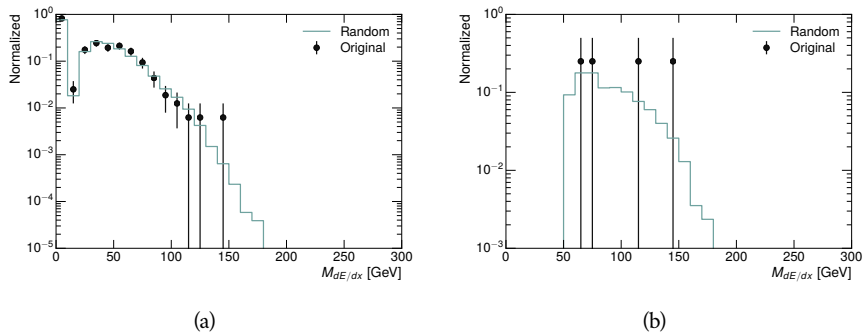


Figure 77: The distribution of $M_{dE/dx}$ (a) before and (b) after the ionization require-
 ment for tracks in the validation region and for the randomly generated back-
 ground estimate.

2958

2959 SYSTEMATIC UNCERTAINTIES AND RESULTS

2960 13.1 SYSTEMATIC UNCERTAINTIES

2961 A number of systematic uncertainties affect the interpretation of the results of
 2962 the search. These uncertainties can broken down into two major categories,
 2963 those which affect the estimate of the background using data and those which
 2964 affect the measurement of the signal yield estimated with simulated events. The
 2965 total measured systematic uncertainties are 7% for the background estimation
 2966 and approximately 32% for the signal yield depending on lifetime. These system-
 2967atic uncertainties are expected to be small compared to the statistical fluctuations
 2968 of the measured yields so that measured cross-sectional limits will be dominated
 2969 by statistical uncertainties. The following sections describe each source of sys-
 2970 tematic uncertainty for each of the two types.

2971 13.1.1 BACKGROUND ESTIMATE

2972 The systematic uncertainties on the background estimate come primarily from
 2973 considering alternative methods for generating the background distributions.
 2974 These uncertainties are small compared to the statistical uncertainties on the
 2975 background estimate which come from the limited statistics in measuring the
 2976 template distributions, as described in Section 12.2. They are summarized in
 2977 Table 9.

Source of Uncertainty:	Value [%]
Analytic Description of dE/dx	4.0
Muon Fraction (Stable Region only)	3.0
IBL Ionization Correction	3.8
Normalization	3.0
Total (Metastable Region):	6.3
Total (Stable Region):	7.0

Table 9: A summary of the sources of systematic uncertainty for the data-driven background in the signal region. If the uncertainty depends on the mass, the maximum values are reported.

2978 13.1.1.1 ANALYTIC DESCRIPTION OF DE/DX

2979 The background estimate uses a binned template distribution to estimate the
 2980 dE/dx of tracks in the signal region, as described in Section 12.2. It is also possi-

ble to fit that measured distribution to a functional form to help smooth the distribution in the tails of dE/dx where the template is driven by a small number of tracks. Both Landau convolved with a Gaussian and Crystal Ball functions are considered as the functional form and used to re-estimate the background distribution. The deviations compared to the nominal method are found to be 4%, and this is taken as a systematic uncertainty to cover the inability carefully predict the contribution from the long tail of dE/dx where there are few measurements available in data.

2989 13.1.1.2 MUON FRACTION

2990 The stable region of the analysis explicitly includes tracks identified as muons,
 2991 which have a known difference in their dE/dx distributions compared to non-
 2992 muon tracks (Section 12.1). To account for a difference in muon fraction be-
 2993 tween the background region and the signal region for this selection, the dE/dx
 2994 templates for muons and non-muons are measured separately and then the rel-
 2995 ative fraction of each is varied in the random generation. The muon fraction
 2996 is varied by its statistical uncertainty and the resulting difference of 3% in back-
 2997 ground yield is taken as the systematic uncertainty.

2998 13.1.1.3 IBL CORRECTIONS

2999 The IBL, described in Section 6.3.1, received a significant dose of radiation during
 3000 the data collection in 2015. The irradiation can cause a drift in the frontend
 3001 electronics and thus alter the dE/dx measurement which includes the ToT output
 3002 by the IBL. These effects are corrected for in the nominal analysis by scaling the
 3003 dE/dx measurements by a constant factor derived for each run to match the
 3004 average dE/dx value to a reference run where the IBL was known to be stable
 3005 to this effect. However, this corrective factor does not account for inter-run
 3006 variations. To account for this potential drift of dE/dx , the correction procedure
 3007 is repeated by varying the corrections up and down by the maximal run-to-run
 3008 variation from the full data-taking period, which results in an uncertainty of
 3009 3.8%.

3010 13.1.1.4 NORMALIZATION

3011 As described in Section 12.2, the generated distribution of masses is normalized
 3012 in a shoulder region ($M < 160$ GeV) where signals have been excluded by pre-
 3013 vious analyses. That normalization factor is varied by its statistical uncertainty
 3014 and the resulting fluctuation in the mass distribution of 3% is taken as a system-
 3015 atic uncertainty on the background estimate.

3016 13.1.2 SIGNAL YIELD

3017 The systematic uncertainties on the signal yield can be divided into three cate-
 3018 gories; those on the simulation process, those on the modeling of the detector
 3019 efficiency or calibration, and those affecting the overall signal yield. They are
 3020 summarized in Table 9. The largest uncertainty comes from the uncertainty on

3021 the production cross section for gluinos, which is the dominant systematic un-
 3022 certainty in this analysis.

Source of Uncertainty	-[%]	+[%]
ISR Modeling (Metastable Region)	1.5	1.5
ISR Modeling (Stable Region)	14	14
Pile-up Reweighting	1.1	1.1
Trigger Efficiency Reweighting	0.9	0.9
E_T^{miss} Scale	1.1	2.2
Ionization Parametrization	7.1	0
Momentum Parametrization	0.3	0.0
Electron Rejection	0.0	0.0
Hadron Rejection	0.0	0.0
μ Identification	4.3	4.3
Luminosity	5	5
Signal size uncertainty	28	28
Total (Metastable Region)	30	29
Total (Stable Region)	33	32

Table 10: A summary of the sources of systematic uncertainty for the simulated signal yield. The uncertainty depends on the mass and lifetime, and the maximum negative and positive values are reported in the table.

3023 13.1.2.1 ISR MODELING

3024 As discussed in Section 10.2, MadGraph is expected to reproduce the distribution
 3025 of ISR in signal events more accurately than the nominal Pythia samples. The
 3026 analysis reweights the distribution of ISR in the simulated signal events to match
 3027 the distribution found in generated MadGraph samples. This has an effect on the
 3028 selection efficiency in the signal samples, where ISR contributes to the generation
 3029 of E_T^{miss} . To account for the potential inaccuracy on the simulation of ISR at high
 3030 energies, half of the difference between the signal efficiency with the reweighted
 3031 distribution and the original distribution is taken as a systematic uncertainty.

3032 13.1.2.2 PILEUP REWEIGHTING

3033 The simulated events were generated prior to data collection with an estimate of
 3034 the average number of interactions per bunch crossing. This estimate does not
 3035 match the value of pileup during actual data collection, but a large fraction of the
 3036 simulated events would be discarded in order to match the distribution in data.
 3037 Therefore the simulated signal events are not reweighted for pileup by default
 3038 in the analysis. The effect of the pileup on signal efficiency is not expected to
 3039 depend on the mass or lifetime of the generated signal events, which allows all

3040 of the generated signal events to be used together to assess the pileup dependence.
 3041 To account for the potential effect of the difference in the number of interactions
 3042 per bunch crossing between data and simulation, the difference in yield between
 3043 the nominal signal events and the reweighted events averaged over all masses
 3044 and lifetimes is taken as a systematic uncertainty on the yield for each mass and
 3045 lifetime (1.1%).

3046 13.1.2.3 TRIGGER EFFICIENCY REWEIGHTING

3047 As described in Section 11.2, the selection for this analysis does not require a suf-
 3048 ficiently large value of E_T^{miss} to be above the plateau of trigger efficiency. There-
 3049 fore, some signal events which would otherwise pass the event selection can be
 3050 excluded because of the trigger requirement. These effects can be difficult to es-
 3051 timate in simulation, and thus are constrained by comparing data and simulated
 3052 events in an alternative W boson region which uses decays to muons to find a rel-
 3053 atively pure sample of events with missing energy. The trigger efficiency for data
 3054 and simulated W events are shown in Figure 78. The comparison between data
 3055 and MC in this region constrains the simulation of the trigger efficiency. The
 3056 simulated signal events are reweighted by the ratio of data to simulation in the
 3057 W boson decays, while the difference between the data and simulation in those
 3058 decays is taken as a systematic uncertainty. This results in an uncertainty of only
 3059 0.9% as the majority of events are well above the plateau and the disagreement
 3060 between data and simulation is small even below that plateau.

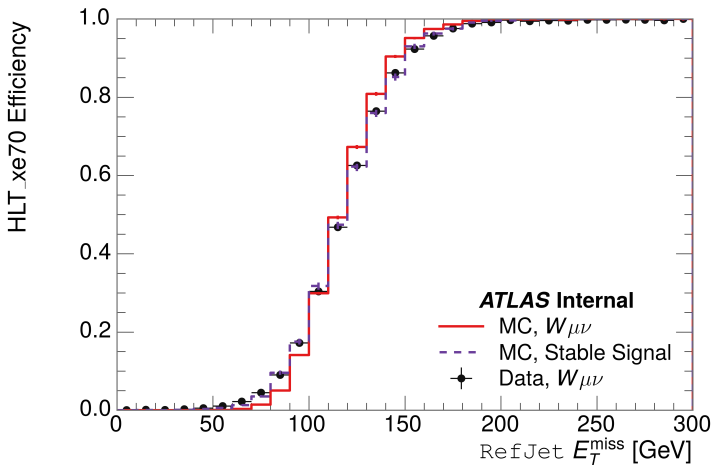


Figure 78: The trigger efficiency for the HLT_xe70 trigger requirement as a function of Calorimeter E_T^{miss} for simulated data events with a W boson selection. Simulated signal events and simulated W boson events are also included.

3061 13.1.2.4 MISSING TRANSVERSE MOMENTUM SCALE

3062 The ATLAS Combined Performance (CP) group provides a default recommenda-
 3063 tion for systematic variations of jets and missing energy (**note: I'm not quite**
 3064 **sure what to cite for this - I don't see any papers from the jet/met group**

Systematic Variation	-[%]	+[%]
JET_GroupedNP_1	-0.7	1.3
JET_GroupedNP_2	-0.7	1.2
JET_GroupedNP_3	-0.5	1.3

Table 11: Example of the contributing systematic variations to the total systematic for the E_T^{miss} Scale, as measured in a 1200 GeV, Stable R-Hadron signal sample.

3065 **after this was implemented).** These variations enter into this analysis only in
 3066 the requirement on E_T^{miss} . The effect of the measured scale of E_T^{miss} is evaluated
 3067 by varying the E_T^{miss} scale according to the one sigma variations provided by all
 3068 **CP** recommendations on objects affecting event kinematics in simulated signal
 3069 events. Missing energy is reconstructed from fully reconstructed objects so any
 3070 systematic uncertainties affecting jets, muons, electrons, or the E_T^{miss} soft terms
 3071 are included. The only non-negligible contributions found using this method are
 3072 itemized in Table 11 for an example signal sample (1200 GeV, Stable R-Hadron),
 3073 where the systematic is measured as the relative difference in the final signal ef-
 3074 ficiency after applying the associated variation through the CP tools. The only
 3075 variations that are significant are the grouped jet systematic variations, which
 3076 combine recommended jet systematic uncertainties into linearly independent
 3077 variations.

3078 As the peak of the reconstructed E_T^{miss} distribution in the signal is significantly
 3079 above the current threshold for events which pass the trigger requirement, the
 3080 effect of scale variation is expected to be small, which is consistent with the mea-
 3081 sured systematic of approximately 2%. Events which do not pass the trigger re-
 3082 quirement usually fail because there are no ISR jets in the event to balance the
 3083 R -hadrons' transverse momentum, so the reconstructed E_T^{miss} is low and there-
 3084 fore also expected to be not very sensitive to scale changes.

3085 13.1.2.5 MOMENTUM PARAMETRIZATION

3086 The uncertainty on the signal efficiency from track momentum is calculated us-
 3087 ing the **CP** group recommendations for tracks. In particular, only one recom-
 3088 mended systematic variation affects track momentum, the sagitta bias for q/P .
 3089 This uncertainty is propagated to the final selection efficiency by varying the
 3090 track momentum by the recommended one sigma variation, and the associated
 3091 uncertainty is found to be negligible (0.3%).

3092 13.1.2.6 IONIZATION REQUIREMENT

3093 The dE/dx distributions in data and simulated events have different most prob-
 3094 able values, which is due in part to radiation effects in the detector that are not
 3095 fully accounted for in the simulation. The difference does not affect the mass
 3096 measurement used in this analysis, as independent calibrations are done in sim-
 3097 ulation and in data. However, it does affect the efficiency of the high dE/dx
 3098 selection requirement. To calculate the size of the effect on the signal efficiency,

3099 the dE/dx distribution in signal simulation is scaled by a scale factor obtained
 3100 from comparing the dE/dx distribution of inclusive tracks in data and in sim-
 3101 ulation. The difference in efficiency for this sample with a scaled dE/dx dis-
 3102 tribution, relative to the nominal case, is taken as a systematic uncertainty on
 3103 signal efficiency. The uncertainty is as large as 7% for low masses and falls to a
 3104 negligible effect for large masses.

3105 13.1.2.7 ELECTRON AND JET REJECTION

3106 The systematic uncertainty on the electron rejection is measured by varying the
 3107 EM fraction requirement significantly, from 0.95 to 0.9. This is found to have
 3108 a less than 0.04% effect on signal acceptance, on average, and so is completely
 3109 negligible. Similarly, the uncertainty on jet rejection is measured by tightening
 3110 the E/p requirement from 0.5 to 0.4. This is found to have no effect on signal
 3111 acceptance, so again the systematic is again negligible.

3112 13.1.2.8 MUON VETO

3113 The metastable signal region requires that the candidate tracks are not identi-
 3114 fied as medium muons because the majority of R-Hadrons in the lifetime range
 3115 included in that region do not reach the muon spectrometers before they de-
 3116 cay. However, the exponential tail of the R-Hadron lifetime distribution results
 3117 in some R-Hadrons traversing the muon spectrometer. These can still fail the
 3118 muon medium identification because they can fail on the requirement on the
 3119 number of precision hits required to pass the loose selection because they ar-
 3120 rive late to the muon spectrometer. This can be seen in Figure 79, which shows
 3121 the efficiency of the muon veto as a function of $1/\beta$, for two simulated stable
 3122 R-Hadron samples.

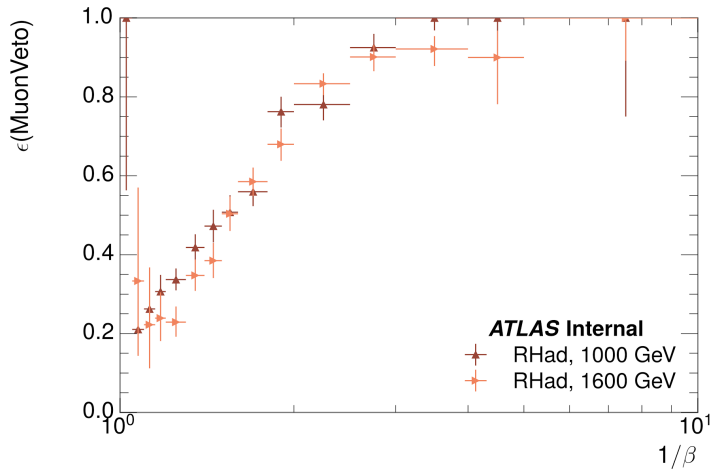


Figure 79: The efficiency of the muon veto for R -hadrons of two different masses, as a function of $1/\beta$ for simulated R-Hadron tracks.

3123 Thus, the efficiency of the muon veto depends on the timing resolution of
 3124 the spectrometer, so an uncertainty is applied to the signal efficiency to cover

3125 differences in timing resolution between data and simulation. First, a sample of
 3126 $Z \rightarrow \mu\mu$ events is selected in data in which one of the muons has a late arrival
 3127 time measured in the MDT. Then the reconstructed β distribution is compared
 3128 to the distribution in simulated $Z \rightarrow \mu\mu$ events; the difference between these
 3129 two distributions reflects the difference in timing resolution between data and
 3130 simulation. To emulate this difference in simulated signal events, the magnitude
 3131 of the difference is used to scale and shift the true β distribution of R-Hadrons in
 3132 simulation. Signal events are then reweighted based on this varied β distribution,
 3133 and the difference in the efficiency of the muon veto selection is compared with
 3134 the nominal and reweighted true β distributions. The difference in muon veto
 3135 efficiency is taken as a systematic uncertainty of the muon veto.

3136 The comparison of reconstructed β between data and simulation is performed
 3137 separately in the barrel, transition, and endcap regions of the spectrometer, and
 3138 the reweighting of the true β distribution in signal is done per region. The com-
 3139 parison of average reconstructed MDT β between data and simulation for the
 3140 barrel region is shown in Figure 80 for $Z \rightarrow \mu\mu$ events. As expected, The uncer-
 3141 tainty is found to be negligible for R-hadrons with short lifetimes, and is only
 3142 significant for lifetimes above 30 ns.

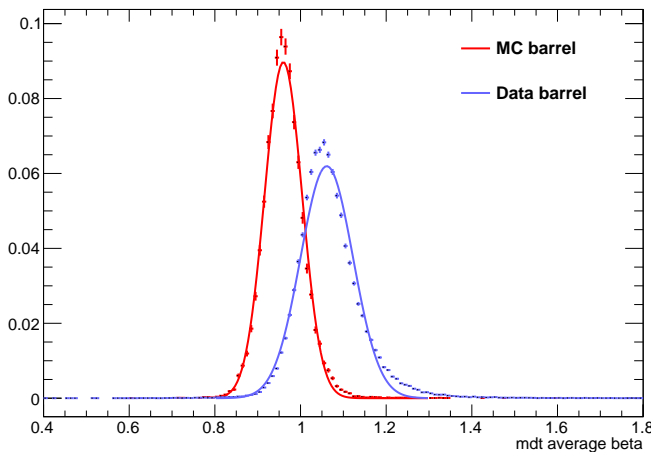


Figure 80: The average reconstructed MDT β distribution for $Z \rightarrow \mu\mu$ events in which
 one of the muons is reconstructed as a slow muon, for both data and simula-
 tion. A gaussian fit is superimposed.

3143 13.1.2.9 LUMINOSITY

3144 The luminosity uncertainty is provided by a luminosity measurement on ATLAS
 3145 and was measured to be 5% at the time of the publication of this analysis.

3146 13.1.2.10 SIGNAL SIZE

3147 As discussed in Section 10.2, the signal cross sections are calculated at NLO in the
 3148 strong coupling constant with a resummation of soft-gluon emission at NLL. The
 3149 uncertainties on those cross sections are between 14% to 28% for the R-Hadrons

Selection Region	Expected Background	Data
Stable	$17.2 \pm 2.6 \pm 1.2$	16
Metastable	$11.1 \pm 1.7 \pm 0.7$	11

Table 12: The estimated number of background events and the number of observed events in data for the specified selection regions prior to the requirement on mass. The background estimates show statistical and systematic uncertainties.

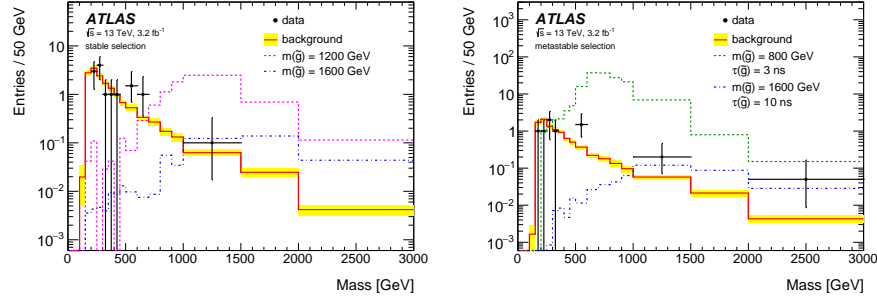


Figure 81: The observed mass distribution of events in data and the generated background distribution in (a) the stable and (b) the metastable signal region. A few example simulated signal distributions are superimposed.

3150 in the range of 400 to 1800 GeV [80, 81], where the uncertainty increases with
 3151 the mass.

3152 13.2 FINAL YIELDS

3153 This full analysis was performed using the 3.2 fb^{-1} from the 2015 data-taking.
 3154 Using the selections discussed in Chapter 11, sixteen events were observed in
 3155 the stable signal region and eleven events were observed in the metastable signal
 3156 region, prior to requirements on the candidate track mass. The background esti-
 3157 mate discussed in Chapter 12 predicts $17 \pm 2.6(\text{stat}) \pm 1.2(\text{syst})$ events for the
 3158 stable region and $11.1 \pm 1.7(\text{stat}) \pm 0.7(\text{syst})$ events for the metastable region.
 3159 These counts are summarized in Table 12.

3160 The mass estimated using dE/dx (Section 11.4.1) provides the final discrimi-
 3161 nating variable, where the signal would be expected as an excess in the falling ex-
 3162 ponential tail of the expected background. The observed distribution of masses
 3163 is shown in Figure 81, along with the predicted distribution from the background
 3164 estimate for each signal region. Both include a few example simulated signal dis-
 3165 tributions, which show the scale of an excess were the R-Hadron signals present.
 3166 Their is no statistically significant evidence of an excess in the data over the back-
 3167 ground estimation. From this distribution it is clearly possible to rule out signals
 3168 with lower masses, around 1200 GeV, which have larger cross sections.

3169 13.3 CROSS SECTIONAL LIMITS

3170 Because there is no observed significant excess of events in the signal region, this
 3171 analysis sets upper limits on the allowed cross section for R-Hadron production.
 3172 These limits are set for each mass point by counting the observed events in data,
 3173 along with the expected background and simulated signal events, in windows of
 3174 mass. The mass windows are formed by fitting the distribution of signal events to
 3175 a Gaussian distribution, and the window is then $\pm 1.4\sigma$ around the center of that
 3176 Gaussian. Two examples of the windows formed by this procedure are shown
 3177 in Tables 13-14, for the stable and 10 ns working points. The corresponding
 3178 counts of observed data, expected background, and simulated signal for those
 3179 same working points are shown in Tables 15-16. Appendix B includes the mass
 3180 windows and counts for all of the considered signal points.

$m(\tilde{g})$ [GeV]	Left Extremum [GeV]	Right Extremum [GeV]
1000	655	1349
1100	734	1455
1200	712	1631
1300	792	1737
1400	717	1926
1500	815	2117
1600	824	2122
1700	900	2274
1800	919	2344

Table 13: The left and right extremum of the mass window for each generated mass point with a 10 ns lifetime.

$m(\tilde{g})$ [GeV]	Left Extremum [GeV]	Right Extremum [GeV]
800	627	1053
1000	726	1277
1200	857	1584
1400	924	1937
1600	993	2308
1800	1004	2554

Table 14: The left and right extremum of the mass window used for each generated stable mass point.

3181 The 95% confidence level upper limits on the cross sections for a large grid of
 3182 masses (between 800 and 1800 GeV) and lifetimes (between 0.4 and stable) are
 3183 extracted from these counts with the CL_S method using the profile likelihood

$m(\tilde{g})$ [GeV]	Expected Signal	Expected Background	Observed Data
800	462.83 ± 14.86	1.764 ± 0.080	2.0
1000	108.73 ± 3.38	1.458 ± 0.070	1.0
1200	31.74 ± 0.95	1.137 ± 0.060	1.0
1400	10.22 ± 0.29	1.058 ± 0.058	1.0
1600	3.07 ± 0.09	0.947 ± 0.054	1.0
1800	1.08 ± 0.05	0.940 ± 0.054	1.0

Table 15: The expected number of signal events, the expected number of background events, and the observed number of events in data with their respective statistical errors within the respective mass window for each generated stable mass point

$m(\tilde{g})$ [GeV]	Expected Signal	Expected Background	Observed Data
1000	144.48 ± 5.14	1.499 ± 0.069	2.0
1100	73.19 ± 2.61	1.260 ± 0.060	2.0
1200	41.54 ± 1.41	1.456 ± 0.067	2.0
1300	22.58 ± 0.77	1.201 ± 0.058	2.0
1400	12.70 ± 0.42	1.558 ± 0.071	2.0
1500	6.73 ± 0.24	1.237 ± 0.060	2.0
1600	3.90 ± 0.13	1.201 ± 0.058	2.0
1700	2.27 ± 0.07	1.027 ± 0.052	2.0
1800	1.34 ± 0.04	1.019 ± 0.052	2.0

Table 16: The expected number of signal events, the expected number of background events, and the observed number of events in data with their respective statistical errors within the respective mass window for each generated mass point with a lifetime of 10 ns.

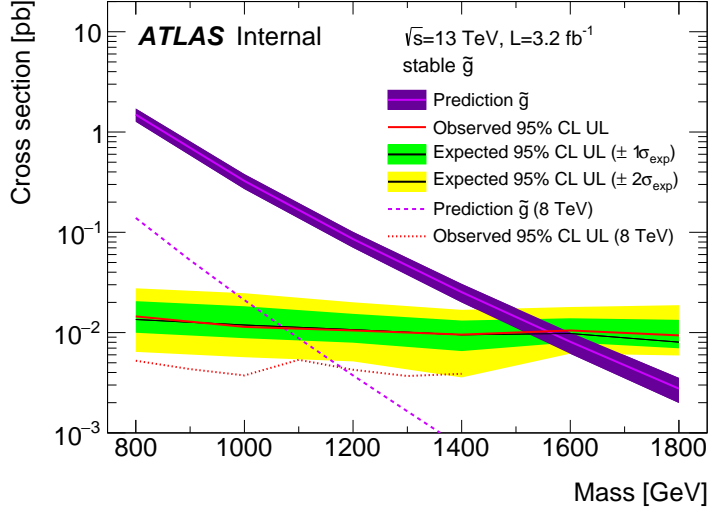


Figure 82: The observed and expected cross section limits as a function of mass for the stable simulated signal. The predicted cross section values for the corresponding signals are included.

ratio as a test statistic [85]. For this procedure, the systematic uncertainties estimated for the signal and background yields are treated as Gaussian-distributed nuisance parameters. The uncertainty on the normalization of the expected background distribution is included in the expected background events. At this point the expected cross section limit is calculated for both the metastable and stable signal region for each lifetime point, and the region with the best expected limit is selected for each lifetime. Using that procedure, the metastable region is used for lifetimes up to and including 30 ns, and the stable region for lifetimes above it.

The resulting cross-sectional upper limits are shown as a function of mass in Figure 82 and Figure 83 for each lifetime considered. The limits are interpolated linearly between each mass point, and the dependence of the limit on the mass is small as the efficiency is relatively constant for large R-Hadron masses. There is however a strong dependence on lifetime, as discussed in Section 11.5, where the probability to form a fully reconstructed track and the kinematic freedom to produce E_T^{miss} result in a local maximum in the limit at 10–30 ns. The figures also include the expected cross section for pair-produced gluino R-Hadrons for reference. For the 10 ns and stable cross section limits, both the observed limit and expected cross section for the Run 1, 8 TeV version of this analysis are included. There the cross sectional limits are lower because of the increased available luminosity, while the signal cross sections were also much lower because of the lower collision energy.

13.4 MASS LIMITS

The cross-sectional limits can then be used to derive a lower mass limit for gluino R-Hadrons by comparing them to the theoretically predicted production cross

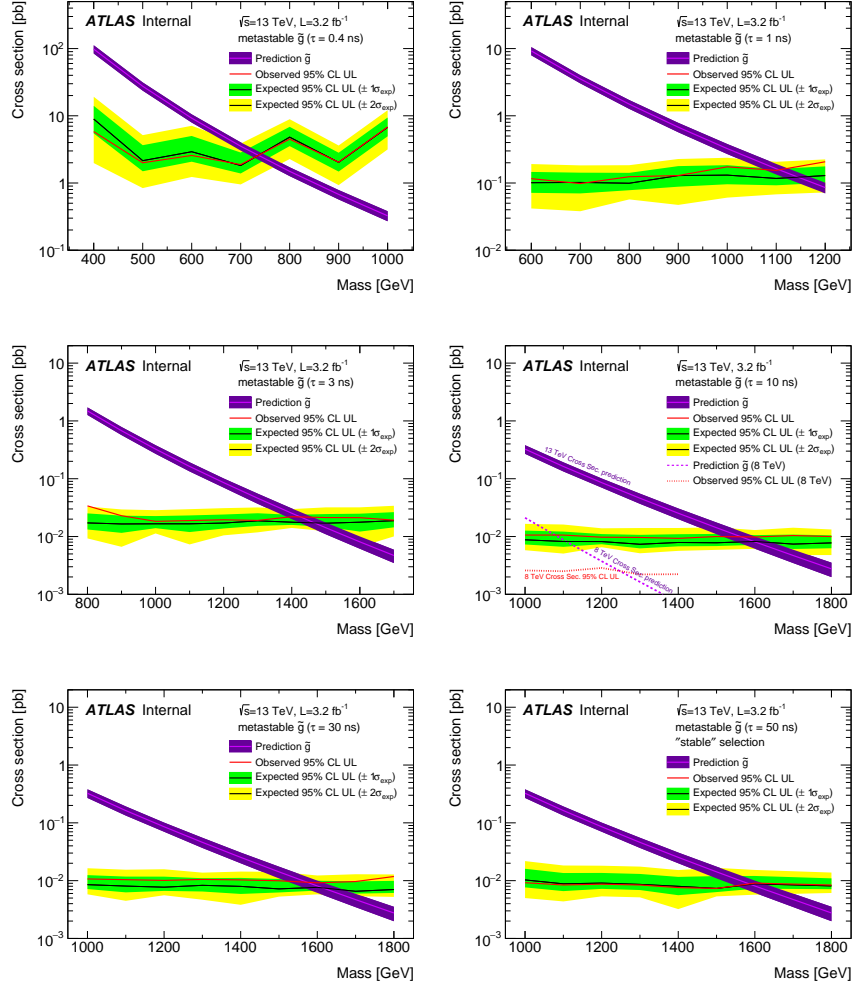


Figure 83: The observed and expected cross section limits as a function of mass for each generated lifetime. The predicted cross section values for the corresponding signals are included.

3209 sections. These mass limits range from only 740 GeV at the lowest lifetimes con-
 3210 sidered, where the selection efficiency is very low, to up to 1580 GeV at 30 ns
 3211 where the selection efficiency is maximized. The observed and expected mass
 3212 limits for each lifetime point are detailed in Table 17, which also lists which se-
 3213 lection region was used for each lifetime. These excluded range of masses as a
 3214 function of lifetime is also shown in Figure 84. The Run 1 limits are included for
 3215 comparison; the limits have increased by about 200 GeV on average. The search
 3216 has also improved since the previous incarnation from Run 1 in optimizing the
 3217 region between 30 GeV and detector-stable lifetimes by introducing the second
 3218 signal region. The definition of the stable region prevents the significant drop
 3219 in mass limit that occurred above 30 GeV in the Run 1 analysis.

Selection	τ [ns]	$M_{\text{obs}} > [\text{GeV}]$	$M_{\text{exp}} > [\text{GeV}]$
Metastable	0.4	740	730
"	1.0	1110	1150
"	3.0	1430	1470
"	10	1570	1600
"	30	1580	1620
Stable	50	1590	1590
"	stable	1570	1580

Table 17: The observed and expected 95% CL lower limit on mass for gluino R-Hadrons for each considered lifetime.

3220 13.5 CONTEXT FOR LONG-LIVED SEARCHES

3221 This search plays an important role in the current, combined [ATLAS](#) search for
 3222 long lived particles. The mass limits provided by various [ATLAS](#) searches for
 3223 long-lived gluino R-Hadrons can be seen in Figure 85. This search provides the
 3224 most competitive limit for lifetimes between 3 ns up through very long lifetimes,
 3225 where it is still competitive with dedicated searches for stable particles. The lim-
 3226 its placed on gluino production are very similar to the limits on promptly decay-
 3227 ing models.

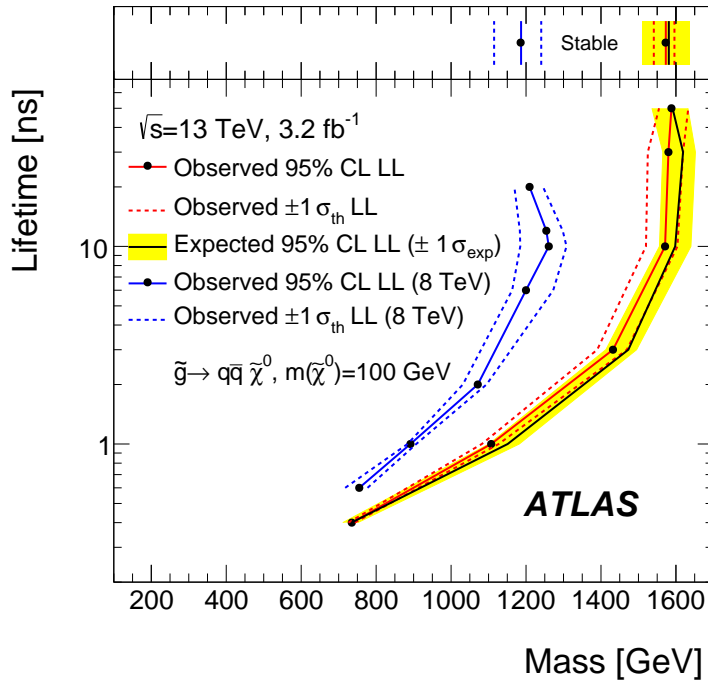


Figure 84: The excluded range of masses as a function of gluino lifetime. The expected lower limit (LL), with its experimental $\pm 1\sigma$ band, is given with respect to the nominal theoretical cross-section. The observed 95% LL obtained at $\sqrt{s} = 8 \text{ TeV}$ [68] is also shown for comparison.

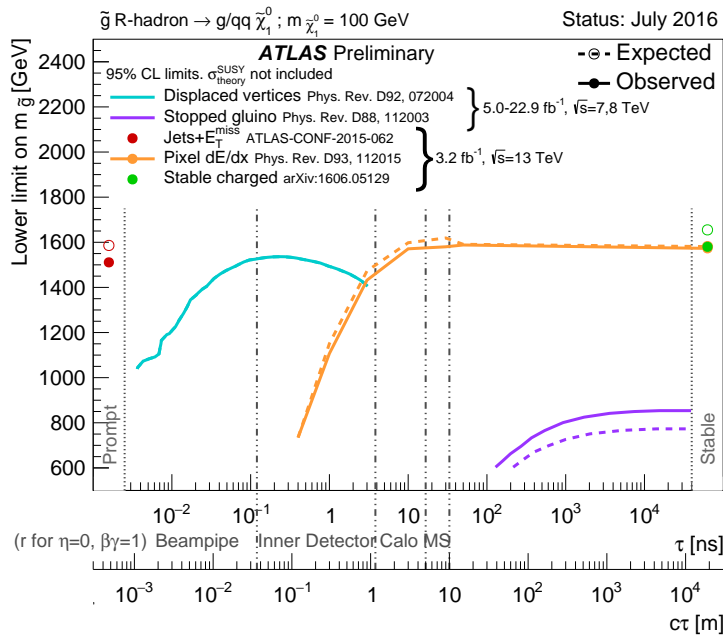


Figure 85: The constraints on the gluino mass as a function of lifetime for a split-supersymmetry model with the gluino R-Hadrons decaying into a gluon or light quarks and a neutralino with mass of 100 GeV. The solid lines indicate the observed limits, while the dashed lines indicate the expected limits. The area below the curves is excluded. The dots represent results for which the particle is assumed to be prompt or stable.

3228

PART VI

3229

CONCLUSIONS

3230

You can put some informational part preamble text here.

14

3231

3232 SUMMARY AND OUTLOOK

3233 14.1 SUMMARY

3234 14.2 OUTLOOK

3235

PART VII

3236

APPENDIX

3237

A

3238

3239 INELASTIC CROSS SECTION

B

3240

³²⁴¹ EXPANDED R-HADRON YIELDS AND LIMITS

$m(\tilde{g})$ [GeV]	Left Extremum [GeV]	Right Extremum [GeV]
1000	682	1387
1100	763	1478
1200	801	1606
1300	809	1841
1400	861	2011
1500	920	2032
1600	952	2173
1800	1017	2422

Table 18: The left and right extremum of the mass window for each generated mass point with a 50 ns lifetime.

$m(\tilde{g})$ [GeV]	Left Extremum [GeV]	Right Extremum [GeV]
1000	689	1321
1100	746	1513
1200	788	1670
1300	860	1734
1400	833	1925
1500	852	2048
1600	833	2283
1700	946	2379
1800	869	2505

Table 19: The left and right extremum of the mass window for each generated mass point with a 30 ns lifetime.

$m(\tilde{g})$ [GeV]	Left Extremum [GeV]	Right Extremum [GeV]
1000	655	1349
1100	734	1455
1200	712	1631
1300	792	1737
1400	717	1926
1500	815	2117
1600	824	2122
1700	900	2274
1800	919	2344

Table 20: The left and right extremum of the mass window for each generated mass point with a 10 ns lifetime.

$m(\tilde{g})$ [GeV]	Left Extremum [GeV]	Right Extremum [GeV]
800	531	1065
900	576	1165
1000	610	1345
1100	635	1432
1200	663	1563
1300	620	1667
1400	742	1727
1500	761	1937
1600	573	2000
1700	621	2182

Table 21: The left and right extremum of the mass window used for each generated mass point with a lifetime of 3 ns.

$m(\tilde{g})$ [GeV]	Left Extremum [GeV]	Right Extremum [GeV]
600	411	758
700	385	876
800	486	970
900	406	987
1000	408	1136
1100	555	1196
1200	516	1378

Table 22: The left and right extremum of the mass window used for each mass point with a lifetime of 1 ns.

$m(\tilde{g})$ [GeV]	Left Extremum [GeV]	Right Extremum [GeV]
400	204	510
500	295	639
600	288	702
700	323	701
800	190	771
900	277	677
1000	249	688

Table 23: The left and right extremum of the mass window for each generated mass point with a lifetime of 0.4 ns.

$m(\tilde{g})$ [GeV]	Left Extremum [GeV]	Right Extremum [GeV]
800	627	1053
1000	726	1277
1200	857	1584
1400	924	1937
1600	993	2308
1800	1004	2554

Table 24: The left and right extremum of the mass window used for each generated stable mass point.

$m(\tilde{g})$ [GeV]	Expected Signal	Expected Background	Observed Data
1000	131.18 ± 6.35	1.803 ± 0.081	1.0 ± 1.0
1100	71.11 ± 3.35	1.409 ± 0.069	1.0 ± 1.0
1200	37.18 ± 1.75	1.310 ± 0.066	1.0 ± 1.0
1300	20.76 ± 0.95	1.431 ± 0.069	1.0 ± 1.0
1400	12.63 ± 0.57	1.273 ± 0.065	1.0 ± 1.0
1500	6.57 ± 0.29	1.115 ± 0.059	1.0 ± 1.0
1600	3.56 ± 0.16	1.041 ± 0.057	1.0 ± 1.0
1800	1.27 ± 0.05	0.918 ± 0.053	1.0 ± 1.0

Table 25: The expected number of signal events, the expected number of background events, and the observed number of events in data with their respective statistical errors within the respective mass window for each generated mass point with a lifetime of 50 ns.

$m(\tilde{g})$ [GeV]	Expected Signal	Expected Background	Observed Data
1000	144.65 ± 6.34	1.328 ± 0.063	2.0 ± 1.4
1100	75.28 ± 3.27	1.255 ± 0.060	2.0 ± 1.4
1200	40.51 ± 1.75	1.193 ± 0.058	2.0 ± 1.4
1300	20.91 ± 0.93	0.997 ± 0.051	2.0 ± 1.4
1400	11.97 ± 0.51	1.131 ± 0.056	2.0 ± 1.4
1500	6.81 ± 0.28	1.111 ± 0.055	2.0 ± 1.4
1600	4.19 ± 0.16	1.193 ± 0.058	2.0 ± 1.4
1700	2.42 ± 0.09	0.963 ± 0.050	2.0 ± 1.4
1800	1.46 ± 0.05	1.138 ± 0.056	3.0 ± 1.7

Table 26: The expected number of signal events, the expected number of background events, and the observed number of events in data with their respective statistical errors within the respective mass window for each generated mass point with a lifetime of 30 ns.

$m(\tilde{g})$ [GeV]	Expected Signal	Expected Background	Observed Data
1000	144.48 ± 5.14	1.499 ± 0.069	2.0 ± 1.4
1100	73.19 ± 2.61	1.260 ± 0.060	2.0 ± 1.4
1200	41.54 ± 1.41	1.456 ± 0.067	2.0 ± 1.4
1300	22.58 ± 0.77	1.201 ± 0.058	2.0 ± 1.4
1400	12.70 ± 0.42	1.558 ± 0.071	2.0 ± 1.4
1500	6.73 ± 0.24	1.237 ± 0.060	2.0 ± 1.4
1600	3.90 ± 0.13	1.201 ± 0.058	2.0 ± 1.4
1700	2.27 ± 0.07	1.027 ± 0.052	2.0 ± 1.4
1800	1.34 ± 0.04	1.019 ± 0.052	2.0 ± 1.4

Table 27: The expected number of signal events, the expected number of background events, and the observed number of events in data with their respective statistical errors within the respective mass window for each generated mass point with a lifetime of 10 ns.

$m(\tilde{g})$ [GeV]	Expected Signal	Expected Background	Observed Data
800	362.97 ± 14.68	1.841 ± 0.080	5.0 ± 2.2
900	169.20 ± 6.69	1.710 ± 0.076	3.0 ± 1.7
1000	84.78 ± 3.23	1.727 ± 0.076	2.0 ± 1.4
1100	40.06 ± 1.60	1.679 ± 0.075	2.0 ± 1.4
1200	20.06 ± 0.81	1.598 ± 0.072	2.0 ± 1.4
1300	10.76 ± 0.43	1.851 ± 0.080	2.0 ± 1.4
1400	5.52 ± 0.22	1.374 ± 0.064	2.0 ± 1.4
1500	3.16 ± 0.13	1.355 ± 0.064	2.0 ± 1.4
1600	2.13 ± 0.11	2.235 ± 0.093	3.0 ± 1.7
1700	1.10 ± 0.06	1.995 ± 0.085	2.0 ± 1.4

Table 28: The expected number of signal events, the expected number of background events, and the observed number of events in data with their respective statistical errors within the respective mass window for each generated mass point with a lifetime of 3 ns.

$m(\tilde{g})$ [GeV]	Expected Signal	Expected Background	Observed Data
600	431.80 ± 36.60	2.418 ± 0.099	3.0 ± 1.7
700	192.77 ± 15.28	3.267 ± 0.126	3.0 ± 1.7
800	69.63 ± 5.90	2.125 ± 0.089	3.0 ± 1.7
900	28.91 ± 2.59	3.114 ± 0.121	3.0 ± 1.7
1000	13.64 ± 1.22	3.359 ± 0.129	5.0 ± 2.2
1100	6.13 ± 0.57	1.879 ± 0.081	3.0 ± 1.7
1200	3.24 ± 0.30	2.387 ± 0.098	5.0 ± 2.2

Table 29: The expected number of signal events, the expected number of background events, and the observed number of events in data with their respective statistical errors within the respective mass window for each generated mass point with a lifetime of 1 ns.

$m(\tilde{g})$ [GeV]	Expected Signal	Expected Background	Observed Data
400	181.71 ± 75.59	6.780 ± 0.238	4.0 ± 2.0
500	103.88 ± 30.05	4.310 ± 0.160	4.0 ± 2.0
600	28.34 ± 9.34	4.868 ± 0.177	4.0 ± 2.0
700	13.62 ± 4.00	3.908 ± 0.147	4.0 ± 2.0
800	2.75 ± 1.15	9.001 ± 0.308	8.0 ± 2.8
900	2.25 ± 0.71	5.045 ± 0.183	5.0 ± 2.2
1000	0.34 ± 0.19	6.026 ± 0.214	6.0 ± 2.4

Table 30: The expected number of signal events, the expected number of background events, and the observed number of events in data with their respective statistical errors within the respective mass window for each generated mass point with a lifetime of p4 ns.

$m(\tilde{g})$ [GeV]	Expected Signal	Expected Background	Observed Data
800	462.83 ± 14.86	1.764 ± 0.080	2.0 ± 1.4
1000	108.73 ± 3.38	1.458 ± 0.070	1.0 ± 1.0
1200	31.74 ± 0.95	1.137 ± 0.060	1.0 ± 1.0
1400	10.22 ± 0.29	1.058 ± 0.058	1.0 ± 1.0
1600	3.07 ± 0.09	0.947 ± 0.054	1.0 ± 1.0
1800	1.08 ± 0.05	0.940 ± 0.054	1.0 ± 1.0

Table 31: The expected number of signal events, the expected number of background events, and the observed number of events in data with their respective statistical errors within the respective mass window for each generated stable mass point

3242 BIBLIOGRAPHY

- 3243 [1] Lyndon Evans and Philip Bryant. "LHC Machine". In: *JINST* 3 (2008), S08001.
3244 doi: [10.1088/1748-0221/3/08/S08001](https://doi.org/10.1088/1748-0221/3/08/S08001).
- 3245 [2] C Lefevre. "LHC: the guide (English version). Guide du LHC (version anglaise)".
3246 2009. URL: <https://cds.cern.ch/record/1165534>.
- 3247 [3] ATLAS Collaboration. "The ATLAS Experiment at the CERN Large Hadron
3248 Collider". In: *JINST* 3 (2008), S08003. doi: [10.1088/1748-0221/3/08/S08003](https://doi.org/10.1088/1748-0221/3/08/S08003).
- 3250 [4] S. Chatrchyan et al. "The CMS experiment at the CERN LHC". In: *JINST*
3251 3 (2008), S08004. doi: [10.1088/1748-0221/3/08/S08004](https://doi.org/10.1088/1748-0221/3/08/S08004).
- 3252 [5] A. Augusto Alves Jr. et al. "The LHCb Detector at the LHC". In: *JINST* 3
3253 (2008), S08005. doi: [10.1088/1748-0221/3/08/S08005](https://doi.org/10.1088/1748-0221/3/08/S08005).
- 3254 [6] K. Aamodt et al. "The ALICE experiment at the CERN LHC". In: *JINST* 3
3255 (2008), S08002. doi: [10.1088/1748-0221/3/08/S08002](https://doi.org/10.1088/1748-0221/3/08/S08002).
- 3256 [7] K. A. Olive et al. "Review of Particle Physics". In: *Chin. Phys. C* 38 (2014),
3257 p. 090001. doi: [10.1088/1674-1137/38/9/090001](https://doi.org/10.1088/1674-1137/38/9/090001).
- 3258 [8] Daniel Froidevaux and Paris Sphicas. "General-Purpose Detectors for the
3259 Large Hadron Collider". In: *Annual Review of Nuclear and Particle Science*
3260 56.1 (2006), pp. 375–440. doi: [10.1146/annurev.nucl.54.070103.181209](https://doi.org/10.1146/annurev.nucl.54.070103.181209). URL: <http://dx.doi.org/10.1146/annurev.nucl.54.070103.181209>.
- 3263 [9] M Capeans, G Darbo, K Einsweiller, M Elsing, T Flick, M Garcia-Sciveres,
3264 C Gemme, H Pernegger, O Rohne, and R Vuillermet. *ATLAS Insertable B-*
3265 *Layer Technical Design Report*. Tech. rep. CERN-LHCC-2010-013. ATLAS-
3266 TDR-19. 2010. URL: <https://cds.cern.ch/record/1291633>.
- 3267 [10] T. Cornelissen, M. Elsing, S. Fleischmann, W. Liebig, and E. Moyse. "Con-
3268 cepts, Design and Implementation of the ATLAS New Tracking (NEWT)".
3269 In: (2007). Ed. by A. Salzburger.
- 3270 [11] "Performance of the ATLAS Inner Detector Track and Vertex Reconstruc-
3271 tion in the High Pile-Up LHC Environment". In: (2012).
- 3272 [12] ATLAS Collaboration. "A neural network clustering algorithm for the AT-
3273 LAS silicon pixel detector". In: *JINST* 9 (2014), P09009. doi: [10.1088/1748-0221/9/09/P09009](https://doi.org/10.1088/1748-0221/9/09/P09009). arXiv: [1406.7690 \[hep-ex\]](https://arxiv.org/abs/1406.7690).
- 3275 [13] ATLAS Collaboration. "Electron reconstruction and identification efficiency
3276 measurements with the ATLAS detector using the 2011 LHC proton–proton
3277 collision data". In: *Eur. Phys. J. C* 74 (2014), p. 2941. doi: [10.1140/epjc/s10052-014-2941-0](https://doi.org/10.1140/epjc/s10052-014-2941-0). arXiv: [1404.2240 \[hep-ex\]](https://arxiv.org/abs/1404.2240). PERF-2013-03.

- 3279 [14] Matteo Cacciari, Gavin P. Salam, and Gregory Soyez. “The anti- k_t jet clustering algorithm”. In: *JHEP* 04 (2008), p. 063. doi: [10.1088/1126-6708/2008/04/063](https://doi.org/10.1088/1126-6708/2008/04/063). arXiv: [0802.1189 \[hep-ph\]](https://arxiv.org/abs/0802.1189).
- 3280
3281
3282 [15] S. Agostinelli et al. “GEANT4: A simulation toolkit”. In: *Nucl. Instrum. Meth. A* 506 (2003), pp. 250–303. doi: [10.1016/S0168-9002\(03\)01368-8](https://doi.org/10.1016/S0168-9002(03)01368-8).
- 3283
3284 [16] ATLAS Collaboration. “A study of the material in the ATLAS inner detector using secondary hadronic interactions”. In: *JINST* 7 (2012), P01013. doi: [10.1088/1748-0221/7/01/P01013](https://doi.org/10.1088/1748-0221/7/01/P01013). arXiv: [1110.6191 \[hep-ex\]](https://arxiv.org/abs/1110.6191). PERF-2011-08.
- 3285
3286
3287
3288 [17] ATLAS Collaboration. “Electron and photon energy calibration with the ATLAS detector using LHC Run 1 data”. In: *Eur. Phys. J. C* 74 (2014), p. 3071. doi: [10.1140/epjc/s10052-014-3071-4](https://doi.org/10.1140/epjc/s10052-014-3071-4). arXiv: [1407.5063 \[hep-ex\]](https://arxiv.org/abs/1407.5063). PERF-2013-05.
- 3289
3290
3291
3292 [18] ATLAS Collaboration. “A measurement of the calorimeter response to single hadrons and determination of the jet energy scale uncertainty using LHC Run-1 pp -collision data with the ATLAS detector”. In: (2016). arXiv: [1607.08842 \[hep-ex\]](https://arxiv.org/abs/1607.08842). PERF-2015-05.
- 3293
3294
3295
3296 [19] ATLAS Collaboration. “Single hadron response measurement and calorimeter jet energy scale uncertainty with the ATLAS detector at the LHC”. In: *Eur. Phys. J. C* 73 (2013), p. 2305. doi: [10.1140/epjc/s10052-013-2305-1](https://doi.org/10.1140/epjc/s10052-013-2305-1). arXiv: [1203.1302 \[hep-ex\]](https://arxiv.org/abs/1203.1302). PERF-2011-05.
- 3297
3298
3299
3300 [20] ATLAS Collaboration. “The ATLAS Simulation Infrastructure”. In: *Eur. Phys. J. C* 70 (2010), p. 823. doi: [10.1140/epjc/s10052-010-1429-9](https://doi.org/10.1140/epjc/s10052-010-1429-9). arXiv: [1005.4568 \[hep-ex\]](https://arxiv.org/abs/1005.4568). SOFT-2010-01.
- 3301
3302
3303 [21] T. Sjöstrand, S. Mrenna, and P. Skands. “A Brief Introduction to PYTHIA 8.1”. In: *Comput. Phys. Commun.* 178 (2008), pp. 852–867. doi: [10.1016/j.cpc.2008.01.036](https://doi.org/10.1016/j.cpc.2008.01.036). arXiv: [0710.3820](https://arxiv.org/abs/0710.3820).
- 3304
3305
3306 [22] ATLAS Collaboration. *Summary of ATLAS Pythia 8 tunes*. ATL-PHYS-PUB-2012-003. 2012. URL: <http://cds.cern.ch/record/1474107>.
- 3307
3308 [23] A.D. Martin, W.J. Stirling, R.S. Thorne, and G. Watt. “Parton distributions for the LHC”. In: *Eur. Phys. J. C* 63 (2009). Figures from the MSTW Website, pp. 189–285. doi: [10.1140/epjc/s10052-009-1072-5](https://doi.org/10.1140/epjc/s10052-009-1072-5). arXiv: [0901.0002](https://arxiv.org/abs/0901.0002).
- 3309
3310
3311
3312 [24] A. Sherstnev and R.S. Thorne. “Parton Distributions for LO Generators”. In: *Eur. Phys. J. C* 55 (2008), pp. 553–575. doi: [10.1140/epjc/s10052-008-0610-x](https://doi.org/10.1140/epjc/s10052-008-0610-x). arXiv: [0711.2473](https://arxiv.org/abs/0711.2473).
- 3313
3314
3315 [25] A. Ribon et al. *Status of Geant4 hadronic physics for the simulation of LHC experiments at the start of LHC physics program*. CERN-LCGAPP-2010-02. 2010. URL: <http://lcgapp.cern.ch/project/docs/noteStatusHadronic2010.pdf>.
- 3316
3317
3318

- 3319 [26] M. P. Guthrie, R. G. Alsmiller, and H. W. Bertini. "Calculation of the cap-
 3320 ture of negative pions in light elements and comparison with experiments
 3321 pertaining to cancer radiotherapy". In: *Nucl. Instrum. Meth.* 66 (1968), pp. 29–
 3322 36. doi: [10.1016/0029-554X\(68\)90054-2](https://doi.org/10.1016/0029-554X(68)90054-2).
- 3323 [27] H. W. Bertini and P. Guthrie. "News item results from medium-energy
 3324 intranuclear-cascade calculation". In: *Nucl. Instr. and Meth. A* 169 (1971),
 3325 p. 670. doi: [10.1016/0375-9474\(71\)90710-X](https://doi.org/10.1016/0375-9474(71)90710-X).
- 3326 [28] V.A. Karmanov. "Light Front Wave Function of Relativistic Composite
 3327 System in Explicitly Solvable Model". In: *Nucl. Phys. B* 166 (1980), p. 378.
 3328 doi: [10.1016/0550-3213\(80\)90204-7](https://doi.org/10.1016/0550-3213(80)90204-7).
- 3329 [29] H. S. Fesefeldt. *GHEISHA program*. Pitha-85-02, Aachen. 1985.
- 3330 [30] G. Folger and J.P. Wellisch. "String parton models in Geant4". In: (2003).
 3331 arXiv: [nucl-th/0306007](https://arxiv.org/abs/nucl-th/0306007).
- 3332 [31] N. S. Amelin et al. "Transverse flow and collectivity in ultrarelativistic
 3333 heavy-ion collisions". In: *Phys. Rev. Lett.* 67 (1991), p. 1523. doi: [10.1103/PhysRevLett.67.1523](https://doi.org/10.1103/PhysRevLett.67.1523).
- 3335 [32] N. S. Amelin et al. "Collectivity in ultrarelativistic heavy ion collisions". In:
 3336 *Nucl. Phys. A* 544 (1992), p. 463. doi: [10.1016/0375-9474\(92\)90598-E](https://doi.org/10.1016/0375-9474(92)90598-E).
- 3338 [33] L. V. Bravina et al. "Fluid dynamics and Quark Gluon string model - What
 3339 we can expect for Au+Au collisions at 11.6 AGeV/c". In: *Nucl. Phys. A* 566
 3340 (1994), p. 461. doi: [10.1016/0375-9474\(94\)90669-6](https://doi.org/10.1016/0375-9474(94)90669-6).
- 3341 [34] L. V. Bravin et al. "Scaling violation of transverse flow in heavy ion col-
 3342 lisions at AGS energies". In: *Phys. Lett. B* 344 (1995), p. 49. doi: [10.1016/0370-2693\(94\)01560-Y](https://doi.org/10.1016/0370-2693(94)01560-Y).
- 3344 [35] B. Andersson et al. "A model for low-pT hadronic reactions with general-
 3345 izations to hadron-nucleus and nucleus-nucleus collisions". In: *Nucl. Phys.*
 3346 *B* 281 (1987), p. 289. doi: [10.1016/0550-3213\(87\)90257-4](https://doi.org/10.1016/0550-3213(87)90257-4).
- 3347 [36] B. Andersson, A. Tai, and B.-H. Sa. "Final state interactions in the (nuclear)
 3348 FRITIOF string interaction scenario". In: *Z. Phys. C* 70 (1996), pp. 499–
 3349 506. doi: [10.1007/s002880050127](https://doi.org/10.1007/s002880050127).
- 3350 [37] B. Nilsson-Almqvist and E. Stenlund. "Interactions Between Hadrons and
 3351 Nuclei: The Lund Monte Carlo, Fritiof Version 1.6". In: *Comput. Phys. Com-*
 3352 *mun.* 43 (1987), p. 387. doi: [10.1016/0010-4655\(87\)90056-7](https://doi.org/10.1016/0010-4655(87)90056-7).
- 3353 [38] B. Ganhuyag and V. Uzhinsky. "Modified FRITIOF code: Negative charged
 3354 particle production in high energy nucleus nucleus interactions". In: *Czech.*
 3355 *J. Phys.* 47 (1997), pp. 913–918. doi: [10.1023/A:1021296114786](https://doi.org/10.1023/A:1021296114786).
- 3356 [39] ATLAS Collaboration. "Topological cell clustering in the ATLAS calorime-
 3357 ters and its performance in LHC Run 1". In: (2016). arXiv: [1603.02934](https://arxiv.org/abs/1603.02934)
 3358 [[hep-ex](#)].
- 3359 [40] Peter Speckmayer. "Energy Measurement of Hadrons with the CERN AT-
 3360 LAS Calorimeter". Presented on 18 Jun 2008. PhD thesis. Vienna: Vienna,
 3361 Tech. U., 2008. URL: <http://cds.cern.ch/record/1112036>.

- 3362 [41] CMS Collaboration. “The CMS barrel calorimeter response to particle
 3363 beams from 2 to 350 GeV/c”. In: *Eur. Phys. J. C* 60.3 (2009). doi: [10.1140/epjc/s10052-009-0959-5](https://doi.org/10.1140/epjc/s10052-009-0959-5).
- 3365 [42] J. Beringer et al. (Particle Data Group). “Review of Particle Physics”. In:
 3366 *Chin. Phys. C* 38 (2014), p. 090001. URL: <http://pdg.lbl.gov>.
- 3367 [43] P. Adragna et al. “Measurement of Pion and Proton Response and Lon-
 3368 gitudinal Shower Profiles up to 20 Nuclear Interaction Lengths with the
 3369 ATLAS Tile Calorimeter”. In: *Nucl. Instrum. Meth. A* 615 (2010), pp. 158–
 3370 181. doi: [10.1016/j.nima.2010.01.037](https://doi.org/10.1016/j.nima.2010.01.037).
- 3371 [44] ATLAS Collaboration. “Jet energy measurement and its systematic uncer-
 3372 tainty in proton–proton collisions at $\sqrt{s} = 7$ TeV with the ATLAS detec-
 3373 tor”. In: *Eur. Phys. J. C* 75 (2015), p. 17. doi: [10.1140/epjc/s10052-014-3190-y](https://doi.org/10.1140/epjc/s10052-014-3190-y). arXiv: [1406.0076 \[hep-ex\]](https://arxiv.org/abs/1406.0076). PERF-2012-01.
- 3375 [45] Hung-Liang Lai, Marco Guzzi, Joey Huston, Zhao Li, Pavel M. Nadolsky,
 3376 et al. “New parton distributions for collider physics”. In: *Phys. Rev. D* 82
 3377 (2010), p. 074024. doi: [10.1103/PhysRevD.82.074024](https://doi.org/10.1103/PhysRevD.82.074024). arXiv: [1007.2241 \[hep-ph\]](https://arxiv.org/abs/1007.2241).
- 3379 [46] E. Abat et al. “Study of energy response and resolution of the ATLAS barrel
 3380 calorimeter to hadrons of energies from 20 to 350 GeV”. In: *Nucl. Instrum.*
 3381 *Meth. A* 621.1-3 (2010), pp. 134 – 150. doi: <http://dx.doi.org/10.1016/j.nima.2010.04.054>.
- 3383 [47] ATLAS Collaboration. “Jet energy measurement with the ATLAS detector
 3384 in proton–proton collisions at $\sqrt{s} = 7$ TeV”. In: *Eur. Phys. J. C* 73 (2013),
 3385 p. 2304. doi: [10.1140/epjc/s10052-013-2304-2](https://doi.org/10.1140/epjc/s10052-013-2304-2). arXiv: [1112.6426 \[hep-ex\]](https://arxiv.org/abs/1112.6426). PERF-2011-03.
- 3387 [48] Nausheen R. Shah and Carlos E. M. Wagner. “Gravitons and dark matter in
 3388 universal extra dimensions”. In: *Phys. Rev. D* 74 (2006), p. 104008. doi: [10.1103/PhysRevD.74.104008](https://doi.org/10.1103/PhysRevD.74.104008). arXiv: [hep-ph/0608140 \[hep-ph\]](https://arxiv.org/abs/hep-ph/0608140).
- 3390 [49] Jonathan L. Feng, Arvind Rajaraman, and Fumihiro Takayama. “Graviton
 3391 cosmology in universal extra dimensions”. In: *Phys. Rev. D* 68 (2003), p. 085018.
 3392 doi: [10.1103/PhysRevD.68.085018](https://doi.org/10.1103/PhysRevD.68.085018). arXiv: [hep-ph/0307375 \[hep-ph\]](https://arxiv.org/abs/hep-ph/0307375).
- 3394 [50] Paul H. Frampton and Pham Quang Hung. “Long-lived quarks?” In: *Phys.*
 3395 *Rev. D* 58 (5 1998), p. 057704. doi: [10.1103/PhysRevD.58.057704](https://doi.org/10.1103/PhysRevD.58.057704).
 3396 URL: <http://link.aps.org/doi/10.1103/PhysRevD.58.057704>.
- 3398 [51] C. Friberg, E. Norrbin, and T. Sjostrand. “QCD aspects of leptoquark pro-
 3399 duction at HERA”. In: *Phys. Lett. B* 403 (1997), pp. 329–334. doi: [10.1016/S0370-2693\(97\)00543-1](https://doi.org/10.1016/S0370-2693(97)00543-1). arXiv: [hep-ph/9704214 \[hep-ph\]](https://arxiv.org/abs/hep-ph/9704214).
- 3401 [52] Herbert K. Dreiner. “An introduction to explicit R-parity violation”. In:
 3402 (1997). arXiv: [hep-ph/9707435](https://arxiv.org/abs/hep-ph/9707435).

- 3403 [53] Edmond L. Berger and Zack Sullivan. "Lower limits on R-parity-violating
 3404 couplings in supersymmetry". In: *Phys. Rev. Lett.* 92 (2004), p. 201801. doi:
 3405 [10.1103/PhysRevLett.92.201801](https://doi.org/10.1103/PhysRevLett.92.201801). arXiv: [hep-ph/0310001](https://arxiv.org/abs/hep-ph/0310001).
- 3406 [54] R. Barbieri, C. Berat, M. Besancon, M. Chemtob, A. Deandrea, et al. "R-
 3407 parity violating supersymmetry". In: *Phys. Rept.* 420 (2005), p. 1. doi: [10.1016/j.physrep.2005.08.006](https://doi.org/10.1016/j.physrep.2005.08.006). arXiv: [hep-ph/0406039](https://arxiv.org/abs/hep-ph/0406039).
- 3409 [55] M. Fairbairn et al. "Stable massive particles at colliders". In: *Phys. Rept.* 438
 3410 (2007), p. 1. doi: [10.1016/j.physrep.2006.10.002](https://doi.org/10.1016/j.physrep.2006.10.002). arXiv: [hep-ph/0611040](https://arxiv.org/abs/hep-ph/0611040).
- 3412 [56] Christopher F. Kolda. "Gauge-mediated supersymmetry breaking: Intro-
 3413 duction, review and update". In: *Nucl. Phys. Proc. Suppl.* 62 (1998), p. 266.
 3414 doi: [10.1016/S0920-5632\(97\)00667-1](https://doi.org/10.1016/S0920-5632(97)00667-1). arXiv: [hep-ph/9707450](https://arxiv.org/abs/hep-ph/9707450).
- 3415 [57] Howard Baer, Kingman Cheung, and John F. Gunion. "A Heavy gluino as
 3416 the lightest supersymmetric particle". In: *Phys. Rev. D* 59 (1999), p. 075002.
 3417 doi: [10.1103/PhysRevD.59.075002](https://doi.org/10.1103/PhysRevD.59.075002). arXiv: [hep-ph/9806361](https://arxiv.org/abs/hep-ph/9806361).
- 3418 [58] S. James Gates Jr. and Oleg Lebedev. "Searching for supersymmetry in
 3419 hadrons". In: *Phys. Lett. B* 477 (2000), p. 216. doi: [10.1016/S0370-2693\(00\)00172-6](https://doi.org/10.1016/S0370-2693(00)00172-6). arXiv: [hep-ph/9912362](https://arxiv.org/abs/hep-ph/9912362).
- 3421 [59] G. F. Giudice and A. Romanino. "Split supersymmetry". In: *Nucl. Phys. B*
 3422 699 (2004), p. 65. doi: [10.1016/j.nuclphysb.2004.11.048](https://doi.org/10.1016/j.nuclphysb.2004.11.048). arXiv:
 3423 [hep-ph/0406088](https://arxiv.org/abs/hep-ph/0406088).
- 3424 [60] N. Arkani-Hamed, S. Dimopoulos, G. F. Giudice, and A. Romanino. "As-
 3425 pects of split supersymmetry". In: *Nucl. Phys. B* 709 (2005), p. 3. doi: [10.1016/j.nuclphysb.2004.12.026](https://doi.org/10.1016/j.nuclphysb.2004.12.026). arXiv: [hep-ph/0409232](https://arxiv.org/abs/hep-ph/0409232).
- 3427 [61] Glennys R. Farrar and Pierre Fayet. "Phenomenology of the Production,
 3428 Decay, and Detection of New Hadronic States Associated with Supersym-
 3429 metry". In: *Phys. Lett.* B76 (1978), pp. 575–579. doi: [10.1016/0370-2693\(78\)90858-4](https://doi.org/10.1016/0370-2693(78)90858-4).
- 3431 [62] A. C. Kraan, J. B. Hansen, and P. Nevski. "Discovery potential of R-hadrons
 3432 with the ATLAS detector". In: *Eur. Phys. J.* C49 (2007), pp. 623–640. doi:
 3433 [10.1140/epjc/s10052-006-0162-x](https://doi.org/10.1140/epjc/s10052-006-0162-x). arXiv: [hep-ex/0511014](https://arxiv.org/abs/hep-ex/0511014)
 3434 [[hep-ex](#)].
- 3435 [63] Rasmus Mackeprang and David Milstead. "An Updated Description of
 3436 Heavy-Hadron Interactions in GEANT-4". In: *Eur. Phys. J.* C66 (2010), pp. 493–
 3437 501. doi: [10.1140/epjc/s10052-010-1262-1](https://doi.org/10.1140/epjc/s10052-010-1262-1). arXiv: [0908.1868](https://arxiv.org/abs/0908.1868)
 3438 [[hep-ph](#)].
- 3439 [64] ATLAS Collaboration. "Search for massive, long-lived particles using mul-
 3440 titrack displaced vertices or displaced lepton pairs in pp collisions at $\sqrt{s} =$
 3441 8 TeV with the ATLAS detector". In: *Phys. Rev. D* 92 (2015), p. 072004.
 3442 doi: [10.1103/PhysRevD.92.072004](https://doi.org/10.1103/PhysRevD.92.072004). arXiv: [1504.05162 \[hep-ex\]](https://arxiv.org/abs/1504.05162).
 3443 SUSY-2014-02.

- 3444 [65] ATLAS Collaboration. “Search for charginos nearly mass degenerate with
 3445 the lightest neutralino based on a disappearing-track signature in pp col-
 3446 lisions at $\sqrt{s} = 8$ TeV with the ATLAS detector”. In: *Phys. Rev. D* 88 (2013),
 3447 p. 112006. doi: [10.1103/PhysRevD.88.112006](https://doi.org/10.1103/PhysRevD.88.112006). arXiv: [1310.3675](https://arxiv.org/abs/1310.3675)
 3448 [[hep-ex](#)]. SUSY-2013-01.
- 3449 [66] ATLAS Collaboration. “Searches for heavy long-lived sleptons and R-Hadrons
 3450 with the ATLAS detector in pp collisions at $\sqrt{s} = 7$ TeV”. In: *Phys. Lett. B*
 3451 720 (2013), p. 277. doi: [10.1016/j.physletb.2013.02.015](https://doi.org/10.1016/j.physletb.2013.02.015). arXiv:
 3452 [1211.1597](https://arxiv.org/abs/1211.1597) [[hep-ex](#)]. SUSY-2012-01.
- 3453 [67] ATLAS Collaboration. “Searches for heavy long-lived charged particles
 3454 with the ATLAS detector in proton–proton collisions at $\sqrt{s} = 8$ TeV”. In:
 3455 *JHEP* 01 (2015), p. 068. doi: [10.1007/JHEP01\(2015\)068](https://doi.org/10.1007/JHEP01(2015)068). arXiv:
 3456 [1411.6795](https://arxiv.org/abs/1411.6795) [[hep-ex](#)]. SUSY-2013-22.
- 3457 [68] ATLAS Collaboration. “Search for metastable heavy charged particles with
 3458 large ionisation energy loss in pp collisions at $\sqrt{s} = 8$ TeV using the AT-
 3459 LAS experiment”. In: *Eur. Phys. J. C* 75 (2015), p. 407. doi: [10.1140/epjc/s10052-015-3609-0](https://doi.org/10.1140/epjc/s10052-015-3609-0). arXiv: [1506.05332](https://arxiv.org/abs/1506.05332) [[hep-ex](#)]. SUSY-
 3460 2014-09.
- 3461 [69] ATLAS Collaboration. “Search for heavy long-lived charged R -hadrons
 3462 with the ATLAS detector in 3.2 fb^{-1} of proton–proton collision data at
 3463 $\sqrt{s} = 13$ TeV”. In: *Phys. Lett. B* 760 (2016), pp. 647–665. doi: [10.1016/j.physletb.2016.07.042](https://doi.org/10.1016/j.physletb.2016.07.042). arXiv: [1606.05129](https://arxiv.org/abs/1606.05129) [[hep-ex](#)].
- 3463 [70] Torbjorn Sjöstrand, Stephen Mrenna, and Peter Skands. “PYTHIA 6.4 Physics
 3464 and Manual”. In: *JHEP* 0605 (2006), p. 026. doi: [10.1088/1126-6708/2006/05/026](https://doi.org/10.1088/1126-6708/2006/05/026). arXiv: [hep-ph/0603175](https://arxiv.org/abs/hep-ph/0603175).
- 3465 [71] *Further ATLAS tunes of PYTHIA6 and Pythia 8*. Tech. rep. ATL-PHYS-PUB-
 3466 2011-014. Geneva: CERN, 2011. url: <https://cds.cern.ch/record/1400677>.
- 3467 [72] Aafke Christine Kraan. “Interactions of heavy stable hadronizing parti-
 3468 cles”. In: *Eur. Phys. J. C* 37 (2004), pp. 91–104. doi: [10.1140/epjc/s2004-01946-6](https://doi.org/10.1140/epjc/s2004-01946-6). arXiv: [hep-ex/0404001](https://arxiv.org/abs/hep-ex/0404001) [[hep-ex](#)].
- 3469 [73] M. Fairbairn et al. “Stable massive particles at colliders”. In: *Phys. Rept.* 438
 3470 (2007), p. 1. doi: [10.1016/j.physrep.2006.10.002](https://doi.org/10.1016/j.physrep.2006.10.002). arXiv: [hep-ph/0611040](https://arxiv.org/abs/hep-ph/0611040).
- 3471 [74] W. Beenakker, R. Hopker, M. Spira, and P. M. Zerwas. “Squark and gluino
 3472 production at hadron colliders”. In: *Nucl. Phys. B* 492 (1997), p. 51. doi:
 3473 [10.1016/S0550-3213\(97\)00084-9](https://doi.org/10.1016/S0550-3213(97)00084-9). arXiv: [hep-ph/9610490](https://arxiv.org/abs/hep-ph/9610490).
- 3474 [75] A. Kulesza and L. Motyka. “Threshold resummation for squark-antisquark
 3475 and gluino-pair production at the LHC”. In: *Phys. Rev. Lett.* 102 (2009),
 3476 p. 111802. doi: [10.1103/PhysRevLett.102.111802](https://doi.org/10.1103/PhysRevLett.102.111802). arXiv: [0807.2405](https://arxiv.org/abs/0807.2405) [[hep-ph](#)].

- 3485 [76] A. Kulesza and L. Motyka. “Soft gluon resummation for the production
 3486 of gluino-gluino and squark-antisquark pairs at the LHC”. In: *Phys. Rev.*
 3487 *D* 80 (2009), p. 095004. doi: [10.1103/PhysRevD.80.095004](https://doi.org/10.1103/PhysRevD.80.095004). arXiv:
 3488 [0905.4749 \[hep-ph\]](https://arxiv.org/abs/0905.4749).
- 3489 [77] Wim Beenakker, Silja Brensing, Michael Kramer, Anna Kulesza, Eric Lae-
 3490 nen, et al. “Soft-gluon resummation for squark and gluino hadroproduc-
 3491 tion”. In: *JHEP* 0912 (2009), p. 041. doi: [10.1088/1126-6708/2009/12/041](https://doi.org/10.1088/1126-6708/2009/12/041). arXiv: [0909.4418 \[hep-ph\]](https://arxiv.org/abs/0909.4418).
- 3493 [78] W. Beenakker, S. Brensing, M.n Kramer, A. Kulesza, E. Laenen, et al. “Squark
 3494 and Gluino Hadroproduction”. In: *Int. J. Mod. Phys. A* 26 (2011), p. 2637.
 3495 doi: [10.1142/S0217751X11053560](https://doi.org/10.1142/S0217751X11053560). arXiv: [1105.1110 \[hep-ph\]](https://arxiv.org/abs/1105.1110).
- 3496 [79] Michael Krämer et al. *Supersymmetry production cross sections in pp collisions*
 3497 at $\sqrt{s} = 7 \text{ TeV}$. 2012. arXiv: [1206.2892 \[hep-ph\]](https://arxiv.org/abs/1206.2892).
- 3498 [80] Rasmus Mackeprang and Andrea Rizzi. “Interactions of Coloured Heavy
 3499 Stable Particles in Matter”. In: *Eur. Phys. J.* C50 (2007), pp. 353–362. doi:
 3500 [10.1140/epjc/s10052-007-0252-4](https://doi.org/10.1140/epjc/s10052-007-0252-4). arXiv: [hep-ph/0612161](https://arxiv.org/abs/hep-ph/0612161)
 3501 [hep-ph].
- 3502 [81] Rasmus Mackeprang and David Milstead. “An Updated Description of
 3503 Heavy-Hadron Interactions in GEANT-4”. In: *Eur. Phys. J.* C66 (2010), pp. 493–
 3504 501. doi: [10.1140/epjc/s10052-010-1262-1](https://doi.org/10.1140/epjc/s10052-010-1262-1). arXiv: [0908.1868](https://arxiv.org/abs/0908.1868)
 3505 [hep-ph].
- 3506 [82] J. Alwall, R. Frederix, S. Frixione, V. Hirschi, F. Maltoni, O. Mattelaer, H. S.
 3507 Shao, T. Stelzer, P. Torrielli, and M. Zaro. “The automated computation of
 3508 tree-level and next-to-leading order differential cross sections, and their
 3509 matching to parton shower simulations”. In: *JHEP* 07 (2014), p. 079. doi:
 3510 [10.1007/JHEP07\(2014\)079](https://doi.org/10.1007/JHEP07(2014)079). arXiv: [1405.0301 \[hep-ph\]](https://arxiv.org/abs/1405.0301).
- 3511 [83] “dE/dx measurement in the ATLAS Pixel Detector and its use for particle
 3512 identification”. In: (2011).
- 3513 [84] ATLAS Collaboration. “The ATLAS Simulation Infrastructure”. In: *Eur.*
 3514 *Phys. J.* C70 (2010), pp. 823–874. doi: [10.1140/epjc/s10052-010-1429-9](https://doi.org/10.1140/epjc/s10052-010-1429-9). arXiv: [1005.4568 \[physics.ins-det\]](https://arxiv.org/abs/1005.4568).
- 3516 [85] Alexander L. Read. “Presentation of search results: The CL(s) technique”.
 3517 In: *J. Phys.* G28 (2002). [,11(2002)], pp. 2693–2704. doi: [10.1088/0954-3899/28/10/313](https://doi.org/10.1088/0954-3899/28/10/313).

3519 DECLARATION

3520 Put your declaration here.

3521 *Berkeley, CA, September 2016*

3522

Bradley Axen

3523

3524 COLOPHON

3525

Not sure that this is necessary.